

CHARACTERIZATION AND ADVANCED COMMUNICATION
TECHNIQUES FOR FREE-SPACE OPTICAL CHANNELS

by
Jaime Andrés Anguita

A Dissertation Submitted to the Faculty of the
DEPARTMENT OF ELECTRICAL AND COMPUTER ENGINEERING
In Partial Fulfillment of the Requirements
For the Degree of
DOCTOR OF PHILOSOPHY
In the Graduate College
THE UNIVERSITY OF ARIZONA

2007

THE UNIVERSITY OF ARIZONA
GRADUATE COLLEGE

As members of the Dissertation Committee, we certify that we have read the dissertation prepared by Jaime Andrés Anguita

entitled “Characterization and Advanced Communication Techniques for Free-Space Optical Channels”

and recommend that it be accepted as fulfilling the dissertation requirement for the

Degree of Doctor of Philosophy

_____ Date: 11/30/2007
Mark A. Neifeld, PhD

_____ Date: 11/30/2007
Bane V. Vasic, PhD

_____ Date: 11/30/2007
Michael Marcellin, PhD

Final approval and acceptance of this dissertation is contingent upon the candidates submission of the final copies of the dissertation to the Graduate College.

I hereby certify that I have read this dissertation prepared under my direction and recommend that it be accepted as fulfilling the dissertation requirement.

_____ Date: 11/30/2007
Dissertation Director: Mark A. Neifeld, PhD

_____ Date: 11/30/2007
Dissertation Director: Bane V. Vasic, PhD

STATEMENT BY AUTHOR

This dissertation has been submitted in partial fulfillment of requirements for an advanced degree at the University of Arizona and is deposited in the University Library to be made available to borrowers under rules of the Library.

Brief quotations from this dissertation are allowable without special permission, provided that accurate acknowledgment of source is made. Requests for permission for extended quotation from or reproduction of this manuscript in whole or in part may be granted by the head of the major department or the Dean of the Graduate College when in his or her judgment the proposed use of the material is in the interests of scholarship. In all other instances, however, permission must be obtained from the author.

SIGNED: Jaime A. Anguita

To my wife Francisca

ACKNOWLEDGMENTS

I would like to thank my co-advisor Dr. Mark A. Neifeld for teaching me the wonders of optics, for his continuous support over many years, and for his commitment to help me find excellence in research. I would like to thank my co-advisor Bane V. Vasic for his rigorous yet patient advice in communication theory, for his enjoyable classes, and for his friendly support. Both Dr. Neifeld's and Dr. Vasic's example and have helped me be more enthusiastic with my decision to work in academia.

I would also like to thank all the professors in the Department, particularly Dr. Michael Marcellin and Dr. Raymond Kostuk for their committed teaching.

With high regard and gratefulness I would like to mention the Senior Graduate Advisor Mrs. Tami Whelan and the secretary Mr. Curt Booth.

I would finally like to thank my children for their patience and unconditional love. But above all I am grateful to my wife, whose love, generosity, and wisdom make me desire to be a better person.

Deo omnis gloria

TABLE OF CONTENTS

LIST OF FIGURES	9
LIST OF TABLES	13
ABSTRACT	14
1. INTRODUCTION	16
1.1. The free-space optical laser link	18
1.2. The optical atmospheric channel	20
1.3. Contributions of this dissertation	22
2. BEAM PROPAGATION AND CHANNEL MODELS	26
2.1. Kolmogorov theory	27
2.2. Numerical wave propagation in turbulence	29
2.3. Scintillation experiment	32
2.4. Analytical intensity fluctuation models	35
2.4.1. Lognormal density	35
2.4.2. Exponential density	36
2.4.3. Gamma-gamma density	36
3. CHANNEL CAPACITY AND LDPC CODES IN TURBULENT CHANNELS	38
3.1. Introduction	38
3.2. Atmospheric turbulent channel modeling	39
3.2.1. Zero inner scale	41
3.2.2. Nonzero Inner Scale	42
3.3. Channel Capacity of an Atmospheric FSO Channel	43
3.3.1. Channel Capacity Calculation	44
3.3.2. Capacity for Zero Inner Scale	46
3.3.3. Capacity for nonzero inner scale	49
3.4. Efficient LDPC error-correction codes	52
3.5. Conclusions	57
4. SPATIAL CORRELATION AND IRRADIANCE FLUCTUATIONS IN MULTIPLE-BEAM LINKS	59
4.1. Introduction	59
4.2. System model	62
4.2.1. Description of system components	62
4.2.2. Beam propagation and turbulence simulation	64
4.2.3. Definition of channel coefficients	65

TABLE OF CONTENTS—*Continued*

4.3.	Analysis of correlation	66
4.3.1.	Correlation versus receiver aperture	67
4.3.2.	Correlation versus propagation distance	69
4.4.	Scaling of scintillation using multiple beams	72
4.4.1.	Scintillation reduction	72
4.4.2.	Comparison with previously published experiments	76
4.4.3.	Density function of multi-beam case	78
4.5.	Bit-error rate comparison using space-time codes	81
4.5.1.	Space repetition code	81
4.5.2.	Space-time block code	83
4.5.3.	Monte Carlo BER simulations	85
4.6.	Conclusions	88
5.	ORBITAL ANGULAR MOMENTUM-BASED CHANNEL MULTIPLEXING	90
5.1.	Introduction	90
5.2.	Orbital angular momentum in Laguerre-Gauss beams	93
5.2.1.	Laguerre-Gauss modal distribution	93
5.2.2.	Generation methods	95
5.3.	OAM-multiplexed system and propagation in turbulence	95
5.3.1.	Transmitter and receiver models	95
5.3.2.	Propagation in turbulence	98
5.4.	OAM crosstalk induced by turbulence	100
5.4.1.	The channel matrix	100
5.4.2.	OAM crosstalk comparison	102
5.5.	Aggregate capacity of the OAM-multiplexed system	106
5.5.1.	Optimal OAM sets	106
5.5.2.	Aggregate capacity	112
5.5.3.	Bit-error rate	114
5.5.4.	Aggregate capacity - fixed system power	116
5.6.	Conclusions	119
6.	BETHE FREE ENERGY APPROACH TO LDPC DECODING IN MEMORY CHANNELS	121
6.1.	Introduction	121
6.2.	Preliminaries on graphical models	126
6.2.1.	Graphical representation of a LDPC code	126
6.2.2.	The discrete ISI channel	128
6.2.3.	Graphical representation of a LDPC code on a discrete ISI channel	129
6.3.	Bethe free energy and belief propagation equations	131

TABLE OF CONTENTS—*Continued*

6.3.1.	Bethe free energy approach to the decoding of LDPC codes in a PR channel	131
6.3.2.	Algorithmic solution to the BP equations	137
6.4.	Numerical simulations	138
6.4.1.	Length-495, rate 0.875 (quasi) regular LDPC code .	139
6.4.2.	Length-4095, rate 0.82, (quasi) regular LDPC code .	140
6.4.3.	Length-2640, rate 0.50, regular LDPC code	142
6.4.4.	Length-4000, rate 0.50 regular LDPC code	143
6.4.5.	Length-2640, rate 0.5 LDPC code on PR channel $h(D) = 1 + 0.5D$	144
6.4.6.	Complexity and delay	145
6.5.	Conclusions	147
REFERENCES	149

LIST OF FIGURES

FIGURE 1.1.	Diagram of a free-space optical communication link.	18
FIGURE 1.2.	Example of a (a) collimated Gaussian beam with radius $w_0 = 4$ cm (b) after 1 km propagating in intermediate turbulence and (c) the (zoomed-in) intensity distribution at the focal plane of the collecting lens whose area is marked in (b).	21
FIGURE 2.1.	Diagram of the experimental setup to record intensity fluctuations.	32
FIGURE 2.2.	(a) Received optical power versus time for a signal with average scintillation $\sigma_I^2 = 0.178$. (b) Histogram of signal waveform, probability density function of a fitted gamma-gamma distribution, and histogram of power fluctuations obtained from simulations.	33
FIGURE 2.3.	(a) Power spectrum from experimental data with scintillation $\sigma_I^2 = 0.04$. (b) Power spectrum from experimental data with average scintillation $\sigma_I^2 = 1.05$	34
FIGURE 3.1.	Gamma-gamma probability density function for several values of σ_R	41
FIGURE 3.2.	Capacity of the FSO atmospheric channel using OOK as a function of SNR. The dotted curve is the capacity of an OOK AWGN channel.	47
FIGURE 3.3.	Capacity of the FSO atmospheric channel using OOK as a function of SNR. The dotted curve is the capacity of an OOK AWGN channel.	48
FIGURE 3.4.	Capacity vs. σ_R vs. SNR for $Q = 200$. The inset is a close-up around 37.5 dB.	49
FIGURE 3.5.	Capacity vs. σ_R vs. SNR for $Q = 32$. The inset is a close-up around 37.5 dB.	51
FIGURE 3.6.	Capacity vs. σ_R vs. SNR for $Q = 8$. The inset is a close-up around 37.5 dB.	52
FIGURE 3.7.	Capacity of the FSO atmospheric channel using OOK as a function of SNR. The dotted curve is the capacity of an OOK AWGN channel.	53
FIGURE 3.8.	BER versus SNR for $\sigma_R = 0.6$	54
FIGURE 3.9.	BER versus SNR for $\sigma_R = 0.8$	55
FIGURE 3.10.	BER versus SNR for $\sigma_R = 1.0$	56
FIGURE 3.11.	BER versus SNR for $\sigma_R = 2.0$	57
FIGURE 3.12.	BER versus SNR for $\sigma_R = 3.0$	58
FIGURE 4.1.	Diagram of a four-beam/single-receiver FSO link.	63
FIGURE 4.2.	Example of a (a) collimated Gaussian beam with $w_0 = 4$ cm (b) after 1 km propagating in turbulent air with $C_n^2 = 10^{-13} \text{ m}^{-2/3}$ and (c) the (zoomed-in) point-spread function at the focal plane of the collecting lens whose area is marked in (b).	65

LIST OF FIGURES—*Continued*

- FIGURE 4.3. Average correlation coefficient between pairs of converging beams on a single receiver, with receiver aperture (a) $D = 1$ cm, (b) $D = 3$ cm, (c) $D = 5$ cm, and (d) $D = 7$ cm. 68
- FIGURE 4.4. Average correlation coefficient versus receiver aperture diameter for (a) $C_n^2 = 2 \times 10^{-15} \text{ m}^{-2/3}$, (b) $C_n^2 = 5 \times 10^{-14} \text{ m}^{-2/3}$, (c) $C_n^2 = 2 \times 10^{-13} \text{ m}^{-2/3}$, and (d) $C_n^2 = 8 \times 10^{-13} \text{ m}^{-2/3}$ 69
- FIGURE 4.5. Average correlation coefficient among pairs of beams at 1 km, 2 km, 4 km, and 9 km with $\sigma_R^2 = 16$. Correlation estimates (dotted curves) for 2 km, 4 km, and 9 km are obtained by using the data from 1-km curve and equation (4.5). 71
- FIGURE 4.6. (a) Scintillation versus σ_R for five system configurations: (i) single-beam/point-receiver; (ii) single-beam, receiver aperture $D = \{3, 7\}$ cm and $50\mu\text{m}$ detector; (iii) four beams, receiver aperture $D = \{3, 7\}$ cm and $50\mu\text{m}$ detector. (b) Aperture averaging factor A_D and total averaging factor $A_D F_B$ versus receiver aperture D . For both (a) and (b), $z = 1$ km, $w_0 = 2.2$ cm, $L_0 = 10$ m, $l_0 = 5$ mm, $d = 15$ cm. 75
- FIGURE 4.7. Histograms of intensity fluctuations and $\Gamma\Gamma$ fit. The $\Gamma\Gamma$ density curve for the 4-beam case is predicted using the beam factor F_B . (a) $C_n^2 = 5 \times 10^{-14} \text{ m}^{-2/3}$, $D = 3$ mm, $d = 5$ cm. (b) $C_n^2 = 5 \times 10^{-14} \text{ m}^{-2/3}$, $D = 3$ mm, $d = 15$ cm. (c) $C_n^2 = 2 \times 10^{-13} \text{ m}^{-2/3}$, $D = 1$ cm, $d = 5$ cm. (d) $C_n^2 = 2 \times 10^{-13} \text{ m}^{-2/3}$, $D = 1$ cm, $d = 15$ cm. 79
- FIGURE 4.8. BER versus P_{Tx}/N_0 for a repetition code and a ST block code using four optical transmitters for the system parameters given in Table 4.5, case 1. 87
- FIGURE 4.9. BER versus P_{Tx}/N_0 for a repetition code and a ST block code using four optical transmitters for the system parameters given in Table 4.5, case 2. 88
- FIGURE 5.1. (a) Intensity distribution of a LG beam with OAM state $m = 5$ and radius $w_0 = 3$ cm. The frame is 20 cm on a side. (b) Phase distribution of the beam at $z = 0$. (c) Phase distribution of the beam at $z = 1$ km. 94
- FIGURE 5.2. Diagram of a free-space optical communication link using multiplexed OAM channels. 96
- FIGURE 5.3. (a) Intensity distribution of a distorted LG beam with initial OAM state $m = 5$ and radius $w_0 = 3$ cm. The frame is 20 cm on a side. (b) The distorted phase distribution after $z = 1$ km still preserves some of its helical structure. In this example $C_n^2 = 10^{-15} \text{ m}^{-2/3}$ 99
- FIGURE 5.4. Transmission efficiency η_{mm} as a function of OAM state, for several values of turbulence strength C_n^2 101

LIST OF FIGURES—*Continued*

FIGURE 5.5. Average crosstalk η_{mn} observed on OAM channels $n \in \mathcal{S}$ induced by transmit channel $m \in \{+1, +5, +10, +15\}$. In (a), $C_n^2 = 10^{-16} \text{ m}^{-2/3}$; in (b), $C_n^2 = 10^{-15} \text{ m}^{-2/3}$; and in (c), $C_n^2 = 10^{-14} \text{ m}^{-2/3}$	102
FIGURE 5.6. Average crosstalk η_{mn} observed on OAM channels $n \in \mathcal{S}$ induced by transmit channel $m \in \{+1, +5, +10, +20\}$. In (a), $C_n^2 = 3 \times 10^{-14} \text{ m}^{-2/3}$ and in (b), $C_n^2 = 10^{-13} \text{ m}^{-2/3}$	103
FIGURE 5.7. (a) One-dimensional intensity profile ($\phi = 0$) of some LG modes. (b) Overlap integral of <i>intensity</i> distribution of OAM state +5 and those of other OAM states. Note the similarity with the crosstalk for $m = +5$ in 5.6(b).	105
FIGURE 5.8. Optimal OAM channel sets versus P_{Tx}/N_0 , for (a) $M = 7$ and $C_n^2 = 10^{-14} \text{ m}^{-2/3}$, for (b) $M = 9$ and $C_n^2 = 10^{-14} \text{ m}^{-2/3}$, and for (c) $M = 7$ and $C_n^2 = 3 \times 10^{-14} \text{ m}^{-2/3}$	109
FIGURE 5.9. Aggregate capacity (in bits/M-channels) versus P_{Tx}/N_0 for (a) $C_n^2 = 10^{-15} \text{ m}^{-2/3}$, for (b) $C_n^2 = 10^{-14} \text{ m}^{-2/3}$, for (c) $C_n^2 = 3 \times 10^{-14} \text{ m}^{-2/3}$, and for (d) $C_n^2 = 10^{-13} \text{ m}^{-2/3}$	114
FIGURE 5.10. Bit-error rate versus P_{Tx}/N_0 in dB, with $M = 7$ at (a) $C_n^2 = 10^{-15} \text{ m}^{-2/3}$ and (b) $C_n^2 = 3 \times 10^{-14} \text{ m}^{-2/3}$	115
FIGURE 5.11. Aggregate capacity (in bits/M-channels) versus P_{Tx}/N_0 (transmit power fixed) for (a) $C_n^2 = 10^{-15} \text{ m}^{-2/3}$, (b) $C_n^2 = 10^{-14} \text{ m}^{-2/3}$, (c) $C_n^2 = 3 \times 10^{-14} \text{ m}^{-2/3}$, and (d) $C_n^2 = 10^{-13} \text{ m}^{-2/3}$	117
FIGURE 5.12. Aggregate capacity (in bits/M-channels use) versus number of OAM channels M for (a) $C_n^2 = 10^{-15} \text{ m}^{-2/3}$, (b) $C_n^2 = 10^{-14} \text{ m}^{-2/3}$, (c) $C_n^2 = 3 \times 10^{-14} \text{ m}^{-2/3}$, and for (d) $C_n^2 = 10^{-13} \text{ m}^{-2/3}$	118
FIGURE 6.1. Factor graph or bipartite graph. Circles correspond to the variable (bit) nodes and the squares correspond to the factor (check) nodes.	127
FIGURE 6.2. Graphical representation of a linear ISI channel. The output nodes y_i are a linear combination of the uncorrelated nodes x_i plus additive receiver noise.	129
FIGURE 6.3. Factor graph of a LDPC code on a ISI channel with length $L = 1$. Squares, circles, and triangles represent factor nodes, variable nodes, and ISI nodes, respectively.	130
FIGURE 6.4. BER versus SNR in dB of the MacKay(495,433) rate 0.875 (quasi) regular code performing on both a memoryless and a Dicode channel.	140
FIGURE 6.5. BER versus SNR in dB of the MacKay (4095,3358) rate 0.82 (quasi) regular code performing on both a memoryless and a Dicode channel.	141
FIGURE 6.6. BER versus SNR in dB of the Margulis (2640,1320) rate 0.50 regular code over both a memoryless and a Dicode channel.	142

LIST OF FIGURES—*Continued*

- FIGURE 6.7. BER versus SNR in dB of the MacKay (4000,2000) rate 0.50
regular code over both a memoryless and a Dicode channel. 143
- FIGURE 6.8. BER versus SNR in dB of the Margulis (2640,1320) rate 0.50
regular code over both a memoryless and a channel with $h(D) = 1 + 0.5D$. 144

LIST OF TABLES

TABLE 3.1.	Channel parameters for capacity computations for zero inner scale.	46
TABLE 3.2.	Channel parameters for capacity computations with $Q = 200$.	50
TABLE 4.1.	F_B^{-1} at beam separation $d = \{5, 7.5, 10, 12.5\}$ cm.	74
TABLE 4.2.	Prediction of F_B^{-1} for the experiment in [73].	76
TABLE 4.3.	Prediction of F_B^{-1} for the experiments in [75].	77
TABLE 4.4.	Prediction of F_B^{-1} for the experiment in [31].	80
TABLE 4.5.	Parameters used in the Monte Carlo simulations to determine BER.	86
TABLE 5.1.	Optimal channel sets for $M = 9$ and $P_{Tx}/N_0 = 20$ dB.	110
TABLE 5.2.	Optimal channel sets for $M = 9$ and $P_{Tx}/N_0 = 30$ dB.	110
TABLE 5.3.	Optimal channel sets for $M = 9$ and $P_{Tx}/N_0 = 40$ dB.	111
TABLE 5.4.	Optimum channel sets for $M = 8$ at various power levels.	112

ABSTRACT

Free-Space Optical (FSO) communication through the terrestrial atmospheric channel may offer many benefits in the wireless communications arena, like very high power efficiency; suitability for secure communications; absence of electromagnetic interference; and potentially very high bandwidth, to name a few. An optical beam propagating through the atmosphere is subject to optical turbulence. Optical turbulence is a random process that distorts the intensity and phase structure of a propagating optical beam and induces a varying signal at the receiver of an FSO communication link. This phenomenon (usually referred to as scintillation) degrades the performance of the FSO link by increasing the probability of error. In this dissertation we seek to characterize the effects of the scintillation-induced power fluctuations by determining the channel capacity of the optical link using numerical methods. We find that capacity decreases monotonically with increasing turbulence strength in weak turbulence conditions, but it is non-monotonic in strong turbulence conditions. We show that low-density parity-check (LDPC) codes provide strong error control capabilities in this channel if a perfect interleaver can be used. Multiple transmit optical beams can also be used to reduce scintillation. We characterize the spatial correlation of the atmospheric optical channel and determine a scintillation model for the multiple-beam scheme. With this model we are able to predict the effective reduction in scintillation as a function of the system design parameters. A Multi-channel FSO communications system based on orbital angular momentum (OAM)-carrying beams is studied. We numerically analyze the effects of atmospheric turbulence on the system and find that turbulence induces attenuation and crosstalk among OAM channels. Based on

a model in which the constituent channels are binary symmetric and crosstalk is a Gaussian noise source, we find optimal sets of OAM states at each turbulence condition studied, and determine the aggregate capacity of the multi-channel system at those conditions. At very high data rates the FSO channel shows some inter-symbol interference. We address the problem of joint sequence detection in partial-response (PR) channels and decoding of LDPC codes. We model the PR channel and the LDPC code as a combined inference problem. We derive the belief propagation equations that allow the simultaneous detection and decoding of a LDPC codeword in a PR channel.

1. INTRODUCTION

Free-Space Optical (FSO) communication refers to the point-to-point connection between two optical transceivers separated by an unguided physical channel. Because of the propagation properties of light, the unguided channel must be line-of-sight without obstructions in the path. The availability of the optical components used in fiber-optics makes outdoors optical links a cost-effective solution for high-rate voice and data communications. The atmospheric free-space channel is a natural medium for outdoor optical wireless communication and has generated significant research attention in the last decade as a complement to radio frequency (RF) links. With respect to wireless RF systems, microwave links have evolved considerably over the years, being able to operate at bit rates up to 500 Mb/s through a distance of 12 km [1]. With carrier frequencies beyond 10 GHz, microwave systems are limited by multi-path fading of the signal, setting a constraint on bit rate. Instead, fiber-based optical communication systems offer very low signal attenuation and very high bit rate. For example, in multi-channel (wavelength-division multiplexed) fiber-optic links, rate-distance products up to 1,000 THz-km have been achieved [2]. Despite the enormous capacity of fiber, wireless communications are still of great necessity. And this is demonstrated by the continuous growth of RF-based technology for both short and long distance links. An example of this is the development of multi-input multi-output (MIMO) RF schemes that offer an increase in capacity of tens of times with respect to its predecessors [3, 4].

Despite the improvements achieved in RF communication systems, there are many

features that make FSO systems very competitive in the short-to-medium-range arena (which we arbitrarily define as ranges from 200 m to 3 km). FSO links commonly employ spatially-coherent optical sources, whose light propagates in the form of beams. Optical beams can be adjusted by means of lenses to have little angular spreading, thus making the optical link compact in the sense that the radiated power is maintained in a small transversal area. This in turn produces a number of benefits. For instance, (i) the FSO link is extremely power efficient, that is, the receiver can collect a significant part of the transmitted power. This characteristic is, nonetheless, subject to the atmospheric conditions, as it will be explained later. (ii) The FSO link is highly suitable for secure communications, as eavesdropping can only be attained within the line-of-sight path. (iii) FSO links do not produce electromagnetic interference, and thus do not require spectrum allocation. Consequently, FSO links are license-free. (iv) Because of the higher bandwidth of optical communication systems, much like fiber-optics systems, FSO can accommodate very high data rates; easily ten times those of RF links. (v) The atmospheric optical channel is not frequency selective, at least not at the rates of current optical systems, because temporal dispersion is about 0.06 ps/(km-nm) (i.e., the group-velocity dispersion parameter is about $\beta_2 = 0.02$ ps²/km) [5].

Examples of situations in which FSO systems –often referred to also as wireless optical links or free-space laser links– may be preferred over guided links are data communications along rough terrain; secure building-to-building connections in metropolitan areas; network hubs to reach end users; temporary network installation, like those needed in conferences, emergency zones, or battle fields; and data links in marine environments. From the market perspective, local-area networks are likely to lean towards FSO technology, because of its simpler and less disruptive deployment

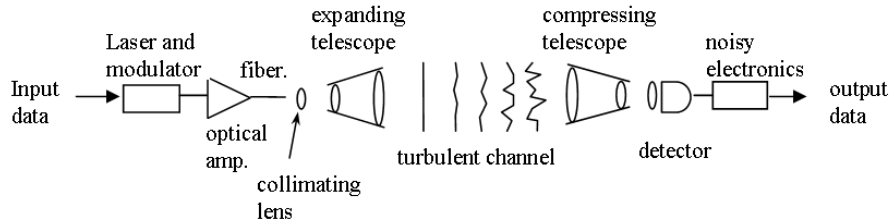


FIGURE 1.1. Diagram of a free-space optical communication link.

in comparison to fiber optics.

1.1. The free-space optical laser link

A typical FSO laser link comprises an optical transmitter, an unobstructed line-of-sight wireless channel, and an optical receiver. The schematic in Fig. 1.1 shows the components of such a system. The incoming digital data stream modulates –either directly or through a separate optical modulator– an optical source. The optical source is usually a semiconductor laser, as this class of lasers provides enough power for short-to-medium range links. Transmitted optical power requirements may range from 10 mW to 500 mW. Optical amplifiers may be used to fulfill this requirement, but as proposed in Chapter 4, an array of independent laser sources is more efficient and less expensive. An array of light-emitting diodes (LEDs) may also serve as a transmitter source. In this case the optical signal does not have a beam-like propagation characteristic; the cone of light is much broader, and the signal detection is therefore less efficient. Lasers are coherent sources, that is, they feature large spatial and temporal correlation in their wavefronts. Consequently, the power at the receiver side can be focused onto a small area, as long as there is no distortion through the propagation medium. As one would expect, a turbulent channel will distort the

signal, making the power detection less efficient.

Because any beam experiences broadening with propagation, the beam diameter is controlled at the transmitter to maximize the received power. For this purpose, the outgoing beam is expanded using a telescope to a diameter matched to the link distance. The longer the distance, the larger the required diameter. For instance, an initially collimated beam with 4 cm of diameter and wavelength $0.85 \mu\text{m}$ will increase its diameter by 20% after 1 km in vacuum. The maximum received power criterion is often relaxed by purposely increasing the beam's spreading angle to ease the process of optical alignment between the transmitter and the receiver at the cost of lower received power. This is a convenient approach in FSO systems where the misalignment caused by building sway may interrupt the data link.

The receiver consists of an objective lens system –which may include a compressing telescope and a focusing lens–; an optical filter to remove the background radiation, which otherwise increases the shot noise; an optical detector that produces an electrical current proportional to the received optical power; and the receiver electronics that deliver an estimate of the transmitted data. PIN detectors and APD detectors are the common choice given the link wavelengths used in FSO systems [6–8]. If error-control codes are used, the data stream is encoded before optical modulation and decoded after the optical-to-electrical conversion and sampling. The most common modulation formats are on-off keying (OOK) and pulse-position modulation (PPM). The latter provides a good solution in systems that do not sense the channel and thus do not operate with an optimal threshold [7–9].

1.2. The optical atmospheric channel

The reliability of terrestrial FSO communications depends on the conditions of the optical atmospheric channel. The optical atmospheric channel is a random medium. An optical beam propagating in the air experiences attenuation, scattering, angular spreading, deflection from its geometrical path, and amplitude and phase distortions. These phenomena are random both in space and time, and have a strong influence on the performance of an FSO data link. Attenuation and scattering are mainly due to the presence of water particles in the air [11]. For optical sources with near infra-red (IR) wavelengths, light haze (6km of visibility) can induce an attenuation in the order of 1 dB/km. Thin fog (2km of visibility) causes attenuation in the order of 4 dB/km. A moderate fog (500m of visibility) can attenuate the optical signal in the order of 25 dB/km [10–12]. Dense maritime fog can cause an attenuation of more than 400 dB/km at optical and near IR wavelength. Fog is, in fact, the most harmful atmospheric phenomenon for FSO communications. Although not immediately evident, rain does not attenuate an optical beam as much as fog does. For instance, the attenuation induced by a heavy rain is comparable to that of thin fog. Interestingly enough, this fact make FSO links good companions to microwave wireless links, as the latter feature the inverse behavior with respect to fog and rain. Clouds may be as harmful as fog to FSO links but these are in most cases below the cloud level. It is conjectured that the multi-scattering effect of water particles in fog may also increase the temporal dispersion of optical pulses, but this idea has not been experimentally proven to our knowledge.

The atmospheric phenomena described above are non continuous events, and their occurrence cannot be effectively predicted. For this reason they are usually treated

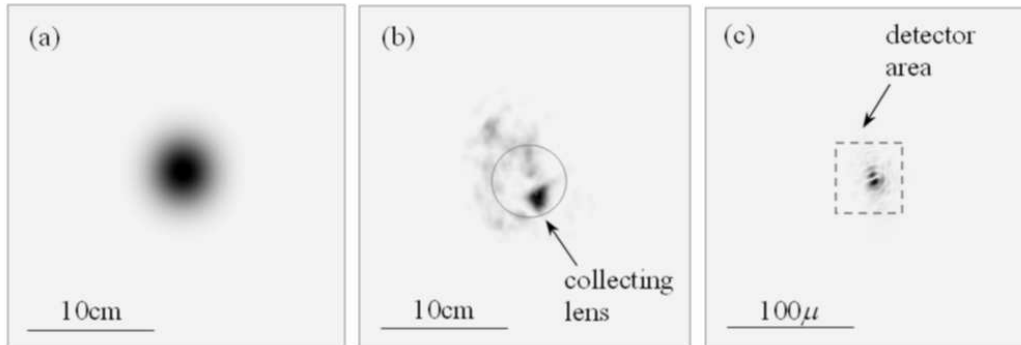


FIGURE 1.2. Example of a (a) collimated Gaussian beam with radius $w_0 = 4$ cm (b) after 1 km propagating in intermediate turbulence and (c) the (zoomed-in) intensity distribution at the focal plane of the collecting lens whose area is marked in (b).

as channel dropouts. Atmospheric turbulence, however, is a random atmospheric phenomenon that is continuously present in a terrestrial FSO link. Consequently, it has been given most of the attention in research [13–18]. In this dissertation we assume that the optical atmospheric channel is transparent (i.e., no attenuation occurs) and that it is only affected by turbulence.

Atmospheric turbulence is the random process of heat transfer within the air. In the context of optical propagation, the air’s density experiences random space and time fluctuations induced by solar heat and wind that produce an inhomogeneous refractive index distribution. The refractive index variations distort the optical signal by perturbing the phase structure of the wavefront continuously along the propagation path. At the receiver’s end, part of the light is lost as it spreads beyond the receiver’s aperture. The light collected by the objective lens produces a time-varying intensity distribution at its focal plane. Because of the finite size of the optical detector lying at the focal plane, only part of this focused light is sensed, and as a result the detector sees a time-varying signal power. For a fixed aperture and detector size, this power fluctuation, usually referred to as *scintillation*, depends on the strength of

the turbulence, the wavelength of light, and the distance traveled by the beam. Fig. 1.2 shows the effects of turbulence on the spatial intensity distribution of a Gaussian beam propagated along 1 km of turbulent air. Scintillation can severely reduce the performance of the link. Power fluctuations in the channel are independent of the optical signal and vary slowly compared to the bit time. For this reason, in situations when the channel experiences deep fades, very long bursts of errors are observed. Correlation times are in the order of milliseconds in terrestrial FSO channels.

Some of the probability density functions that approximate well the intensity fluctuations are (i) the log-normal density, which is accurate in weak turbulence; (ii) the exponential density, valid only in very strong turbulence conditions; and (iii) the gamma-gamma density, which can model a wide range of turbulence conditions. Turbulence conditions and channel models will be explicitly defined in the next chapter. Modeling scintillation both in time and in space and its dependence on turbulence strength, optical wavelength, and link distance –among other parameters– is a crucial aspect in the development of the FSO technology. In order to highlight the contributions of this dissertation we provide a more technical introduction to the underlying physics of propagation in optical turbulence and scintillation in the following chapter.

1.3. Contributions of this dissertation

Even though FSO communication systems have been under consideration since the 1970's, little research interest was given outside defense applications until recently. Only in the last fifteen years have FSO systems shown growth in commercial applications. During this time, some significant contributions have been made in areas of scintillation models [19, 21, 22], mitigation of scintillation [23–27], bit-error

rate bounds [28–30], multi-channel schemes [30–34], and beam-tracking and retro-reflecting devices [35–39].

The contributions offered by this dissertation are the following.

- Development of a reliable numerical simulation system for beam propagation in turbulence. This numerical model allowed the study of beam propagation in a large volume of the system design space, that is, considering large ranges of turbulence strengths, wavelength, receiver aperture, etc. Simulations of complete FSO systems permitted validating some scintillation models proposed in the literature, like the log-normal model valid for weak turbulence, the exponential model (or, more generally the K model) for very strong power fluctuations, and the gamma-gamma scintillation model, which covers a large range of turbulence conditions. The numerical simulation system is particularly important in showing the conditions at which the analytical models are accurate. This is covered in Chapter 2.
- Deployment of an experimental apparatus to measure the power fluctuations of a continuous laser source over a 600-m horizontal path. This experiment provided a confirmation of the analytical models as well as the numerical simulation system. It also opened the possibility of studying the temporal behavior of the power fluctuations. This is found in Chapter 2.
- Numerical determination of channel capacity in FSO channels modeled by a gamma-gamma density function and evaluation of low-density parity-check (LDPC) codes in this channel. We determined for the first time the channel capacity of a FSO system over a gamma-gamma channel assuming a point detector. We determined that capacity can be severely affected by scintillation and

that it reduces (almost) monotonically with the turbulence strength. We found that high-rate LDPC codes can provide a good solution in weak turbulence conditions, but stronger, lower-rate LDPC codes are required to compensate for medium-to-stronger turbulence conditions. These results assumed the use of a perfect interleaver, in order to break the slow temporal correlation typical of optical scintillation. This is covered in Chapter 3.

- Modeling of the spatial correlation and scintillation reduction in FSO links using multiple beams. With the purpose of mitigating scintillation, we investigated the benefits of using multiple transmitted beams projected to a single receiver. We found that the FSO channel is spatially correlated when multiple, independent sources are used. This correlation may reduce the efficacy of this scintillation reduction method without sufficient beam separation. We found that the power fluctuations of the multiple-beam system can also be modeled with the gamma-gamma density, whose parameters can be explicitly related to the spatial correlation. In the context of multiple transmitters we also adapt space-time codes previously proposed for RF MIMO channels for intensity-based modulation and find that a simple repetition scheme achieves maximum diversity if the transmitted sources are independent. This comparison assumes constant transmitted power instead of constant signal-to-noise ratio like in RF communication systems. This is covered in Chapter 4.
- Feasibility of a terrestrial multi-channel FSO link based on beams carrying orbital angular momentum (OAM). We determine the turbulence-induced channel crosstalk among OAM channels in terms of the turbulence strength and find optimal channel configurations in such conditions. We find that inner OAM chan-

nels (those with small momentum) are more resilient to turbulence than outer OAM channels. This translates to lower bit-error rates for the former. OAM-multiplexed FSO link can be a promising concept in weak turbulence conditions if a photon-efficient receiver strategy is used. This is covered in Chapter 5.

- In the context of error-correction codes, a decoding algorithm for LDPC in memory channels was derived using principles from statistical mechanics. LDPC codes will likely be essential components in FSO communication links. Starting from Bethe free energy, we derive the belief-propagation equations that permit the decoding of LDPC codes in partial-response channels, providing even better bit-error rate performance than those of the standard turbo equalization schemes, and with comparable complexity. This is covered in Chapter 6.

2. BEAM PROPAGATION AND CHANNEL MODELS

The propagation of an optical wave in an unconfined medium, as with any other electromagnetic radiation, follows the laws of diffraction. Diffraction is the phenomenon experienced by any wave that has finite lateral field extent (i.e., that is not a plane wave). Diffraction manifests as a spatially-dependent phase evolution of the electromagnetic field, and depends on the field's wavelength, its polarization, and the physical characteristics of the propagation medium. In optical propagation it is usually assumed that the medium is dielectric (i.e., non-conductive). If the medium is isotropic, propagation is independent of the field's polarization. Furthermore, in the context of optical propagation in the air, we can also assume that the medium is linear, non-magnetic and non-dispersive (i.e., permittivity is independent of wavelength). However, unlike vacuum or optical fibers, the air behaves as an inhomogeneous, time-variant medium. That is, the air's refractive index is spatially variant and its distribution changes over time. Such a medium cannot be modeled with a simple transfer function. Even more, the air's inhomogeneity and time dependence are of a stochastic nature. As mentioned in Chapter 1, this randomness originates in atmospheric turbulence. In this chapter we introduce the Kolmogorov theory for atmospheric turbulence and describe our numerical model for optical propagation in turbulence. We describe the experimental apparatus for measuring intensity fluctuations and present some of these measurements. The current analytical models for intensity fluctuations observed at the receiver of a FSO communication system are also presented, and are compared to experimental and simulation data.

2.1. Kolmogorov theory

A commonly used model of turbulence assumes that heat transfer and air motion occurs as if the air mass behaved as a group of individual cells or *eddies* of different temperature, diameter, and refractive indices. In the context of geometrical optics, these eddies may be thought of as lenses that randomly refract the optical wavefront, producing a distorted intensity profile at the receiver of a communication system. The resulting intensity fluctuations are called scintillation and are one of the most important factors that limit the performance of an atmospheric FSO communication link. The most widely accepted theory of turbulence is due to Kolmogorov [40,42–44]. This theory assumes that kinetic energy from large turbulent eddies, characterized by the outer scale L_0 , is transferred without loss to eddies of decreasing size down to sizes of a few millimeters characterized by the inner scale l_0 . The outer and inner scales define the inertial subrange, in which the energy transfer is independent of the parent flow (i.e., the flow by which energy is first injected). Below the inner scale, energy is dissipated by viscosity. The refractive index varies randomly across the different turbulent eddies and causes phase and amplitude variations to the wave front.

Because the refractive index distribution along the optical propagation path is stochastic, its characteristics are best described by a power spectrum. The fluctuations in the refractive index introduced by turbulence are of very small magnitude ($\leq 10^{-5}$) compared to the air's index of refraction (≈ 1.0003). For this reason, the power spectral density is given for the refractive index fluctuation Δn . The most important parameter that characterizes the refractive index variations is the *refractive index structure parameter* C_n^2 and depends on temperature and atmospheric pressure. This structure parameter accounts for the strength of the refractive index fluctuations,

and varies from about $C_n^2 = 10^{-17} \text{ m}^{-2/3}$ for very weak turbulence conditions (usually encountered at high altitude), to $C_n^2 = 10^{-12} \text{ m}^{-2/3}$ for very strong conditions (next to the ground at low altitude) [44]. The structure parameter is frequently assumed to be constant along horizontal paths and its average value can be measured using a scintillometer [45]. According to the Kolmogorov model, the power spectral density of the refractive index fluctuations is defined as

$$\Phi_n(\kappa) = 0.033 C_n^2 \kappa^{-11/3}, \quad 1/L_0 \ll \kappa \ll 1/l_0, \quad (2.1)$$

where κ is the spatial frequency, in m^{-1} . As indicated above, this spectrum is only defined within the inertial subrange. Because of its simplicity it is widely used in analytical calculations, but it is otherwise inconvenient if it is to be used in numerical wave propagation, as it would require the assumption of an infinitely large outer scale and an infinitely small inner scale. Several modifications to the Kolmogorov spectrum have been later proposed to extend its domain beyond the inertial subrange. Among them we highlight two that we consider most relevant. Von Kármán's model adds a damping factor that is a function of both outer and inner scales. This spectrum is defined by

$$\Phi_n(\kappa) = 0.033 C_n^2 (\kappa^2 + 1/L_0^2)^{-11/6} \exp(-\kappa^2/\kappa_m^2), \quad 0 \leq \kappa < \infty, \quad (2.2)$$

where $\kappa_m = 5.92/l_0$. Note that within the inertial subrange (2.2) reduces to (2.1). This model has been widely used in both theoretical analysis and numerical propagation as it adds increased tractability. Hill [46] developed a numerical spectrum that included a bump at spatial frequencies near $1/l_0$ observed in experimental data. This bump has been shown to have an impact in the scintillation index. Later, An-

draws [47] proposed an analytical approximation to Hill's spectrum, given by

$$\begin{aligned} \Phi(\kappa) &= 0.033 C_n^2 (\kappa^2 + 1/L_0^2)^{-11/6} \exp(-\kappa^2/\kappa_l^2) \\ &\times [1 + 1.802(\kappa/\kappa_l) - 0.254(\kappa/\kappa_l)^{7/6}], \end{aligned} \quad (2.3)$$

where $\kappa_l = 3.3/l_0$. In the numerical propagation studies presented in chapters 4 and 5 we use this modified Kolmogorov spectrum to include turbulence in the beam propagation path. This is described below.

2.2. Numerical wave propagation in turbulence

Wave propagation in an linear, isotropic, homogeneous (LIH) medium is a well known subject [44,48] and there are well defined solutions for some input fields distributions. For instance, the propagation of a zero-order Gaussian beam can be analytically determined at any propagation distance by means of the scalar wave equation and the paraxial approximation [48]. A convenient method for determining the propagated field of an arbitrary input field distribution is through the angular spectrum. This method is closely linked to linear filter theory and is based on the principle that any (physical) input field distribution can be represented by a superposition of plane waves, which are eigenfunctions of the propagation operator of a LIH medium. At propagation distance z the field $u(x, y, z)$ is, thus, expressed in the Fourier domain as

$$U(f_x, f_y, z) = \exp \left[j \frac{2\pi}{\lambda} z \sqrt{1 - (\lambda f_x)^2 - (\lambda f_y)^2} \right] U(f_x, f_y, 0) \quad (2.4)$$

where $U(f_x, f_y, z)$ is the angular (Fourier) representation of the field $u(x, y, z)$, λ is the wavelength and f_x, f_y are the spatial frequencies (in units m^{-1}). Further simplification

can be done to the propagation operator by means of the paraxial approximation, which assumes that the terms $f_x^2, f_y^2 \ll 1$. In our numerical simulations, however, we consider the full form in (2.4).

The inclusion of turbulence in numerical propagation is performed through the insertion of a number of random phase screens along the propagation path, usually at uniformly distributed steps of size Δz . These screens are samples of the turbulent volume and perturb the field in such a way that the statistical properties of the propagated field are equal to those of a field propagated through the turbulent volume. Generation of the screens is done by filtering a two-dimensional array of complex Gaussian deviates with the spectrum of the refractive index fluctuations in (2.3). A detail description of the procedure follows. In accord with the well-known *split-step Fourier method* [49], the field is propagated in vacuum (or unperturbed air) over a distance $\Delta z/2$ using (2.4). The resulting field is perturbed by the random phase screen by performing a multiplication (in spatial domain) of the former with a complex exponential whose argument is the two-dimensional random phase

$$\theta(x, y, \Delta z) = \frac{2\pi}{\lambda} \sqrt{\Delta z} n_1(x, y) \quad (2.5)$$

where

$$n_1(x, y) = \mathcal{F}^{-1} \left\{ 2\Delta x^{-1} G(\kappa_x, \kappa_y) \sqrt{\Phi(\kappa)} \right\}, \quad \kappa^2 = \kappa_x^2 + \kappa_y^2 \quad (2.6)$$

in which \mathcal{F}^{-1} indicates the inverse Fourier transform operation, Δx is the pitch of the discrete simulation grid in the transverse direction x (assumed to be equal to Δy , where y is the transverse direction orthogonal to x), $G(\kappa_x, \kappa_y)$ is an $N \times N$ array of complex Gaussian deviates and κ_x, κ_y are the spatial frequencies in the transverse directions x, y . The perturbed field is then Fourier-transformed and propagated in

free-space via (2.4) for a distance $\Delta z/2$. This completes one step of the forward wave propagation.

Several requirements have to be met in order to obtain accurate field statistics using this method. First, the phase fluctuations induced by each screen have to be small enough to maintain the validity of the Rytov approximation [40, 41, 44]. This is ensured by limiting the value of C_n^2 and/or the step size Δz . The latter implies the use of more screens along the path. For instance, on a 1-km propagation path using 25 screens (i.e., $\Delta z = 40$ m) a value $C_n^2 < 10^{-12} \text{ m}^{-2/3}$ with $\Delta x = 2$ mm guarantees a phase change $\theta \ll 2\pi$. Another required condition –which is also limiting in practical cases– is imposed by the energy spread due to propagation. Transverse lengths of the propagation volume must be large enough to account for the additional beam spreading induced by turbulence and proper handling of the energy that reaches the volume boundaries must be ensured. This is achieved by attenuating the field on the screen’s edges such that power leakage from one side to the opposite from Fourier-transform operations is avoided. An important requirement in cases where measuring scintillation in the intermediate-to-strong regime is of interest consists of setting $\Delta x < l_0/2$, so that the small scale fluctuations are properly sampled.

It is worth noting that random phase screens are uncorrelated from each other. Because the large-scale eddies can occupy several meters along the path, the volume is properly sampled if the screens are separated at distances $\Delta z > L_0$, that is, at steps at which the spatial distribution of eddies can be expected to be independent from each other. In our simulations we use $\Delta z = 2 L_0$, while ensuring the other conditions are still satisfied. A thorough numerical analysis of these conditions is given by Belmonte in [50].

The simulations presented in Chapters 4 and 5 also include the interaction with

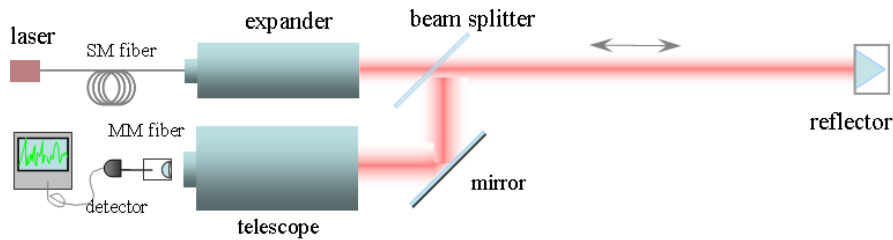


FIGURE 2.1. Diagram of the experimental setup to record intensity fluctuations.

optical elements in both the transmitter and the receiver, as well as with the geometry of the optical detector.

2.3. Scintillation experiment

In the interest of understanding the underlying physical effects of turbulent propagation on a laser source, an experimental apparatus was deployed at the campus of the University of Arizona. The system comprises a single-mode continuous-wave laser source with $\lambda = 650$ nm, whose pig-tailed output is connected to a beam expander, as shown in Fig. 2.1. The beam expander is pointed to a 2-inch (1 inch = 2.54 cm) corner-cube reflector fixed to a lighting pole 300 m away. The reflected beam (which by corner-cube design is reflected back in the same direction) is captured by a telescope and focused on one end of a multi-mode fiber. The other end of the fiber is connected to a low-bandwidth silicon-based optical detector. The signal delivered by the detector is recorded in an oscilloscope. The path length is, therefore, $z = 600$ m.

The laser source featured a transmit power of only 2 mW, which proved to be enough to get a return signal with large signal-to-noise ratio for a 20MHz bandwidth in clear days. This, however, was subject to critical beam alignment at both

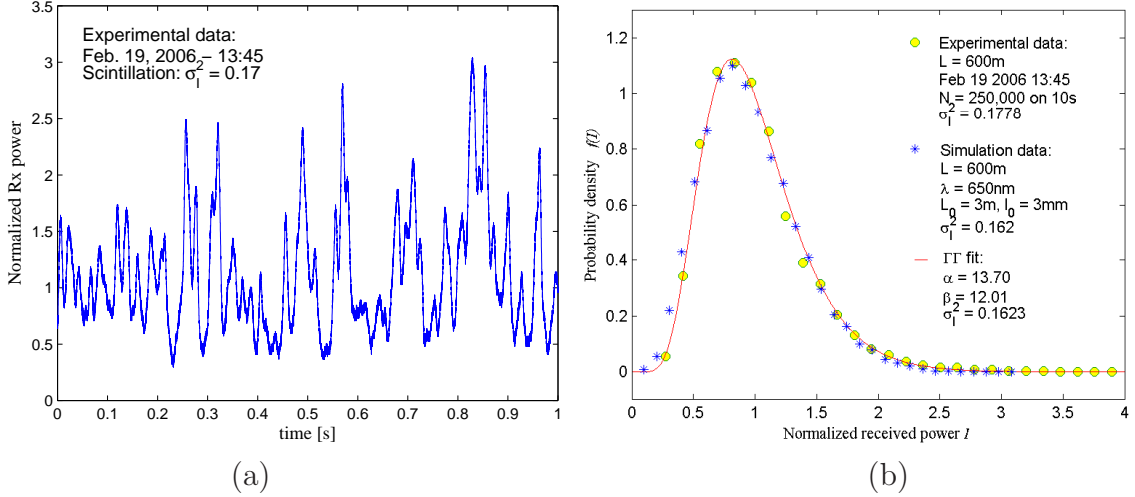


FIGURE 2.2. (a) Received optical power versus time for a signal with average scintillation $\sigma_I^2 = 0.178$. (b) Histogram of signal waveform, probability density function of a fitted gamma-gamma distribution, and histogram of power fluctuations obtained from simulations.

the transmitter-reflector link and the free-space-to-fiber coupling at the receiver end. Because of the narrow field of view imposed by the free-space-to-fiber coupling at the receiver, no optical filters were necessary to reduce the background radiation. At every data recording we measured this background signal (for later subtraction) whose average showed in all cases to be very small in comparison to the laser signal. Data were recorded in intervals no longer than 20 seconds in order to keep sampling frequency above 5 kHz, given the finite sample count of the oscilloscope. Intensity waveform recordings were performed on several months at different atmospheric conditions. In Figure 2.2 (a) we present a sample of a recorded optical signal distorted by turbulence with a scintillation $\sigma_I^2 = 0.178$. In Fig. 2.2(b) the normalized histogram of the recorded optical power is plotted along with the histogram obtained from numerical simulations of a Gaussian beam in turbulence. A gamma-gamma density function fitted to the experimental data is also included in the plot. This density function

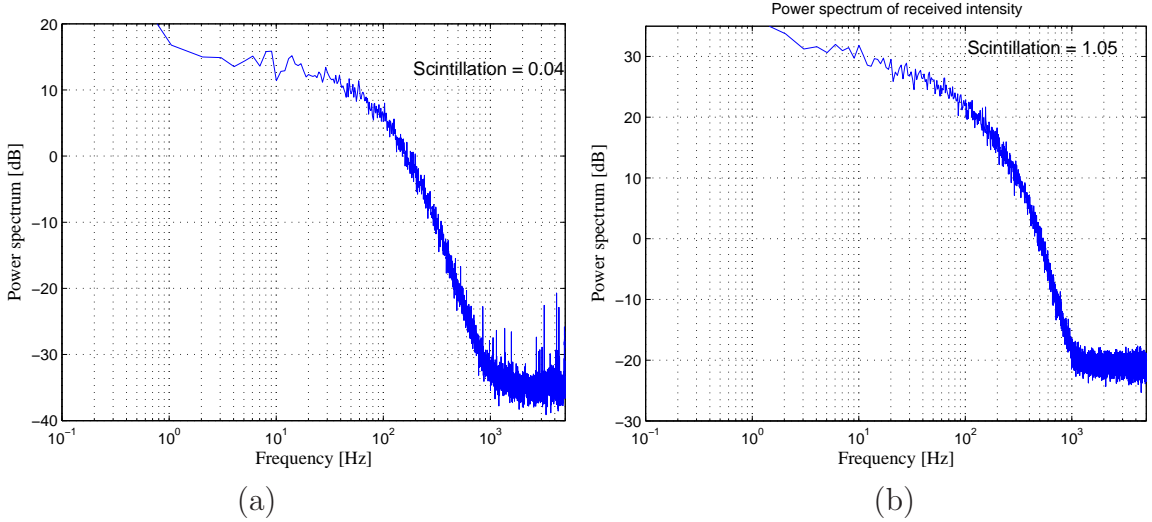


FIGURE 2.3. (a) Power spectrum from experimental data with scintillation $\sigma_I^2 = 0.04$. (b) Power spectrum from experimental data with average scintillation $\sigma_I^2 = 1.05$.

will be introduced in the following section. We note that good matching between the gamma-gamma distribution, simulations, and experimental data is achieved as long as small receiver apertures are considered, that is, aperture size much smaller than the beam spot. With larger sizes, aperture averaging reduces the extent of the fluctuations, thus changing the statistical properties. Analytical models like the gamma-gamma distribution are not accurate when a large fraction of the transmitted power is collected.

To highlight the temporal characteristics of the optical power fluctuations, Figure 2.3 shows the temporal power spectra for two cases, recorded at different days. In (a) the data has $\sigma_I^2 = 0.04$ (very weak). In (b), the signal features a much stronger scintillation, with $\sigma_I^2 = 1.05$. Note that both spectra show very similar characteristics. We have observed that the power fluctuations never show frequency content beyond 2 kHz. Furthermore, the energy of the spectrum is often contained below 1 kHz and appears to be uncorrelated with the strength of the turbulence. We conjecture that

temporal correlation is a function of the wind velocity transverse to the optical path, but this subject is not studied in this dissertation.

2.4. Analytical intensity fluctuation models

In clear atmosphere the variations of received power are the most important feature of the FSO channel. For this reason, formalizing accurate analytical models for scintillation has taken a good fraction of the community's research effort. Among the many models available, we briefly describe three probability density functions of practical importance.

2.4.1. Lognormal density

The lognormal probability density function is a two-parameter density. It is related to the normal distribution in that if I is a lognormal-distributed random variable with parameters μ and σ_X , then the random variable $\psi = \log(I)$ is normal-distributed with parameters μ and σ_X . The lognormal function is given by

$$f_I(I) = \frac{1}{I} \frac{1}{\sqrt{2\pi\sigma_X^2}} \exp\left[-\frac{(\ln I - \mu)^2}{2\sigma_X^2}\right], \quad I > 0 \quad (2.7)$$

The validity of the lognormal density is linked to the underlying physical model in which the field variations along the propagation path can be understood as many consecutive small perturbations. As described by the Rytov approximation [40], the log-amplitude fluctuations follow a normal distribution due to the Central Limit theorem. Because of the exponential relation between the intensity and the log-amplitude of the field, the perturbed optical intensity has a lognormal distribution. The validity

of this assumption, and therefore the accuracy of this model, applies only to the weak turbulence regime.

2.4.2. Exponential density

Because of the wide-spread use of this distribution, we limit our comments to say that this density is adequate to model the intensity fluctuations in very strong turbulence conditions (achieved by either a large C_n^2 or a long propagation path), usually referred to as the *saturation regime*. Its applicability is limited but its simple functional form gives great flexibility in analytical studies. The density is given by

$$f_I(I) = \frac{1}{\mu} \exp\left(-\frac{I}{\mu}\right) \quad (2.8)$$

2.4.3. Gamma-gamma density

The gamma-gamma density function has gained significant popularity since Al-Habash *et al.* proposed it to model intensity fluctuations over a wide range of turbulence conditions, while relating its parameters to the physical conditions of the turbulence [51]. The density is given by the expression

$$f(I) = \frac{2(\alpha\beta)^{(\alpha+\beta)/2}}{\Gamma(\alpha)\Gamma(\beta)} I^{(\alpha+\beta)/2-1} K_{\alpha-\beta}\left(2\sqrt{\alpha\beta I}\right), \quad I > 0 \quad (2.9)$$

where I is the received optical power, α and β are the parameters, Γ is the Gamma function, and $K_{\alpha-\beta}$ is the modified Bessel function of the second kind and order $\alpha-\beta$. This distribution can accurately model intensity fluctuations from weak turbulence conditions to very strong conditions. Its accuracy in the *focusing regime* (in which scintillation finds its maximum) is lower. Still, among scintillation models it covers

the largest range of turbulence conditions and for this reason we make use of it in this dissertation. Chapter 3 presents a complete description of this model.

3. CHANNEL CAPACITY AND LDPC CODES IN TURBULENT CHANNELS

3.1. Introduction

To design a high-performance communication link for the atmospheric FSO channel, it is of great importance to characterize the channel from the perspective of information theory. In this Chapter we study the Shannon capacity of the atmospheric FSO link using an accurate scintillation model based on the gamma-gamma probability distribution function to predict the fluctuation of the intensity signal [29, 51]. This statistical representation not only fits the channel scintillation accurately, but its parameters can be related to the physical conditions of turbulence by a scintillation model proposed by Andrews *et al.* [22]. Previous studies have considered the use of the lognormal distribution [28], but its validity is limited to weak turbulence [22, 29, 51]. To estimate the channel capacity, a system based on OOK modulation and a point detector is studied. The noise in the receiver electronics is modeled as additive white Gaussian noise (AWGN).

A broad range in turbulence strength –from the weak turbulence regime through the saturation regime– is considered. We show that atmospheric turbulence reduces the channel capacity, and the latter reaches an asymptotic limit in the saturation regime.

The probability of bit error under several turbulence conditions is determined using Monte Carlo simulations. We demonstrate that appropriate forward error correction (FEC) codes can provide a significant coding gain in SNR with respect to an uncoded system. In particular, we present two error correction systems based on low-

density parity-check (LDPC) codes: (i) LDPC codes designed using the MacNeish-Mann theorem and (ii) block-circulant codes; both codes we proposed recently for fiber-optics communications [52, 53]. The codes have quasi-cyclic structure of parity-check matrix, high code rate, low encoder and decoder complexity, and excellent error correction capabilities. For more details on LDPC codes, the interested reader is referred to Refs. [52–55]. The bit-error rate (BER) performance of LDPC codes are compared against Reed-Solomon (RS) codes of similar rates and lengths. The LDPC codes provide significant coding gain improvement compared with standard RS codes, ranging from about 6 dB to about 14 dB, depending on the turbulence strength.

The Chapter is organized as follows. In Section 3.2 we describe the statistical model for the intensity variations caused by atmospheric turbulence. The zero and the nonzero inner scale models are presented in subsections 3.2.1 and 3.2.2, respectively. In Section 3.3 we present the computation of channel capacities based on the statistical model and we explain the implications on high bit-rate communication links. In Section 3.4 we present a comparison of BER performances of the FEC codes and the uncoded link for some channels. In Section 3.5 we summarize our work and provide our conclusions.

3.2. Atmospheric turbulent channel modeling

As described in Chapter 2, Kolmogorov theory characterizes the loss-less turbulent air motion between the outer scale L_0 and the inner scale l_0 . Outer scale is assumed to be infinite in this Chapter. We consider zero and nonzero inner scale conditions. Understanding the turbulence effects under zero inner scale is important, as it represents a physical bound for the optical atmospheric channel and as such it has been

of interest to researchers [19, 22, 51].

To account for the strength of the turbulence, we use the unitless Rytov variance, given by [40, 42]

$$\sigma_R^2 = 1.23 C_n^2 k^{7/6} L^{11/6}, \quad (3.1)$$

where $k = 2\pi/\lambda$ is the wavenumber, λ is the wavelength, L is the propagation distance, and C_n^2 is the refractive index structure parameter, which we assume to be constant for horizontal paths. Although the Rytov variance has been used as an estimate of the intensity variance in weak turbulence, we use it here only as an intuitive metric that brings together all the physical operating conditions. Throughout the Chapter we often refer to σ_R simply as turbulence strength.

To characterize the FSO channel from a communication theory perspective, it is useful to give a statistical representation of the scintillation. The reliability of the communication link can be determined if we use a good probabilistic model for the turbulence. Several probability density functions (PDFs) have been proposed for the intensity variations at the receiver of an optical link [19–21, 56–58]. Al-Habash et al. [51] proposed a statistical model that factorizes the irradiance as the product of two independent random processes each with a Gamma PDF. The PDF of the intensity fluctuation is therefore [as defined in (2.9)]

$$f(I) = \frac{2(\alpha\beta)^{(\alpha+\beta)/2}}{\Gamma(\alpha)\Gamma(\beta)} I^{(\alpha+\beta)/2-1} K_{\alpha-\beta} \left(2\sqrt{\alpha\beta I} \right), \quad I > 0 \quad (3.2)$$

where I is the signal intensity, α and β are parameters of the PDF, Γ is the gamma function, and $K_{\alpha-\beta}$ is the modified Bessel function of the second kind of order $\alpha - \beta$.

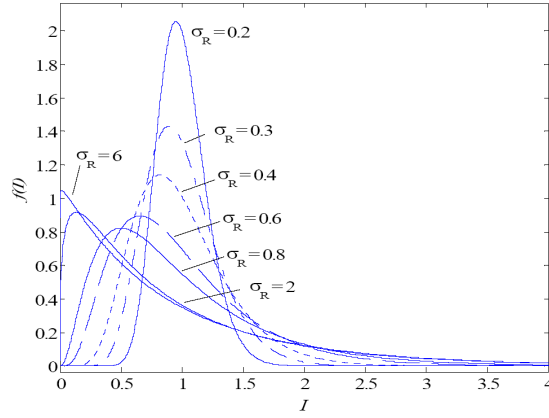


FIGURE 3.1. Gamma-gamma probability density function for several values of σ_R .

3.2.1. Zero inner scale

The parameters α and β of the PDF that predicts the scintillation experienced by plane waves in the case of $l_0 = 0$, are given by the expressions [43, 51]

$$\alpha = \left\{ \exp \left[\frac{0.49\sigma_R^2}{\left(1 + 1.11\sigma_R^{12/5}\right)^{7/6}} \right] - 1 \right\}^{-1},$$

$$\beta = \left\{ \exp \left[\frac{0.51\sigma_R^2}{\left(1 + 0.69\sigma_R^{12/5}\right)^{5/6}} \right] - 1 \right\}^{-1}. \quad (3.3)$$

This is a significant result, as the PDF of the intensity fluctuations at the receiver can be predicted from the physical turbulence conditions. The predicted distribution matches very well the distributions obtained from numerical propagation simulations [19, 51]. The predicted gamma-gamma distribution fits even better than the log-normal distribution in the weak turbulence regime. The poorest fit with experiments occurs in the focusing regime, where σ_R is about 2 to 3.

Figure 3.1 shows the predicted distribution for a few instances of the turbulence

strength. For $\sigma_R \ll 1$, the gamma-gamma distribution resembles a log-normal distribution. As the turbulence strength increases the distribution skews towards smaller values of irradiance. The distribution of the intensity fluctuations asymptotically approaches an exponential distribution as σ_R tends to infinity.

3.2.2. Nonzero Inner Scale

In the presence of non-zero inner scale, the model must be modified to account for the slight change in the power spectrum of the refractive index variations. The PDF model is again a gamma-gamma distribution, but its parameters are now given by [43, 51]

$$\alpha = \left\{ \exp \left[\sigma_{\ln X}^2 \right] - 1 \right\}^{-1},$$

$$\beta = \left\{ \exp \left[\frac{0.51 \sigma_P^2}{\left(1 + 0.69 \sigma_P^{12/5} \right)^{5/6}} \right] - 1 \right\}^{-1}, \quad (3.4)$$

where $\sigma_{\ln X}^2$ is given by

$$\sigma_{\ln X}^2 = 0.16 \sigma_R^2 \left(\frac{\eta_x Q}{\eta_x + Q} \right)^{7/6} \left[1 + 1.75 \left(\frac{\eta_x Q}{\eta_x + Q} \right)^{1/2} - 0.25 \left(\frac{\eta_x Q}{\eta_x + Q} \right) \right], \quad (3.5)$$

and

$$\eta_x = \frac{2.61}{1 + 0.45 \sigma_R^2 Q^{1/6}}, \quad Q = \frac{10.89 L}{k l_0^2}. \quad (3.6)$$

For the second expression in (3.4), σ_P^2 is given by

$$\sigma_P^2 = 3.86 \sigma_R^2 \left\{ (1 + 1/Q^2)^{11/12} \left[\sin \left(\frac{11}{6} \tan^{-1} Q \right) + \frac{1.51}{(1 + Q^2)^{1/4}} \sin \left(\frac{4}{3} \tan^{-1} Q \right) - \frac{0.27}{(1 + Q^2)^{7/24}} \sin \left(\frac{5}{4} \tan^{-1} Q \right) \right] - 3.5 Q^{-5/6} \right\}. \quad (3.7)$$

3.3. Channel Capacity of an Atmospheric FSO Channel

The capacity of a noisy channel relates the SNR of the received signal to the average rate of symbols per channel use that can be recovered with an arbitrarily small probability of error. If we use a binary alphabet, the maximum rate we can achieve is 1 bit/channel use and this limit is realized only for infinite SNR. The channel capacity can also be expressed in terms of bandwidth efficiency (bits/s/Hz) if the frequency response of the channel is known. In most cases the channel capacity can only be achieved by using long error-correction codes. To be able to reduce the BER to an arbitrarily small value at any given SNR, the rate R of the code has to be smaller than the channel capacity C at that SNR [59]. We define $\text{SNR} = E[I]^2/N_0$, where $E[\cdot]$ is the expectation operator, I is the received intensity, and N_0 is the electrical noise power.

We are interested in determining the channel capacity of the FSO channel for different turbulence conditions. This can lead to better understanding of the effects of turbulence in a high-bit-rate optical communication system and helps to learn about on which conditions the channel can be more effectively utilized. Some work on capacity estimation has been previously done under weak turbulence by using the lognormal statistical model [28]. We consider the complete range of turbulence

strength, from very weak turbulence to the saturation regime. It is intuitively clear that higher turbulence strength will lead to a reduction in channel capacity; however, we seek a quantitative description of this capacity reduction. Below we describe the assumptions under which we determine the channel capacity of the optical atmospheric channel.

3.3.1. Channel Capacity Calculation

The assumptions made to determine channel capacity are as follows:

(i) The received intensity samples are treated as independent and identically distributed (i.i.d.); that is, the channel is assumed to be uncorrelated. In reality, at high bit rates the channel has temporal correlation and consecutive bits propagate through similar channel conditions [16]. Because of the lack of literature in regard of the temporal statistics in the FSO channel and the difficulty of tractability of multidimensional joint distributions, we consider an i.i.d. case, as it will produce a lower bound in capacity. This approach is valid because temporal correlation can in practice be overcome by means of long interleavers. Hence, this type of correlation does not place a constraint on capacity [60, 61]. For brief periods of time the instantaneous capacity may be reduced or increased due to scintillation. If the bit time is much smaller than the correlation time, the channel can be sensed and this information can be used to improve the detection of further bits, yielding a higher capacity. However, without the knowledge of the temporal statistics, the receiver uses a symbol-by-symbol detection scheme.

(ii) The marginal distribution of the channel is known. This means that we can determine the turbulence conditions and can predict the parameters of the gamma-gamma distribution. This assumption is sound, as all the physical parameters can

be effectively measured.

(iii) We assume an intensity-based OOK modulation scheme and model the noise at the receiver as AWGN. The statistical channel can be represented by the expression

$$Y = I X + N, \quad I > 0, \quad (3.8)$$

where Y is the received signal, I is a random variable representing the intensity gain, X is the transmitted binary signal, and N is the noise at the receiver. We assume for simplicity that the responsivity factor of the detector is equal to 1. If a 0 is transmitted, the received signal is given by noise alone. If a 1 is transmitted, the channel will randomly scale the input signal by a factor that follows a gamma-gamma distribution according to the model described above. Channel capacity for a binary-input continuous-output channel is defined as the maximum of the mutual information between X and Y over all input distributions [59]. In this case, the input distribution is binomial. The mutual information for this channel is, therefore,

$$I(Y; X) = \int_0^\infty \sum_{x=0}^1 f_Y(y|x) P_X(x) \log_2 \frac{f_Y(y|x)}{\sum_{z=0}^1 f_Y(y|z) P_X(z)} dy, \quad (3.9)$$

where $f_Y(y|x)$ is the conditional distribution of the output Y given the input X , and $P_X(x)$ is the probability of $X = x$. The conditional distribution $f_Y(y|x = 0)$ is a zero-mean Gaussian distribution, and $f_Y(y|x = 1)$ is the distribution of $I + N$. We determine $f_Y(y|x = 1)$ numerically, using the fact that the PDF of the sum of two random variables is the convolution of their PDFs [62]. Because the channel is asymmetric, the input distribution that maximizes the mutual information is no longer $P_X(0) = P_X(1) = 0.5$. In fact the optimal input distribution varies with the turbulence strength and the SNR, and it ranges from about $P_X(0) = 0.56$ for strong

TABLE 3.1. Channel parameters for capacity computations for zero inner scale.

σ_R	α	β	σ_I^2
0.2	51.91	49.11	0.04
0.4	14.11	12.54	0.156
0.6	7.38	5.86	0.329
0.8	5.23	3.59	0.523
1.0	4.39	2.56	0.706
1.5	4.01	1.61	1.025
2.0	4.34	1.31	1.171
3.0	5.49	1.12	1.242
4.0	6.76	1.06	1.234
5.0	8.05	1.03	1.214
6.0	9.31	1.02	1.194
10.0	14.11	1.0033	1.138

turbulence and low SNR to about $P_X(0) = 0.5$ for weak turbulence and high SNR. We determine the capacity C from (3.9) using Monte Carlo integration [63].

3.3.2. Capacity for Zero Inner Scale

Table 3.1 summarizes the turbulence conditions considered and the corresponding distribution parameters for $l_0 = 0$. The final column indicates the variance of the intensity fluctuations, usually referred to as scintillation index. Figure 3.2 shows the channel capacity for plane waves considering OOK modulation and a point receiver, expressed as bits/channel use versus SNR in decibels. For the sake of a comparison, the capacity of an OOK AWGN channel with the same modulation scheme is also shown. Each curve represents the maximum possible coding rate at which the probability of error can be made arbitrarily small for a given SNR and turbulence strength.

Under weak turbulence the capacity approaches that of a binary AWGN channel as

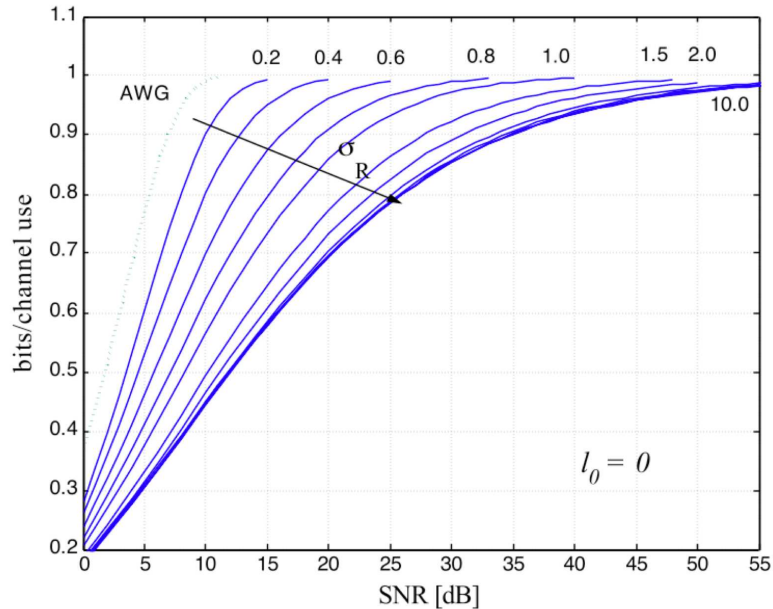


FIGURE 3.2. Capacity of the FSO atmospheric channel using OOK as a function of SNR. The dotted curve is the capacity of an OOK AWGN channel.

the turbulence strength decreases. We see that as σ_R increases, the capacity decreases. This in turn will result in worse performance of the communication link. Under weak turbulence the capacity decreases more rapidly as σ_R increases, for a given rate. It is interesting to see that beyond the weak turbulence regime ($\sigma_R > 2$), the capacity curves keep to higher SNR values but at smaller steps. For very strong turbulence, capacity curves asymptotically approach a limit. This means that regardless of the propagation distance and turbulence strength, the performance will not drop below this asymptotic limit, assuming that attenuation is compensated.

Another useful way to analyze the capacity is to plot the SNR required to achieve a constant rate (in bits/channel use) as a function of σ_R . This is shown in Fig. 3.3. For any given rate, the required SNR grows more rapidly for small σ_R , meaning that

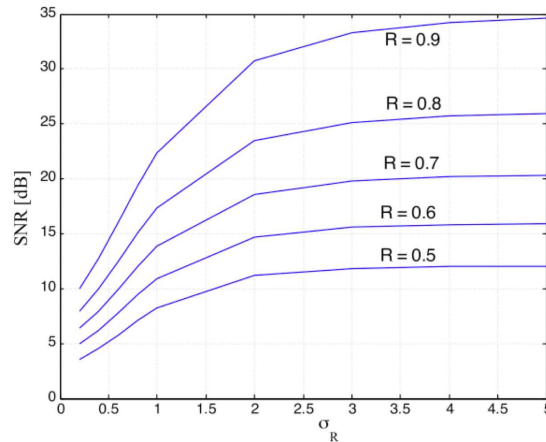


FIGURE 3.3. Capacity of the FSO atmospheric channel using OOK as a function of SNR. The dotted curve is the capacity of an OOK AWGN channel.

most of the degradation in capacity occurs in weak turbulence. From the curves of Fig. 3.3, for fixed SNR, it can be concluded that there exists a monotonic decrease of capacity as turbulence strength σ_R increases. At high rates, we find that the SNR suffers stronger degradation compared with that at lower rates. We see that at a rate $R = 0.5$ the required SNR is almost constant in strong turbulence ($\sigma_R > 2$). However, at a rate $R = 0.9$, the SNR required increases significantly up to a turbulence strength of about $\sigma_R = 4$. It appears that the power penalty for using higher code rate FEC codes is large. It is worth recalling, however, that FEC codes incur a SNR penalty inversely proportional to the rate. Moreover, for a reasonable throughput, high-rate codes are necessary.

The curves presented in Figs. 3.2 and 3.3 are universal, that is, they apply for any combination of propagation length L , wavelength λ , and structure parameter C_n^2 , as

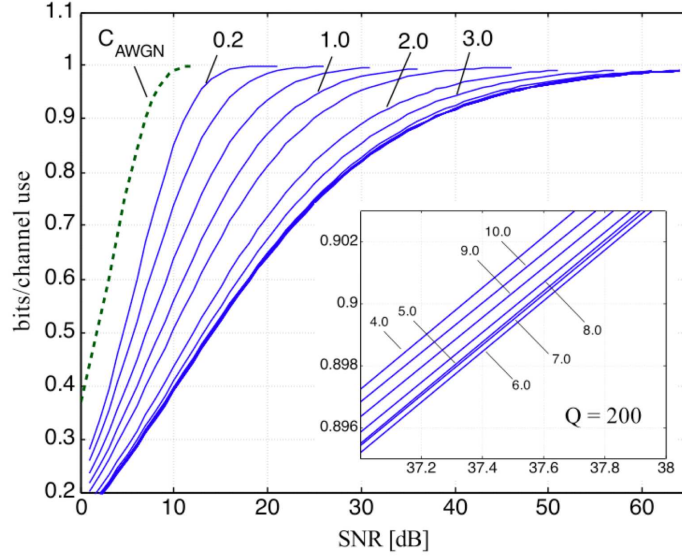


FIGURE 3.4. Capacity vs. σ_R vs. SNR for $Q = 200$. The inset is a close-up around 37.5 dB.

long as L is much larger than λ , so that the geometrical optics approximation used in deriving (3.3) holds. In practice, the refractive index structure parameter C_n^2 varies from about $10^{-17} \text{ m}^{-2/3}$ for very weak turbulence to about $10^{-12} \text{ m}^{-2/3}$ for strong turbulence. For instance, a value of $\sigma_R = 1$ can be obtained with $C_n^2 = 8 \times 10^{-14} \text{ m}^{-2/3}$, $L = 500 \text{ m}$, and $\lambda = 780 \text{ nm}$.

3.3.3. Capacity for nonzero inner scale

For non-zero l_0 , the capacity is computed as in the previous section but the parameters of the PDF are predicted according to (3.4). Because there is an additional degree of freedom, the capacity cannot be represented by a single set of curves as before. It is convenient to use the parameter Q , defined by (3.6), as the free variable as it accounts for propagation distance, inner scale, and wavelength. We present the capacity for

TABLE 3.2. Channel parameters for capacity computations with $Q = 200$.

σ_R	α	β	σ_I^2
0.2	45.79	41.55	0.0464
0.4	12.87	10.67	0.179
0.6	6.82	5.05	0.374
0.8	4.75	3.14	0.596
1.0	3.83	2.29	0.811
1.5	3.04	1.50	1.214
2.0	2.88	1.25	1.422
3.0	2.98	1.09	1.557
4.0	3.18	1.05	1.571
5.0	3.41	1.03	1.555
6.0	3.62	1.02	1.534
7.0	3.82	1.01	1.512
8.0	4.00	1.006	1.493
9.0	4.17	1.004	1.475
10.0	4.34	1.002	1.459

three values of Q , namely 200, 32, and 8. Table 3.2 shows the distribution parameters we consider for $Q = 200$. The values of Q considered above are obtained, for instance, with $L = 592$ m, $\lambda = 780$ nm, and inner-scale values 2 mm, 5 mm, and 10 mm, respectively. Because σ_R depends on L and λ , the free parameter will be C_n^2 . Given the values above, varying σ_R from 0.2 to 10 is equivalent to varying C_n^2 from 2×10^{-15} m^{-2/3} to 6×10^{-12} m^{-2/3}. For smaller values of C_n^2 , the curve of capacity is expected to come nearer the capacity of the AWGN channel.

Figures 3.4, 3.5, and 3.6 show the capacity curves for $Q = 200$, 32, and 8, respectively. These curves show a similar behavior to that of the zero inner-scale case. There are, however, some noteworthy differences. The capacity curves experience a stronger shift to higher SNR values as Q decreases. In other words, for a given σ_R , capacity decreases as Q decreases. For instance, at $\sigma_R = 1$, a rate 0.8 bits/channel

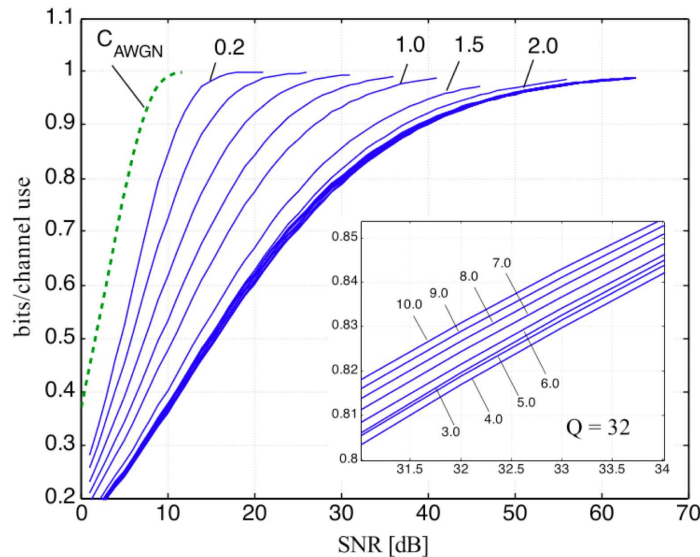


FIGURE 3.5. Capacity vs. σ_R vs. SNR for $Q = 32$. The inset is a close-up around 37.5 dB.

use is achieved at an SNR = 17 dB for $Q = 200$ (Fig. 3.4), at 21.1 dB for $Q = 32$ (Fig. 3.5), and at 21.6 dB for $Q = 8$ (Fig. 3.6). If L , k , and C_n^2 are kept constant, we can conclude that capacity decreases as the inner scale increases.

Beyond the focusing regime ($\sigma_R > 2$), the capacity is no longer monotonic with σ_R . Within the focusing regime, scintillation finds its maximum and decays as σ_R continues to grow. The maximum scintillation reached at this conditions has a strong dependence on l_0 and therefore, on Q . The non-monotonicity is subtle for $Q = 200$ (Fig. 3.4) which is associated with a small l_0 , but very noticeable at $Q = 8$, for which l_0 is larger for a fixed L (Fig. 3.6). The latter case produces a large scintillation value σ_I^2 in comparison to that of the saturation regime (i.e., at large σ_R), thus causing a visible minimum in capacity. The insets in Figs. 3.4, 3.5, and 3.6 show detailed sections of the capacity curves. Beyond certain σ_R , the curves shift to lower values

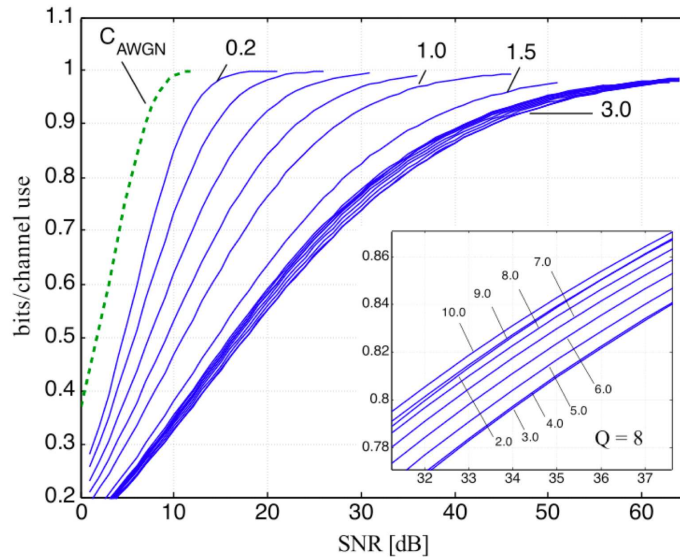


FIGURE 3.6. Capacity vs. σ_R vs. SNR for $Q = 8$. The inset is a close-up around 37.5 dB.

of SNR. The value of σ_R at which this occurs decreases with Q . This trend is more clearly seen by plotting SNR versus σ_R for curves of constant rate. This is shown in Fig. 3.7. For $Q = 200$ [Fig. 3.7(a)], the maximum SNR occurs around $\sigma_R = 6$; for $Q = 32$ [Fig. 3.7(b)], the maximum occurs around $\sigma_R = 4$; for $Q = 8$ [Fig. 3.7(c)], the maximum appears to be between $\sigma_R = 3$ and $\sigma_R = 4$. Table 3.2 summarizes the turbulence parameters at which capacity is computed for $Q = 200$. We estimate the error in the capacity –assuming the validity of the gamma-gamma model– to be lower than 1%.

3.4. Efficient LDPC error-correction codes

We have found in the previous section that capacity can be severely reduced with scintillation. Hence, the FSO probability of bit error can be very high, even for

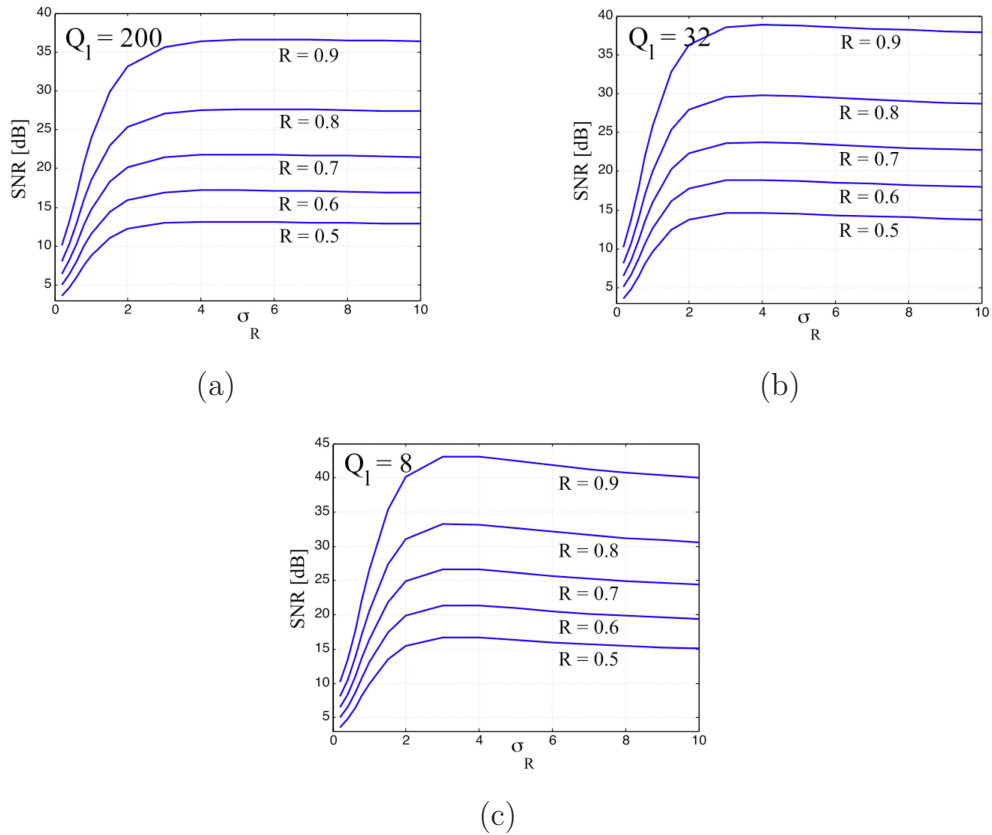


FIGURE 3.7. Capacity of the FSO atmospheric channel using OOK as a function of SNR. The dotted curve is the capacity of an OOK AWGN channel.

large values of SNR [64]. This renders the atmospheric FSO channel useless, as such high SNR is not attainable in practice. Therefore, powerful error-correction codes are necessary. Our analysis will focus on two classes of codes: RS codes and LDPC codes [52, 53, 65]. Some Turbo codes [66] have already been evaluated for use on the FSO channel under weak turbulence [28].

We evaluate two LDPC error-correction codes for the FSO channel that can efficiently operate across all turbulence regimes. These codes were recently proposed for bursty channels, such as fiber-optics channel operating at 40 Gb/s or higher, out-

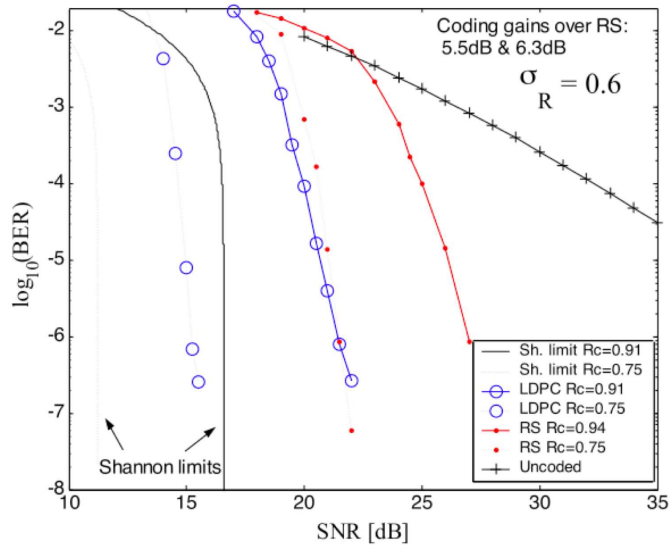


FIGURE 3.8. BER versus SNR for $\sigma_R = 0.6$.

performing turbo product codes of comparable code rates [52, 53]. The atmospheric FSO channel also shows bursty-error prone behavior, making these codes appealing for this channel. They also have large minimum distances, have a regular structure and are designed using the concepts of combinatorial design [54]. These codes also have low encoding and decoding complexity, which is a desirable feature for implementation in actual FSO communication systems. Namely, the quasi-cyclic structure of parity-check matrix of the considered LDPC codes facilitates the implementation, because only the dimension of the permutation matrix and the exponents are to be memorized. For the details of an LDPC chip architecture an interested reader is referred to [67]. The codeword lengths are 2025 bits and 4320 bits long, with rates 0.91 and 0.75, respectively.

Figure 3.8 shows the BER curves for a turbulence strength of $\sigma_R = 0.6$ (weak turbulence) of the rate 0.91 LDPC, the rate 0.75 LDPC, a rate 0.94 RS (255, 239)

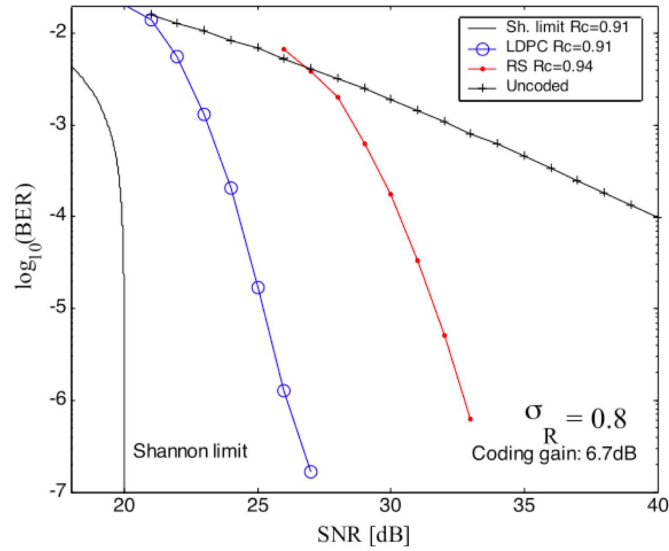


FIGURE 3.9. BER versus SNR for $\sigma_R = 0.8$.

code, and a rate 0.75 RS (255, 191) code. The BER of the uncoded system is also depicted. The Shannon limit for rates 0.91 and 0.75 are also plotted and represent the best performance one can achieve with an infinitely long FEC code. The coding gain of the rate 0.91 LDPC code with respect to the rate 0.94 RS code is 5.5 dB, and the coding gain of the rate 0.75 LDPC code with respect to the rate 0.75 RS code is 6.3 at $\text{BER} = 10^{-7}$. The coding gain of the LDPC codes over an uncoded system is more than 20 dB, which is an outstanding improvement, as these coding gains are rarely seen in other channels. The performances of the LDPC codes are 5 dB and 4 dB away from their respective Shannon limits.

The BER performance for a turbulence strength of $\sigma_R = 0.8$ (weak turbulence) is shown in Fig. 3.9. The coding gain of the rate 0.91 LDPC code over the rate 0.94 RS (255, 239) code is 6.7 dB. The gain over the uncoded system is again larger than 20 dB, although the whole range is not depicted in Fig. 3.9. The BER curve of the

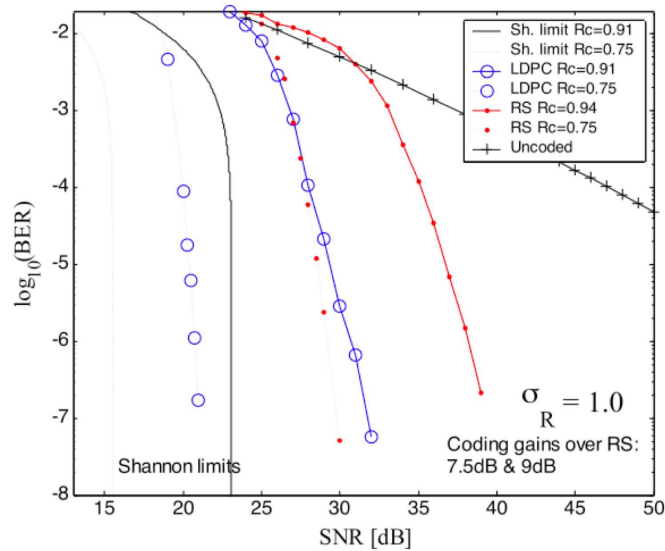


FIGURE 3.10. BER versus SNR for $\sigma_R = 1.0$.

LDPC code is about 7 dB away from the Shannon limit at $\text{BER} = 10^{-7}$.

Figure 3.10 shows the BER performance of both LDPC codes and both RS codes for a turbulence strength of $\sigma_R = 1.0$. This corresponds to a medium turbulent strength. The coding gains in this case are 7.5 dB and 9.0 dB over the RS codes, respectively. For this turbulence strength, the performance of the uncoded system is so poor that in practice a system cannot operate without coding, because an SNR of 50 dB is almost impossible to achieve.

Figures 3.11 and 3.12 show the BER performance in the strong turbulence regime for $\sigma_R = 2.0$ and $\sigma_R = 3.0$ respectively. LDPC coding gains with respect to the RS codes are even larger than in previous cases: 10.5 dB and 12 dB for the rate 0.91 code, at $\sigma_R = 2.0$ and $\sigma_R = 3.0$ respectively, and 12 dB and 14 dB respectively for the rate 0.75 codes. The performance of the LDPC codes departs more from the Shannon limit than for weaker turbulence, so there is more room for improvement

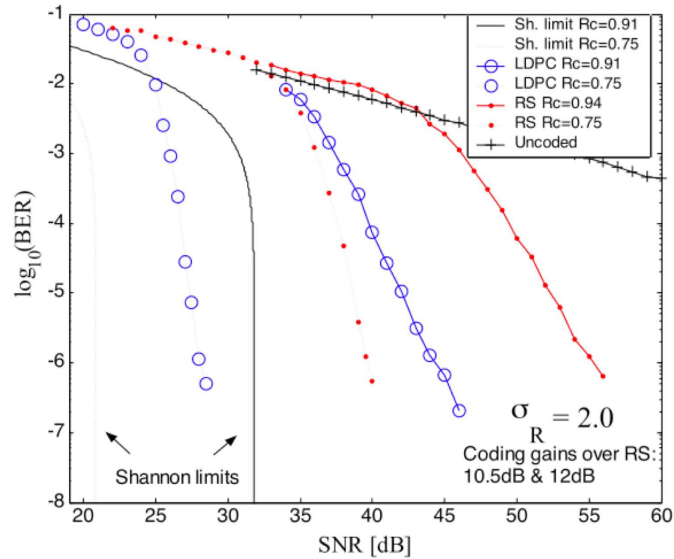


FIGURE 3.11. BER versus SNR for $\sigma_R = 2.0$.

here. The uncoded channel under this turbulence strength is almost useless. However, the values of capacity presented above show that although the BER performance of these uncoded channels is very poor, there is a significant room for improvement if appropriate channel codes are used, particularly at lower rates.

3.5. Conclusions

We analyze the atmospheric FSO channel from the perspective of information theory. This analysis is based on a gamma-gamma distribution model of the scintillation that has been shown to be a good representation of the actual effect of turbulence. We determine the channel capacity of the atmospheric FSO channel for a point receiver from weak through very strong turbulence conditions. For this analysis we consider both the zero and the non-zero inner scale instances.

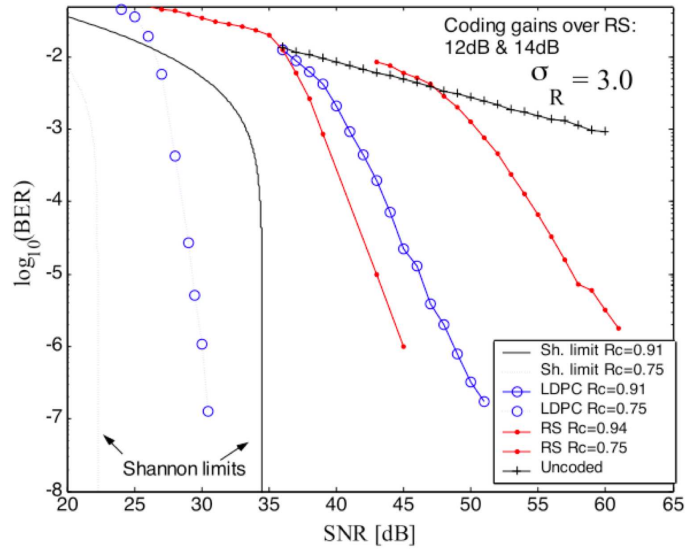


FIGURE 3.12. BER versus SNR for $\sigma_R = 3.0$.

We observe that the capacity reduces as the turbulence strength σ_R increases. This reduction is monotonic with σ_R at zero inner scale. We observe that for any given rate, the capacity decreases more rapidly at lower values of σ_R than at higher ones. At non-zero inner scale, we observe that for constant σ_R , the capacity decreases as l_0 increases. We also note that the capacity does not monotonically decrease with σ_R : it begins to grow over a certain value of σ_R , and this increment is more evident as l_0 increases.

We evaluate two error-correction systems based on LDPC codes with excellent correction capabilities for the FSO channel. We show that these codes provide very large SNR gains over Reed-Solomon codes of similar rate for a wide range of turbulence conditions. The delivered coding gains appear to grow as turbulence strengthens. These codes have been designed to provide low encoder and decoder complexity, making them very suitable for practical FSO communication systems.

4. SPATIAL CORRELATION AND IRRADIANCE FLUCTUATIONS IN MULTIPLE-BEAM LINKS

4.1. Introduction

An optical beam propagating in turbulent air experiences faster spreading than in vacuum, deflection from its geometric path, and wavefront distortions. All these phenomena are random in nature and induce a time-varying optical power at the receiver of the communication link. The variations in optical power seen by the receiver, usually referred to as scintillation, reduce FSO channel capacity or equivalently increase the bit-error rate (BER) [30]. In the effort to improve system performance, scintillation may be reduced by means of (1) aperture averaging, achieved by increasing the receiver aperture with the purpose of averaging the distortions on the optical wavefront [68, 69]; (2) spatial coherence reduction of the beam at the transmitter [24, 25]; and/or (3) exploiting spatial diversity with the use of multiple transmitted beams and/or multiple receivers [16, 23, 32, 33, 70–72].

Aperture averaging requires increasing both the receiver aperture and the detector's area. The need for the latter originates in the random phase distortions suffered by the beam, which reduce the spatial correlation of the optical wavefront [22]. This in turn increases the spatial frequency content and, therefore, broadens the point-spread function at the focal plane. As shown experimentally in [26], a relatively small aperture can provide a ten-fold averaging factor, but further improvement grows only logarithmically with aperture size. Moreover, smaller averaging factors are expected in high-bit-rate systems, for which optical detectors must have small area.

Beams with reduced spatial coherence show lower scintillation at the cost of faster divergence and, therefore, lower average received power. The spatial coherence of a beam can be reduced by placing a phase diffuser at the output of the transmitter. By appropriately choosing the strength of the diffuser, the improvement in scintillation reduction overcomes the penalty of power reduction and significant signal-to-noise ratio (SNR) gains can be obtained in the weak turbulence regime [25].

The large degree of spatial diversity found in turbulent optical channels can also be exploited to reduce scintillation, and ultimately reduce BER. In this regard, most of the reported research has been focused on receiver diversity [16, 23, 32, 33, 70]. This previous work has demonstrated that a collection of small receivers can offer performance similar to that of a single large receiver. The use of multiple transmitters has also been suggested [70–72] to be used in multiple-input/single-output (MISO) or multiple-input/multiple-output (MIMO) configurations, similar to those proposed for wireless radio-frequency (RF) links. However, reported works on the physical characteristics of the multiple-beam terrestrial FSO channel and the improvements we may expect are not abundant [31, 73–76].

In this Chapter we will study a FSO MISO system. Because correlation among the constituent beams in a MISO system plays a key role in determining overall system performance, our focus will be on quantifying this spatial correlation structure as a function of turbulence strength, beam separation, receiver aperture, and propagation distance. Note that there have been some important experimental activities reported that undertook a similar task; however, because these activities were hardware-based, only isolated points in design space could be evaluated [31, 73–75]. Here we have taken a complementary approach in which we have employed a widely accepted numerical wavefront propagation model in order to conduct design studies that probe a large

volume of the relevant design space. We have verified that our numerical results agree with these previous experimental studies while simultaneously providing important insights into underlying trends. For example, we find a simple scaling rule that enables the prediction of correlation values and scintillation reduction at long propagation distances from known values obtained at shorter link lengths. We also present for the first time, a simple way to characterize the probability density function (PDF) of the temporal power fluctuations in a MISO system in terms of the PDF of a single-beam system operating under similar turbulence conditions.

The work reported here also verifies several expected trends. For example, we verify that spatial correlation increases with (a) increased propagation distance, (b) increased receiver aperture, and (c) decreased beam spacing. We also find that correlation does not depend significantly on the turbulence strength parameter C_n^2 or on link wavelength. We also discover one additional benefit from using multiple beams: because of the square-law relationship between optical power and electrical power, the total received power is increased by $M^{1/2}$ if the electrical power applied to one source is divided into M sources. This is important for battery operated FSO communication systems.

The chapter is organized as follows. In Section 4.2 we describe the system model on which we base our analysis along with our numerical propagation model. In Section 4.3 the analysis of channel correlation is presented. In Section 4.4 we compare the scintillation-averaging effects of four beams with that of a single-beam system for several receiver aperture sizes and a fixed detector area. We also describe the relationship between single- and multiple-beam probability densities. In Section 4.5 we present a BER comparison between a four-beam and a single-beam system for two different turbulence conditions. Here we introduce a rate-one space-time code adapted

from wireless RF communications and compare it to a simple space repetition code. The last Section summarizes our results.

4.2. System model

4.2.1. Description of system components

Our numerical analysis is based on the four-source single-receiver FSO link shown in Fig. 4.1. The transmitter comprises four mutually incoherent monochromatic sources of wavelength $\lambda = 1.55 \mu\text{m}$. As shown in Fig. 4.1, each transmitter produces a Gaussian beam that is directed toward the center of the receiver aperture. All laser sources are assumed to be noise-free and with equal power, as the latter is the most effective configuration to reduce scintillation. The transmitter apertures are separated by distances d . The beams are collimated and expanded to a radius w_0 chosen appropriately for the link distance so that the received power is maximized at the weakest turbulence considered in this study. In practical systems, this criterion is often relaxed to ease the alignment of the beams to the receiver. The incoherence (or independence) of the sources is important because it ensures the incoherent superposition (sum of intensities) at the detector, regardless of any channel-induced phase change. This is a feature not found in multi-source RF systems.

The receiver comprises a circular collecting lens with focal length $f_{Rx} = 15 \text{ cm}$ and diameter D , and a square PIN detector. The detector size is chosen to support a system bandwidth of 2GHz, for which $50\mu\text{m}$ is the typical size in the class of infrared free-space detectors. Because the transmitted beams form an angle with respect to the receiver's optical axis, the focal spots will lie away from the center of the detector. This limits the ratio d/z between beam-separation d and link-distance

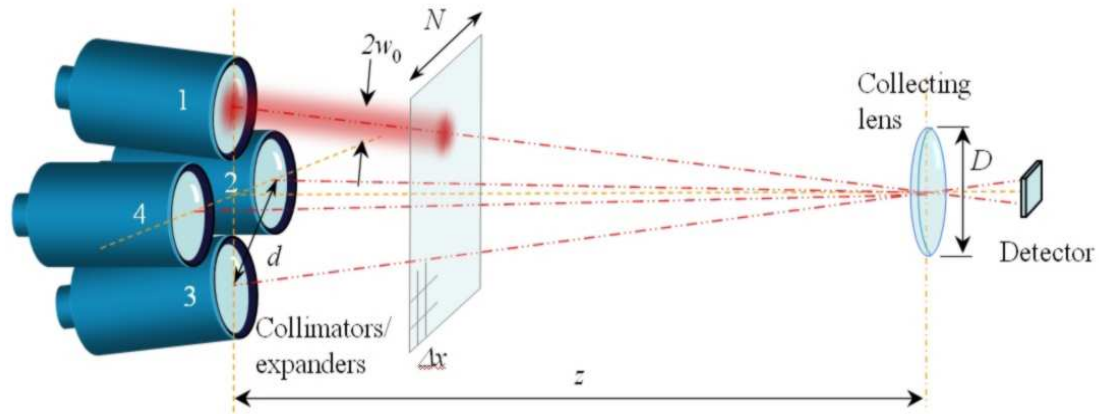


FIGURE 4.1. Diagram of a four-beam/single-receiver FSO link.

z , but is otherwise more energy-efficient than using parallel beams. For instance, a $50\mu\text{m}$ -detector is large enough to contain about 98% of the power focused by a 4cm-lens from all incident beams in the absence of turbulence, assuming a 1km-link with beam separation $d = 10$ cm. Any power not collected by the detector is considered lost, with the consequent reduction in SNR. Because the purpose of this work is to quantify channel correlation and scintillation reduction, background radiation is not considered in this analysis.

Using multiple receivers together with multiple sources is an alternative not evaluated in this study, but it is worthwhile mentioning that in such an architecture one must assess the additional detector noise incurred. Unlike wireless RF links in which any additional receiver will increase the SNR, optical links exhibit line-of-sight propagation with little radiation to adjacent channels. If a larger divergence angle is given to the beams (i.e., by adjusting the beam's radius of curvature), larger channel loss is also experienced. The use of multiple smaller receiver apertures (with one detector) in place of a single large aperture may however be a cost-effective solution that can

give good performance in moderate to strong turbulence conditions [23, 32].

4.2.2. Beam propagation and turbulence simulation

Gaussian beam wavefront propagation is performed using the split-step Fourier method [50]. In order to generate statistics with 95% significance or better, many thousands of simulation runs (one simulation run involves propagating the wavefront from the transmitter to the receiver) are needed for each set of simulation parameters. Note that this involves very long computing times, performed on many machines. We select a grid size of $N = 512$ points on a square window of 50 cm on a side perpendicular to the propagation axis z . This gives a pitch of $\Delta x = \Delta y = 0.98$ mm, well beyond the Nyquist sampling rate for the inner scale of turbulence $l_0 = 5$ mm that we use throughout our study. Turbulence is included via the use of random phase screens placed at steps $\Delta z = 40$ m. This screen separation is small enough to ensure small phase transitions, yet large enough to guarantee the validity of the assumption that turbulence is uncorrelated between contiguous screens. To generate the random phase screens we have used the modified version of the Kolmogorov refractive-index power spectrum proposed by Andrews [47], given earlier in (2.3). The spectrum is described by

$$\begin{aligned} \Phi(\kappa) = & 0.033 C_n^2 (\kappa^2 + 1/L_0^2)^{-11/6} \exp(-\kappa^2/\kappa_l^2) \\ & \times [1 + 1.802(\kappa/\kappa_l) - 0.254(\kappa/\kappa_l)^{7/6}], \end{aligned}$$

where κ is the spatial frequency, $\kappa_l = 3.3/l_0$, C_n^2 is the refractive-index structure parameter, L_0 is the outer scale of turbulence (which is set to $L = 10$ m) and l_0 is the inner scale. The propagation of beams from different optical sources is done one at a

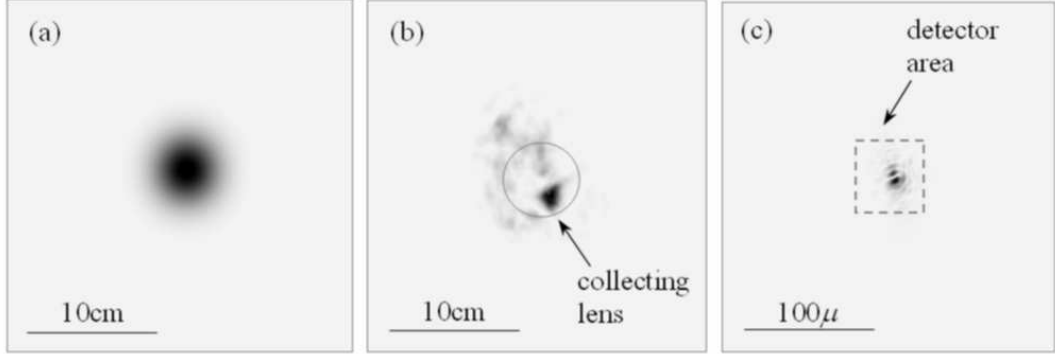


FIGURE 4.2. Example of a (a) collimated Gaussian beam with $w_0 = 4$ cm (b) after 1 km propagating in turbulent air with $C_n^2 = 10^{-13} \text{ m}^{-2/3}$ and (c) the (zoomed-in) point-spread function at the focal plane of the collecting lens whose area is marked in (b).

time on a common set of random screens to ensure incoherent superposition. At each propagation step the optical fields are attenuated on the edges of the screens using a two-dimensional super-Gaussian function to avoid energy leakage that otherwise would occur from Fourier transform operations. This ensures the integrity of the propagating field that reaches the detector.

We assume clear air and no mechanical flexure. Values for the refractive-index structure parameter are taken from the range $2 \times 10^{-15} \text{ m}^{-2/3} \leq C_n^2 \leq 10^{-12} \text{ m}^{-2/3}$, with a maximum propagation distance of 1km in the case of $C_n^2 = 10^{-12} \text{ m}^{-2/3}$. When longer propagation distances are considered, the maximum value of C_n^2 must be restricted to avoid significant energy spread outside the simulation volume. A detailed description of these numerical constraints is presented by Belmonte in [50].

4.2.3. Definition of channel coefficients

The propagated optical field is masked at the receiver by a circular aperture and the point-spread function observed at the detector plane is computed as the scaled

Fourier transform of the masked field, according to the Fresnel approximation [48]. The size and shape of the point-spread function depends on the amplitude and phase distortions induced by turbulence, as well as on the wavelength, the lens diameter, and the focal length. Fig. 4.2 shows an example of an intensity profile resulting from an (a) initially collimated Gaussian beam (b) after propagating 1 km with $C_n^2 = 10^{-13} \text{ m}^{-2/3}$ and (c) the corresponding point-spread function observed at the detector plane. We define the received optical power $p_{Rx}(i)$ from beam i as the spatial integral of the intensity $I_{r(i)}(u, v)$ falling on the detector's surface, where (u, v) are the coordinates of the simulation grid at the detector plane, and (u_0, v_0) and (u_1, v_1) are the coordinates of the beginning and end position of the detector surface. The transmitted optical power for beam i , $p_{Tx}(i)$, is defined as the integral of the transmitted intensity profile $I_{t(i)}(m, n)$ of beam i , where (m, n) are the coordinates of the simulation grid at $z = 0$. The instantaneous *channel coefficient* h_i is defined as the ratio between $p_{Rx}(i)$ and $p_{Tx}(i)$, for a given channel instance. That is,

$$h_i = \frac{p_{Rx}(i)}{p_{Tx}(i)} = \frac{\sum_{u=u_0}^{u_1} \sum_{v=v_0}^{v_1} I_{r(i)}(u, v)}{\sum_{u=u_0}^{u_1} \sum_{v=v_0}^{v_1} I_{t(i)}(u, v)}. \quad (4.1)$$

Thus, channel coefficients h_i range from 0 to 1.

4.3. Analysis of correlation

The effectiveness of the MISO scheme depends on the correlation among channel coefficients. Therefore, it is important to understand the dependence of correlation upon the system parameters and the turbulence conditions. The random nature of turbulence makes h_i random in both space and time. We define the spatial channel

correlation coefficient as

$$\hat{r}_{ij} = \frac{\langle h_i h_j \rangle - \langle h_i \rangle \langle h_j \rangle}{s_i s_j} \quad (4.2)$$

where $\langle \rangle$ represents ensemble average and s_i is the sample standard deviation of h_i . To have a value of \hat{r}_{ij} with a significance of at least 0.95 (by means of a t-test) we generate a minimum of 15,000 channel samples for each set of parameters, and up to 30,000 samples for those cases in which $\hat{r}_{ij} < 0.03$. In the first set of simulations we fix the propagation distance to $z = 1$ km. The structure parameter C_n^2 takes values in the set $\{2 \times 10^{-15}, 5 \times 10^{-14}, 2 \times 10^{-13}, 8 \times 10^{-13}\} \text{ m}^{-2/3}$ and the receiver aperture is varied from $D = 1$ cm to $D = 7$ cm, and $L_0 = 10$ m and $l_0 = 5$ mm. All beams are collimated at the transmitter and have a $1/e$ radius of $w_0 = 2.2$ cm. We present the resulting correlation data in several ways to make the dependence on the free parameters more apparent.

4.3.1. Correlation versus receiver aperture

The plots in Fig. 4.3 show the average channel correlation as a function of beam separation at the transmitter, d , for several values of turbulence strength C_n^2 . We have plotted the average correlation \hat{r} among all pairs of beams that are separated at distance d , specifically, $\hat{r} = (\hat{r}_{12} + \hat{r}_{23} + \hat{r}_{34} + \hat{r}_{14})/4$. In (a) the receiver aperture is $D = 1$ cm, in (b), $D = 3$ cm, in (c), $D = 5$ cm, and in (d), $D = 7$ cm. The error bars represent a ± 1 standard deviation of the estimation error. At any receiver aperture diameter, correlation decreases monotonically with beam separation, as one would expect. We observe that the dependence of correlation on C_n^2 saturates at $C_n^2 = 5 \times 10^{-14} \text{ m}^{-2/3}$. Above that turbulence strength correlation does not experience significant change for any fixed beam separation.

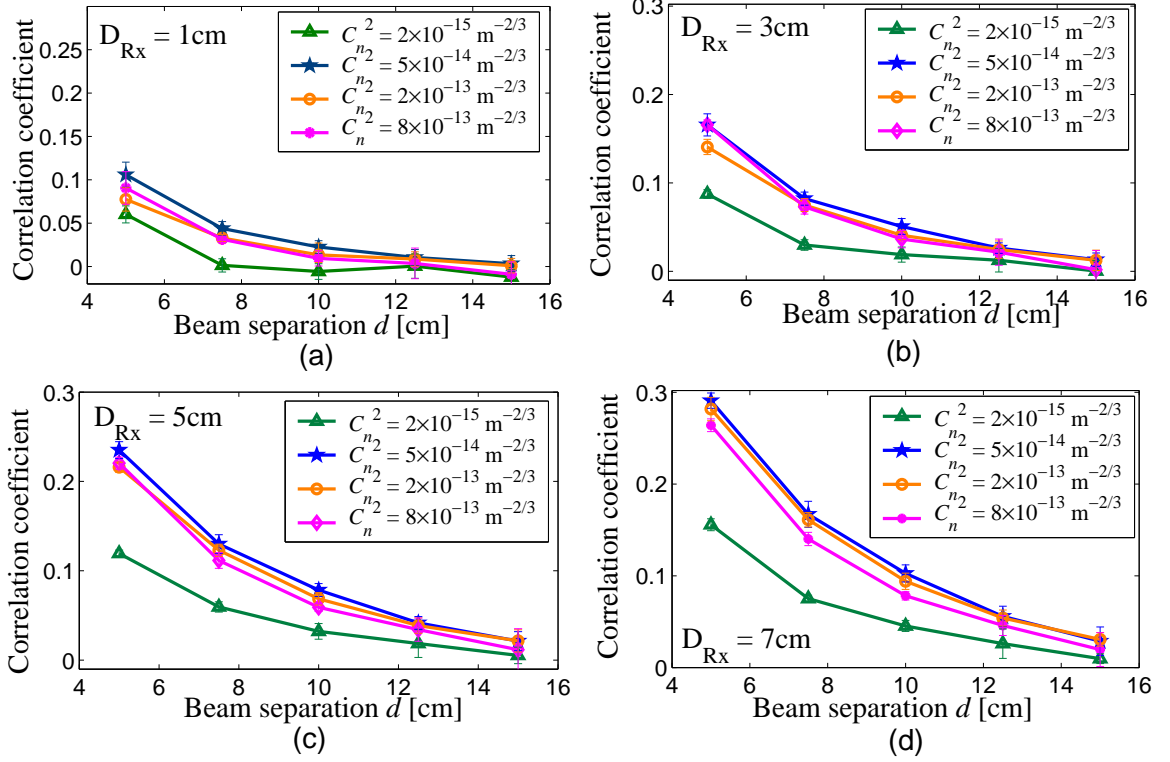


FIGURE 4.3. Average correlation coefficient between pairs of converging beams on a single receiver, with receiver aperture (a) $D = 1 \text{ cm}$, (b) $D = 3 \text{ cm}$, (c) $D = 5 \text{ cm}$, and (d) $D = 7 \text{ cm}$.

As the receiver aperture is increased, correlation increases accordingly. This may be explained by the fact that with larger aperture, a larger fraction of the beam's energy is collected, and part of that energy has propagated in a common path. In Fig. 4.4, correlation is plotted as a function of collecting lens diameter for (a) $C_n^2 = 2 \times 10^{-15} \text{ m}^{-2/3}$, (b) $C_n^2 = 5 \times 10^{-14} \text{ m}^{-2/3}$, (c) $C_n^2 = 2 \times 10^{-13} \text{ m}^{-2/3}$, and (d) $C_n^2 = 8 \times 10^{-13} \text{ m}^{-2/3}$. We observe that in all cases, channel correlation increases monotonically with collecting lens diameter, and this dependence is stronger at shorter beam separations. The increase in spatial correlation with increasing receiver aperture presents a trade-off. Effective scintillation control requires low correlation. This is also a requirement for obtaining good performance in multiple-beam systems using space-

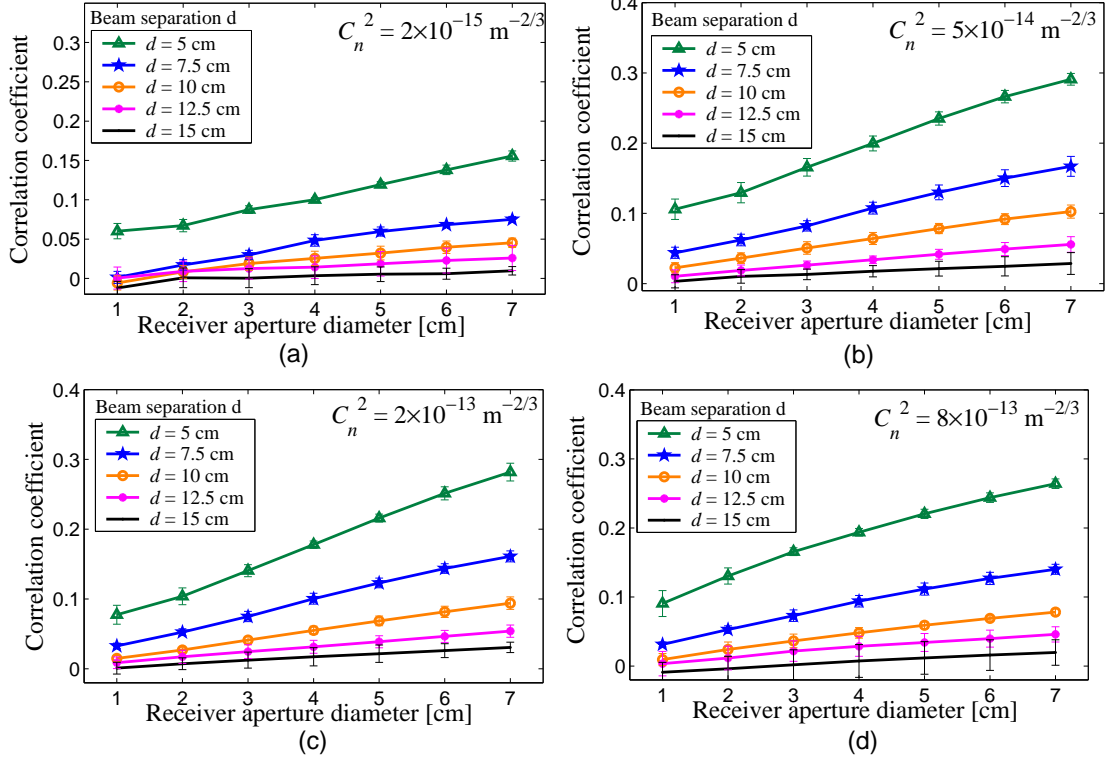


FIGURE 4.4. Average correlation coefficient versus receiver aperture diameter for (a) $C_n^2 = 2 \times 10^{-15} \text{ m}^{-2/3}$, (b) $C_n^2 = 5 \times 10^{-14} \text{ m}^{-2/3}$, (c) $C_n^2 = 2 \times 10^{-13} \text{ m}^{-2/3}$, and (d) $C_n^2 = 8 \times 10^{-13} \text{ m}^{-2/3}$.

time coding. This leads to a preference for smaller receiver aperture and, consequently, to lower SNR. The optimal combination depends on the application, which in some cases may prefer smaller power variations and smaller receiver size at the cost of lower average received power.

4.3.2. Correlation versus propagation distance

The results in Fig. 4.3 and Fig. 4.4 make an important point: channel correlation cannot be expected to directly scale with scintillation. This is because correlation may be thought of as an effect of multiple scattering, in which the probability of a

scattering event increases with propagation distance. At this point it is convenient to make use of the *Rytov variance* [defined in (3.1)] as a metric for turbulence strength. It is given by

$$\sigma_R^2 = 1.23 C_n^2 k^{7/6} z^{11/6},$$

where $k = 2\pi/\lambda$ is the propagation constant. At a propagation distance $z = 1$ km, $C_n^2 = 2 \times 10^{-15} \text{ m}^{-2/3}$ is equivalent to $\sigma_R^2 = 0.04$. Similarly, $C_n^2 = 5 \times 10^{-14} \text{ m}^{-2/3}$, $C_n^2 = 2 \times 10^{-13} \text{ m}^{-2/3}$, and $C_n^2 = 8 \times 10^{-13} \text{ m}^{-2/3}$ correspond to $\sigma_R^2 = 1.0$, $\sigma_R^2 = 4.0$, and $\sigma_R^2 = 16.0$, respectively. We evaluate and compare the correlation found for (i) $z = 1$ km and $C_n^2 = 8 \times 10^{-13} \text{ m}^{-2/3}$, (ii) $z = 2$ km and $C_n^2 = 2.25 \times 10^{-13} \text{ m}^{-2/3}$, (iii) $z = 4$ km and $C_n^2 = 6.3 \times 10^{-14} \text{ m}^{-2/3}$, and (iv) $z = 9$ km and $C_n^2 = 1.43 \times 10^{-14} \text{ m}^{-2/3}$. All four cases have a Rytov variance $\sigma_R^2 = 16.0$. We have varied w_0 and D according to the propagation lengths such that the average received power is the approximately same for all cases. The corresponding correlation curves are plotted as a function of beam separation in Fig. 4.5. A conspicuous increase in correlation with propagation distance is observed.

From these results, we can extract an order-of-magnitude estimate for the correlation at larger propagation distances. For a given Rytov variance the correlation found at beam separation d_0 and propagation distance z_0 equals the correlation found at beam separation

$$d = d_0 \sqrt{z/z_0} \tag{4.3}$$

and propagation distance z . This relation holds as long as the average ratio of received power and transmitted power is maintained (that is, the receiver aperture is increased for longer distances in order to maintain a constant power ratio). Furthermore, a

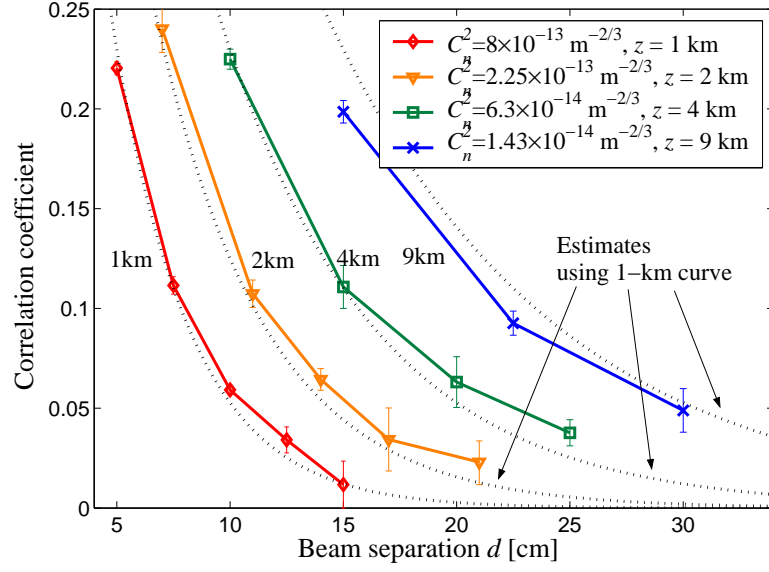


FIGURE 4.5. Average correlation coefficient among pairs of beams at 1 km, 2 km, 4 km, and 9 km with $\sigma_R^2 = 16$. Correlation estimates (dotted curves) for 2 km, 4 km, and 9 km are obtained by using the data from 1-km curve and equation (4.5).

decaying exponential of the form

$$r = \exp(-C d_0) \quad (4.4)$$

is fit to the simulation data corresponding to $C_n^2 = 8 \times 10^{-13} \text{ m}^{-2/3}$ and $z_0 = 1 \text{ km}$ (line with diamond markers in Fig. 4.5), where $C = 0.295$ is a constant that minimizes the mean-square error and d_0 is the beam separation in cm. By substituting (4.3) into (4.4) we can obtain an estimate of the spatial correlation at longer propagation distances, namely

$$r = \exp\left(\frac{-C d}{\sqrt{z/z_0}}\right). \quad (4.5)$$

We have plotted the correlation estimates for $z = 2 \text{ km}$, $z = 4 \text{ km}$, and $z = 9 \text{ km}$ using $C = 0.295$ and $z_0 = 1000$. These are shown by the dotted lines in Fig. 4.5. These estimates compare well with the simulated data. Note that if one considers

the saturation observed in correlation at $\sigma_R^2 > 1$ (Fig. 4.3), the recipe in (4.5) and the values in Fig. 4.5 may serve to estimate the spatial correlation coefficient at other propagation distances and wavelengths. Although not shown here, we have also quantified the spatial correlation experienced by beams with $\lambda = 850$ nm (in contrast with $\lambda = 1550$ nm) and $z = 9$ km for a few instances of d , showing agreement with the predicted curves in Fig. 4.5.

4.4. Scaling of scintillation using multiple beams

4.4.1. Scintillation reduction

We seek to reduce scintillation at the receiver by using multiple independent sources. Scintillation may be quantified by the received power variance

$$\sigma_I^2 = \frac{\langle (p_{Rx}(i) - \langle p_{Rx}(i) \rangle)^2 \rangle}{\langle p_{Rx}(i) \rangle^2} = \frac{\langle p_{Rx}^2(i) \rangle}{\langle p_{Rx}(i) \rangle^2} - 1, \quad (4.6)$$

where $p_{Rx}(i)$ is the received optical power from beam i , as defined in section 2.C. It is well-known that the sum of M independent and identically distributed (i.i.d.) random variables h_1, \dots, h_M with variance σ_h^2 has variance $\sigma^2 = M \sigma_h^2$. Therefore, the scintillation seen by a detector when M beams are used would be

$$\sigma_I^2 = \frac{\sigma_h^2}{M} \quad (4.7)$$

only if the assumption of independence holds. For practical reasons, multi-beam systems may be restricted in size, so assessing the effective scintillation reduction for small beam separations is important. In these cases, the independence assumption will not hold. Using the simulations described in the previous sections, we characterize

the total optical power resulting from the superposition of four incoherent beams as described in Section 2 and shown in Fig. 4.1. The scintillation of the four-beam system is compared with that of a single-beam system with the same receiver. The simulation of a one-beam system with a point receiver is also necessary to determine aperture averaging, as we explain below.

In Fig. 4.6(a) the scintillation of the configurations above are plotted for $D = 3$ cm and $D = 7$ cm together with the scintillation of the point-aperture case, as a function of σ_R . In order to quantify scintillation, we define two metrics: (i) *aperture averaging factor* A_D and (ii) *beam averaging factor* F_B as

$$A_D = \frac{\sigma_I^2(D)}{\sigma_I^2(0)}, \quad F_B = \frac{\sigma_{I_4}^2(D)}{\sigma_I^2(D)}, \quad (4.8)$$

where $\sigma_I^2(0)$ is the scintillation of the single-beam, point-receiver system; $\sigma_I^2(D)$ is the scintillation of the single-beam system with receiver aperture D and a $50\mu\text{m}$ square detector; and $\sigma_{I_4}^2(D)$ is the scintillation of the 4-beam system with the same receiver. The total averaging factor is then given by the product $A_D F_B$. The plot in Fig. 4.6(b) shows A_D and $A_D F_B$ as a function of receiver aperture for $C_n^2 = 2 \times 10^{-15} \text{ m}^{-2/3}$, $C_n^2 = 5 \times 10^{-14} \text{ m}^{-2/3}$, and $C_n^2 = 8 \times 10^{-13} \text{ m}^{-2/3}$. It is apparent in Fig. 4.6(a) that the overall reduction of scintillation is lower at large σ_R . The performance of A_D in Fig. 4.6(b) provides hints on the origin of this decreased effectiveness. It is due to the finite detector size, as the point-spread function is larger at stronger turbulence. In contrast, the beam factor F_B is rather insensitive to D and to the detector size if beam separation is relatively large (i.e., at low spatial correlation). Multiple beams can be used in exchange for collecting lens diameter to reduce scintillation and receiver size. For instance, in Fig. 4.6(b) the total averaging factor at $C_n^2 = 8 \times 10^{-13} \text{ m}^{-2/3}$ for

TABLE 4.1. F_B^{-1} at beam separation $d = \{5, 7.5, 10, 12.5\}$ cm.

C_n^2 [m ^{-2/3}]		2×10^{-15}	5×10^{-14}	2×10^{-13}	8×10^{-13}
$D = 1$ cm	$d = 5.0$	3.526	3.161	3.332	3.282
	$d = 7.5$	3.984	3.590	3.688	3.772
	$d = 10.0$	4.047	3.760	3.849	3.926
	$d = 12.5$	4.032	3.857	3.926	4.001
$D = 3$ cm	$d = 5.0$	3.292	2.800	2.928	2.820
	$d = 7.5$	3.726	3.291	3.350	3.405
	$d = 10.0$	3.805	3.513	3.603	3.677
	$d = 12.5$	3.896	3.688	3.757	3.827
$D = 5$ cm	$d = 5.0$	3.084	2.479	2.562	2.557
	$d = 7.5$	3.480	2.984	3.032	3.130
	$d = 10.0$	3.692	3.297	3.374	3.487
	$d = 12.5$	3.841	3.543	3.617	3.724

Simulation values: $z = 1$ km, $w_0 = 2$ cm, $l_0 = 5$ mm.

At $d = 15$ cm (not shown), F_B^{-1} ranges from 3.9 to 4.0.

$D = 1$ cm is about the same as that for a single beam with $D = 7$ cm.

All cases in Fig. 4.6 employ a beam separation $d = 15$ cm. For this and larger separations (in a 1-km link), the beams can be assumed to be spatially uncorrelated, as F_B^{-1} is close to 4. For smaller d the performance can still be good. Beam averaging factors for other values of d and C_n^2 are shown in Table 4.1. These beam averaging factors have been determined directly from the simulations according to (4.8), but they can also be predicted with good accuracy from the spatial correlation coefficients. The scintillation index of the combined system clearly depends on the correlation between the received signals of the constituent beams. This relationship can, in principle, be determined through the moment-generating function of the sum of the random variables characterizing the received power from each individual beam. However, this is a very burdensome mathematical problem. We circumvent this by assuming Normal statistics. In this case, it is simple to show that the scintillation

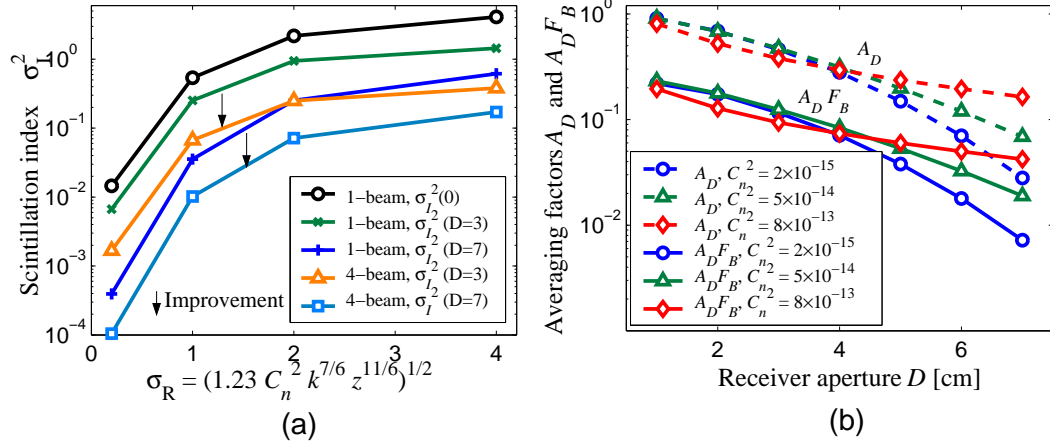


FIGURE 4.6. (a) Scintillation versus σ_R for five system configurations: (i) single-beam/point-receiver; (ii) single-beam, receiver aperture $D = \{3, 7\}$ cm and $50\mu\text{m}$ detector; (iii) four beams, receiver aperture $D = \{3, 7\}$ cm and $50\mu\text{m}$ detector. (b) Aperture averaging factor A_D and total averaging factor $A_D F_B$ versus receiver aperture D . For both (a) and (b), $z = 1$ km, $w_0 = 2.2$ cm, $L_0 = 10$ m, $l_0 = 5$ mm, $d = 15$ cm.

index $\sigma_{I_M}^2$ in a system with M spatially-correlated received signals can be expressed as

$$\sigma_{I_M}^2 = \frac{1}{M} \left(1 + \frac{2}{M} \sum_{p \in P} r_p \right) \sigma_I^2 \quad (4.9)$$

or, more conveniently

$$F_B^{-1} = M \left(1 + \frac{2}{M} \sum_{p \in P} r_p \right)^{-1}, \quad (4.10)$$

where r_p is the correlation coefficient between the p th pair of beams and P represent the set of all pairs of beams, and σ_I^2 is the single-beam scintillation. Clearly, in the uncorrelated case, (4.9) reduces to (4.7) as expected. The Normal statistics assumption is clearly not appropriate for characterizing the probability density functions of the received power, but it does give a good approximation to the overall scintillation as a function of the correlation coefficients. We have tested this hypothesis using

TABLE 4.2. Prediction of F_B^{-1} for the experiment in [73].

Predicted F_B^{-1} : 2.991 (Reported F_B^{-1} : 3.20)		
d [cm]	\hat{r}	No. of pairs
20.0	0.42213	8
35.0	0.22107	8
46.2	0.13639	8
50.0	0.11578	4

Parameters involved in the estimation of F_B^{-1} factor for the 46.8-km 8-beam experiment reported in [73]. The beam spacing d is given for all pairs of beams in the array.

the correlation data shown in Fig. 4.3 and were able to estimate the values of F_B^{-1} in Table 4.1 (assuming a square configuration of beams) with an accuracy of 4% or better at all values of C_n^2 . We use this hypothesis in the next subsection to predict the values obtained by some reported experimental setups.

4.4.2. Comparison with previously published experiments

In the 46.8-km multi-beam experimental demonstration reported in [73], 8 beams in a circular configuration are used in an effort to reduce scintillation. The separation between adjacent beams in that demonstration is 20 cm and the maximum beam separation (across diameter) is 50 cm. We estimate the correlation coefficient between all pairs of beams using (4.5) with a constant $C = 0.295$. The estimated coefficients were used in (4.10) to obtain $F_B^{-1} = 2.99$, very close to the reported value $F_B^{-1} = 3.20$ (data from June 29th in [73]). Table 4.2 summarizes all the values involved in computing F_B^{-1} .

The experiment in [75] reports the use of multiple beams in several configurations for propagation distances 1.2 km and 10.4 km. We focus on the latter case as

TABLE 4.3. Prediction of F_B^{-1} for the experiments in [75].

Predicted F_B^{-1} : (Reported F_B^{-1} : d [in]	4.296 4) \hat{r}	No. of pairs	Predicted F_B^{-1} : (Reported F_B^{-1} : d [in]	12.15 10) \hat{r}
4.0	0.39479	24	11.0	0.07763
5.7	0.26865	18	15.6	0.02693
8.0	0.15586	16	22.0	0.00603
8.9	0.12516	24	24.6	0.00330
11.3	0.06153	8	31.1	0.00073
12.0	0.06153	8	33.0	0.00047

Parameters involved in the estimation of F_B^{-1} factor for the 10.4-km 16-beam experiment for two of the square configurations reported in [75].

The beam spacing d is given for most of the pairs of beams possible in the 4-by-4-beam array.

the authors report large variations of the effectiveness in reducing scintillation with varying beam spacing. Considering the 4-by-4 square configuration of beams, with separation $d = 4$ inches between adjacent beams, we predict (using (4.5) and (4.10)) a beam averaging factor corresponding to $F_B^{-1} = 4.30$, significantly lower than 16, which is what one would obtain if the channels are uncorrelated. For beam spacing $d = 11$ inches, our estimation is $F_B^{-1} = 12.15$. These estimates match well (20% or better) the results plotted in [18, Fig.12b], approximately 4 and 10, respectively (however, values of scintillation or beam averaging factors are not explicitly given in the text). It is worth noting that the accuracy of the predictions is expected to be higher if the received power per beam is uniform. The pair-wise beam spacing and the corresponding correlation estimates are listed in Table 4.3.

A third comparison is made with the 5.4-km multibeam illumination experiment reported in [31]. The system comprises 9 beams, each with 4 cm in diameter, in a circular configuration with one in the center. According to the description, all the beams are contained within a circular area of diameter 20 cm. Using this information

we determined all the pair-wise beam spacings. In this case we use $C = 0.34$ in (4.5), fit to the lowest curve in Fig. 4.3(d). This is to account for the small Rytov variance ($\sigma_R = 0.25$), at which we cannot assume saturation of the spatial correlation coefficient, unlike in the previous comparisons. The predicted beam averaging factor (inverted) is $F_B^{-1} = 3.08$, almost the same as the observed value $F_B^{-1} = 3.0$. Table 4.4 summarizes the data used in this estimation.

4.4.3. Density function of multi-beam case

The Gamma-Gamma ($\Gamma\Gamma$) probability density function (PDF) serves as a good model for the power fluctuations seen at the receiver of a single-beam FSO communication system for a wide range of turbulence conditions [51, 77, 78]. It is given by

$$f(I) = \frac{2(\alpha\beta)^{(\alpha+\beta)/2}}{\Gamma(\alpha)\Gamma(\beta)} I^{(\alpha+\beta)/2-1} K_{\alpha-\beta} \left(2\sqrt{\alpha\beta I} \right), \quad I > 0 \quad (4.11)$$

where I is the received optical power, α and β are the parameters, Γ is the Gamma function, and $K_{\alpha-\beta}$ is the modified Bessel function of the second kind and order $\alpha-\beta$. We fit this PDF to the histograms obtained from simulation data corresponding to single-beam cases in order to determine the parameters α and β . We have found that the power variations for the multiple-beam case on a single receiver can also be modeled by a $\Gamma\Gamma$ PDF whose parameters are scaled versions of those from the single-beam case under the same turbulence conditions and design constraints. This scaling follows the beam averaging factor F_B very closely. That is, the PDF's parameters α and β of the multi-beam case can be expressed as

$$\alpha = F_B^{-1}\alpha_1, \quad \beta = F_B^{-1}\beta_1 \quad (4.12)$$

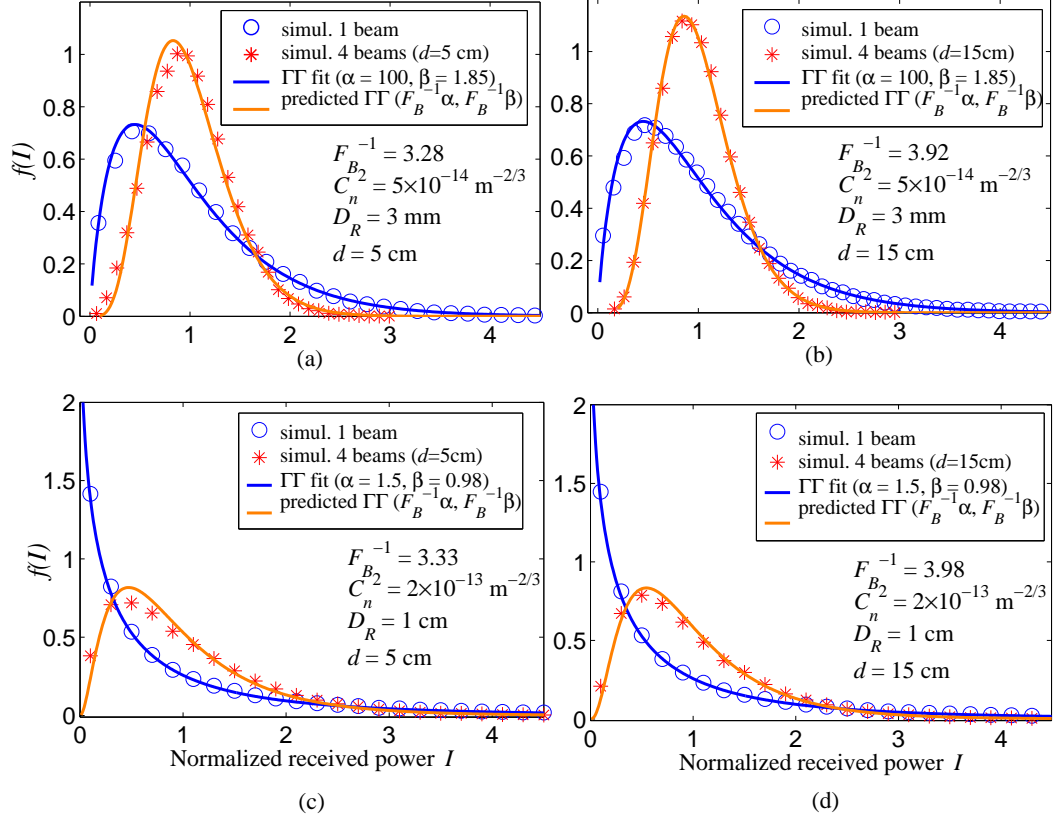


FIGURE 4.7. Histograms of intensity fluctuations and $\Gamma\Gamma$ fit. The $\Gamma\Gamma$ density curve for the 4-beam case is predicted using the beam factor F_B . (a) $C_n^2 = 5 \times 10^{-14} \text{ m}^{-2/3}$, $D = 3 \text{ mm}$, $d = 5 \text{ cm}$. (b) $C_n^2 = 5 \times 10^{-14} \text{ m}^{-2/3}$, $D = 3 \text{ mm}$, $d = 15 \text{ cm}$. (c) $C_n^2 = 2 \times 10^{-13} \text{ m}^{-2/3}$, $D = 1 \text{ cm}$, $d = 5 \text{ cm}$. (d) $C_n^2 = 2 \times 10^{-13} \text{ m}^{-2/3}$, $D = 1 \text{ cm}$, $d = 15 \text{ cm}$.

where the parameters α_1 and β_1 correspond to the single-beam case. The beam averaging factor's inverse F_B^{-1} reduces to the number of beams, M , when the channels are uncorrelated.

Figure 4.7 show four examples that compare the predicted PDF with the actual histogram. In Fig. 4.7(a), $C_n^2 = 5 \times 10^{-14} \text{ m}^{-2/3}$ and $D = 3 \text{ mm}$. The parameters for the single-beam case are $\alpha_1 = 100$ and $\beta_1 = 1.85$ and for a beam separation $d = 5 \text{ cm}$, $F_B^{-1} = 3.28$. The predicted PDF is a good match to the histogram obtained from the simulation data of the 4-beam case. We have quantified the goodness of fit by means

TABLE 4.4. Prediction of F_B^{-1} for the experiment in [31].

Predicted F_B^{-1} : 3.0779 (Reported F_B^{-1} : 3.0)		
d [cm]	\hat{r}	No. of pairs
6.11	0.4083	8
8.00	0.3102	8
11.3	0.1910	8
14.2	0.1247	8
16.0	0.0962	4

Parameters involved in the estimation of F_B^{-1} factor for the 5.4-km 9-beam experiment reported in [31]. The beam spacing d is given for all pairs of beams in the array.

of the correlation between the histogram and the predicted $\Gamma\Gamma$. For case (a) the correlation is $\rho = 0.9933$. In (b) the parameters are the same as in (a) but $d = 15$ cm. Here, $F_B^{-1} = 3.92$, and the predicted curve gives an excellent fit to the histogram. In this case, $\rho = 0.9994$. The examples in (c) and (d) employ $C_n^2 = 2 \times 10^{-13} \text{ m}^{-2/3}$ and $D = 1$ cm with beam separations $d = 5$ cm and $d = 15$ cm, respectively. In these cases we have $\alpha_1 = 1.5$ and $\beta_1 = 0.98$, with $F_B^{-1} = 3.33$ in (c) and $F_B^{-1} = 3.98$ in (d). The goodness of fit is $\rho = 0.9919$ for case (c) and $\rho = 0.9972$ for case (d).

A good fit is obtained using the $\Gamma\Gamma$ density function as long as the receiver aperture is small compared to the effective beam size at the receiver. We have observed that for relatively large collecting lenses, the histograms resemble a Gaussian density. A plausible reason is that larger apertures collect more independent fading patches and the PDF of the sum of these patches approaches a Gaussian distribution through the Central Limit theorem.

4.5. Bit-error rate comparison using space-time codes

The metrics analyzed above do not completely portray the communication system improvement to be expected by using a MISO scheme. The bit-error rate (BER) comparison presented here (based on Monte Carlo simulations) considers the effectiveness of the MISO approach in reducing the detection errors induced by both the random turbulent channel and the detector noise. We adapt the modulating and decoding strategy of a size-four rate-one space-time block code proposed for multi-input multi-output (MIMO) antenna systems in the context of wireless radio-frequency (RF) communications so that it can be used in intensity-modulated optical systems, following the approach proposed in [72]. We evaluate the bit-error rate performance of two space-time coding schemes using On-Off Keying (OOK) modulation. The first scheme uses a spatial repetition code and the second scheme uses a size-four rate-one ST block code mentioned above. We show that although both schemes have excellent performance in moderate and stronger turbulence conditions, the simpler repetition scheme is better. We later explain that this is due to the incoherent superposition of fields, naturally found in optical systems if independent sources are used.

4.5.1. Space repetition code

We can describe the output y of the FSO channel with the statistical expression

$$y = h x + \xi, \quad (4.13)$$

where h is the instantaneous channel coefficient, x is the transmitted symbol, and ξ is the zero-mean Gaussian noise added by the optical detector. The knowledge of h (usually referred to as channel state information in the context of coding theory

for fading channels) by the receiver is essential in the use of space-time codes. can be measured with small error using pilot signals. This is a realistic approach, as the temporal variations of scintillation are known to be slow compared to the bit rate of a typical FSO communication system [79].

A size-four space repetition code is defined by the column vector

$$\mathbf{x} = [x \quad x \quad x \quad x]^T \quad (4.14)$$

where x is the symbol to be transmitted and $[\cdot]^T$ is the transpose operation. The transmission vector in (4.14) implies that every symbol x is replicated and transmitted simultaneously by each optical transmitter. The time dimension of this code is just the transmission of the next symbol in the buffer. The received signal will be

$$y = (h_1 + h_2 + h_3 + h_4)x + \xi \quad (4.15)$$

where $\{h_i\}$ represent the single-beam channel coefficients defined in (4.1). In the context of RF communications, this code would not provide diversity because the channel coefficients add coherently. However, the superposition of independent optical sources is always incoherent, as the correlation length of a typical laser source will be much shorter than the path difference of any two transmitted beams [81]. The decoding statistic for the repetition code will then be

$$\hat{x} = y / \sum_{i=1}^4 h_i. \quad (4.16)$$

4.5.2. Space-time block code

A ST block code is defined by an $n_T \times p$ transmission matrix, where n_T is the number of optical transmitters, and p is the number of time steps required to transmit all symbols. In a binary system, q bits are encoded into n_T parallel binary sequences of length p , according to the transmission matrix \mathbf{X} . The rate of the code is given by $R = q/p$ [82]. We evaluate a modified rate-one ($q = 4, p = 4$), size-four, full-diversity code given by

$$\mathbf{X} = \begin{bmatrix} x_1 & -x_2 + A & -x_3 + A & -x_4 + A \\ x_2 & x_1 & x_4 & -x_3 + A \\ x_3 & -x_4 + A & x_1 & x_2 \\ x_4 & x_3 & -x_2 + A & x_1 \end{bmatrix} \quad (4.17)$$

where $\{x_1, x_2, x_3, x_4\}$ are the binary symbols to be transmitted, and A is the intensity of the OOK signal, which is added to negative symbols to produce non-negative transmit signals. In (4.17) we have followed the adaptation of the Alamouti (size-two) code proposed in [72]. The first column of the transmission matrix corresponds to the bits transmitted on each of the four optical transmitters during the first time interval. The following columns correspond to the second, third, and fourth group of transmitted bits, respectively. The received intensity at time interval t for the case of one receiver is given by

$$r_t = \sum_{i=1}^{n_T} h_i X_{i,t} + \xi_t, \quad (4.18)$$

where h_i is the intensity coefficient of channel i , $X_{i,t}$ is the (i, t) element of \mathbf{X} , and ξ_t is white Gaussian noise added by the detector at interval t . The channel coefficients $\{h_i\}$ are assumed to remain constant for the duration of the transmission of the entire matrix \mathbf{X} . The decoding scheme with linear processing proposed for RF systems [82]

must be modified to account for the constraints imposed on \mathbf{X} to work on non-negative signals. In our case, the decision statistic for symbol x_j with $1 \leq j \leq q$ is given by the expression

$$\tilde{x} = \sum_{i=1}^4 \delta_i(j) r_i h_{e_i(j)} + b_j \quad (4.19)$$

where $\delta_i(j)$ represents the *sign* of symbol x_j at column i of \mathbf{X} , $e_i(j)$ is the *position* of symbol x_j in column i , and b_j is the bias added to balance the decision statistic, given by

$$b_j = \begin{cases} 0, & j = 1 \\ -\sum_{i=2}^4 \delta_i(j) h_{e_i(j)} C_i, & j = 2, 3, 4. \end{cases} \quad (4.20)$$

where C_i are constants derived from the bias terms in r_i . In particular, $C_2 = A(h_1 + h_3)$, $C_3 = A(h_1 + h_4)$, and $C_4 = A(h_1 + h_2)$. The constructed statistics in (4.19) will have the form

$$\tilde{x} = (h_1^2 + h_2^2 + h_3^2 + h_4^2) x_j + \Xi_j \quad (4.21)$$

where Ξ_j is a noise term that comprises all noise contributions in (4.19). To decode the symbol j , we decide in favor of the symbol value $s \in \{0, 1\}$ that minimizes the expression [82]

$$m_j = |\tilde{x}_j - s|^2 + \left(\sum_{i=1}^4 |h_i|^2 - 1 \right) |s|^2, \quad (4.22)$$

which, with the assumption of a AWGN channel (as channel coefficients are known), is equivalent to thresholding the statistic

$$\hat{x}_j = \tilde{x}_j / \sum_{i=1}^4 h_i^2. \quad (4.23)$$

Note that the decision statistic in (4.23) differs from that of the repetition code

in (4.16) in that the former features a sum of the squares of the channel coefficients, rather than a sum of linear terms. This fact causes the two statistics to have different probability distributions. The ST codes described above do not have any error-correction capability; they just make use of the channel diversity of the multiple beam system. However, ST codes can be concatenated with any error-correction code.

4.5.3. Monte Carlo BER simulations

To evaluate the BER improvement achieved by using the space-time coding strategies described above, we modulate a randomly generated binary stream using On-Off keying(OOK). We assume that the channel state information is known to the receiver. For the purposes of this evaluation, the channel is assumed to remain constant for ten thousand consecutive bits and is varied randomly and independently from the previous instance. This scheme is usually referred to as block fading [80].

Channel coefficients are randomly generated according to a $\Gamma\Gamma$ PDF. We consider two specific cases for which (1) $C_n^2 = 10^{-13} \text{ m}^{-2/3}$ and $D = 3 \text{ cm}$, and (2) $C_n^2 = 10^{-12} \text{ m}^{-2/3}$ and $D = 5 \text{ cm}$. Both cases employ a beam separation $d = 15 \text{ cm}$. We define electrical signal-to-noise ratio (SNR) as the ratio between the average transmitted electrical power and receiver electrical noise power P_{Tx}/N_0 . Consequently, the BER curves include the power penalty incurred by the choice of beam diameter, receiver aperture, detector area, and beam spreading induced by turbulence. This penalty can be determined by an ensemble average of the channel coefficients h_i as defined in (4.1) and apply to both single-beam and four-beam systems. We have summarized these parameters in Table 4.5.

Figure 4.8 depicts the BER versus electrical SNR in dB for case (1). The curve

TABLE 4.5. Parameters used in the Monte Carlo simulations to determine BER.

Case	C_n^2 [$\text{m}^{-2/3}$]	Rx aperture D [cm]	Single-beam Γ (α, β)	$\sigma_I^2(D)$	Power penalty (channel loss)
(1)	10^{-13}	3	(4.6, 4.2)	0.694	7.7 [dB]
(2)	10^{-12}	5	(3.7, 3.0)	0.507	13.0 [dB]

with asterisk markers correspond to the repetition-code scheme; the curve with circle markers correspond to the ST block code; and the curve without markers is the BER of the uncoded single-beam system. The SNR gain is 23 dB between the repetition-coded system and the single-beam system at $\text{BER} = 10^{-6}$, and is 18 dB between the ST-block-coded system and the single-beam system at the same BER level. In each situation, the average transmitted electrical power per bit for the four-beam system is the same as that of the single-beam system. As mentioned in the introduction, splitting the electrical power into M independent sources provides an increase in optical power by a factor of \sqrt{M} . This derives from the square-law relationship between electrical power and optical power. If we assume a total electrical power normalized to unity, the optical power in each beam is proportional to $M^{-1/2}$. The total optical power is then $M \times M^{-1/2} = \sqrt{M}$. In our example, the total optical power is increased by a factor of 2, which translates into a gain of 6 dB in electrical SNR. This improvement is already included in the SNR gains given above. Figure 4.9 shows the BER performance for case (2). For this case, the SNR gains are 30 dB with the repetition code and 25 with the ST block code.

Our explanation for the better performance of the repetition code is that it achieves diversity without the need of separate transmissions. The ST block code was designed to work on RF channels where the superposition of fields is coherent. As a result, the statistics given in (4.16) and in (4.23) have different underlying prob-

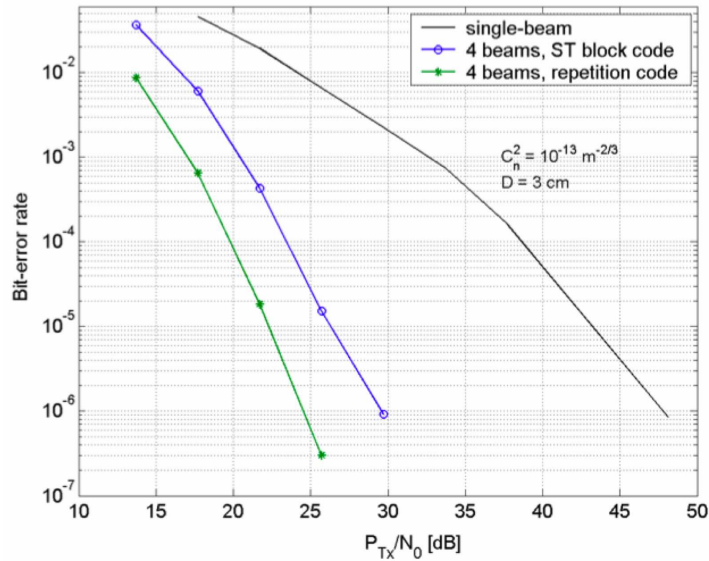


FIGURE 4.8. BER versus P_{Tx}/N_0 for a repetition code and a ST block code using four optical transmitters for the system parameters given in Table 4.5, case 1.

ability distributions. We have found that the decoding statistic of the repetition code is characterized by a less skewed probability density than that of the ST block code, which leads to a better performance of the former.

The channel conditions for cases (1) and (2) evaluated above correspond to Rytov variances $\sigma_R^2 = 2.0$ and $\sigma_R^2 = 19.9$, respectively. Both cases belongs to the strong turbulence regime, which is characterized by $\sigma_R^2 > 1$. In weaker turbulence conditions, the SNR gain may not be large enough to justify the cost of additional hardware, and aperture averaging alone (i.e., increasing the collecting aperture at the receiver) may be more cost-effective.

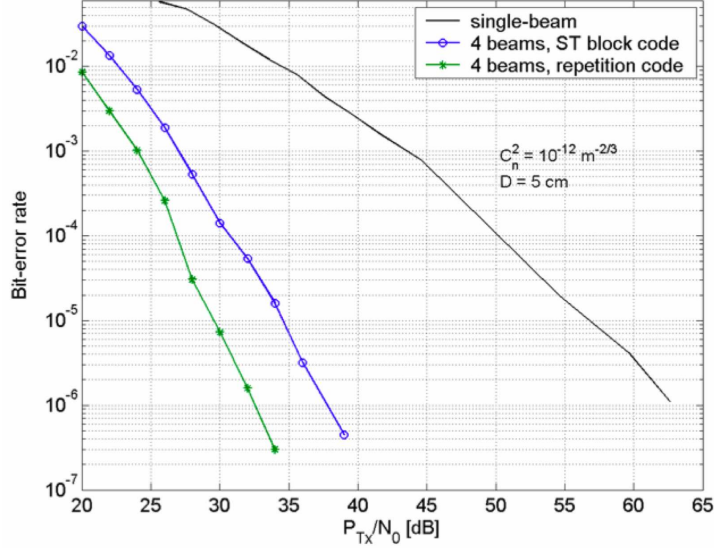


FIGURE 4.9. BER versus P_{Tx}/N_0 for a repetition code and a ST block code using four optical transmitters for the system parameters given in Table 4.5, case 2.

4.6. Conclusions

By means of numerical modeling we have analyzed the correlation among multiple incoherent beams projected onto a single receiver in an FSO communication system. Correlation is found to increase with the turbulence parameter C_n^2 up to a certain point (around $\sigma_R^2 = 1$) above which correlation saturates. Spatial correlation grows with increasing propagation distance and increasing collecting lens diameter. For $z = 1$ km, channel correlation is statistically significant for beam separations $d < 15$ cm.

It is observed that for constant Rytov variance, correlation increases with propagation distance, such that the correlation found at beam separation d_0 and propagation distance z_0 approximates the correlation found at beam separation $d = d_0 \sqrt{z/z_0}$ and propagation distance z . We provide simple expressions that, together with the corre-

lation curves given in Figures 4.3 and 4.5, can be used to predict correlation values at other propagation distances. We tested these predicting tools by comparing against previously reported experiments, with very good accuracy.

We find that the $\Gamma\Gamma$ PDF can be used to model the power fluctuations observed in a FSO MISO system. The parameters (α, β) corresponding to the density function of the MISO system are well approximated by $(F_B^{-1}\alpha, F_B^{-1}\beta)$. In this expression, F_B^{-1} is the inverse of the beam averaging factor, as defined in (4.8), and (α, β) are the parameters of a $\Gamma\Gamma$ PDF modeling the optical power fluctuations of a single-beam system under the same turbulence conditions.

The improvement in BER performance achieved by using multiple beams is evaluated. Large SNR gains are obtained by using such configurations compared to single-beam systems using the same electrical power. The averaging effects on scintillation achieved by the MISO scheme multiply those obtained from aperture averaging at the receiver. This combined effect significantly reduces the power requirements to operate at low BER, and may provide a cost-effective alternative to large collecting apertures.

5. ORBITAL ANGULAR MOMENTUM-BASED CHANNEL MULTIPLEXING

5.1. Introduction

Orbital angular momentum (OAM) is a property of light associated with the helicity of a photon's wavefront. Optical beams carrying OAM are usually called optical vortices, because they feature a phase discontinuity at their center. This discontinuity produces a dark central spot in the intensity distribution of such an OAM beam. A vector normal to a vortex wavefront follows a spiral trajectory around the optical propagation axis. The momentum of a vortex field is proportional to the number of turns that this vector completes around the beam's axis after propagating a distance equal to one wavelength. This number is equal to the OAM state.

Unlike spin angular momentum, for which only two states are possible, the OAM state of a photon can take any integer value. This infinite set of OAM states forms an orthonormal basis [83–85]. This property may be exploited in the context of optical communications [85–87]. The orthogonality among beams with different OAM states allows the simultaneous transmission of information from different users, each on a separate OAM channel. Each orthogonal channel can be perfectly filtered and decoded at the receiver of a free-space optical (FSO) communication link. OAM states may also be used for multilevel modulation [85].

Although OAM could in principle be imprinted on any optical wavefront, some optical beams have well-defined vorticity. Among the beams that can carry OAM we find Bessel beams, Hermite-Bessel beams, helical Mathieu beams, and Laguerre-Gauss beams [83, 84, 88–91]. The phase front of an optical beam carrying OAM is of

course diffracted as it propagates in any linear, isotropic, and homogeneous medium; however, the vorticity of the beam is preserved so that wavefronts with different OAM states remain orthogonal after propagation. For FSO applications however, it is important to note that orthogonality is no longer maintained in the presence of atmospheric turbulence [92]. Atmospheric turbulence is a random process in which heat is continuously transferred within the air. As described by Kolmogorov's model, air cells of various sizes and different temperature break continuously into smaller cells in a process that ends as cells dissipate by viscosity. This process makes the optical channel inhomogeneous because the transmitted optical wavefront propagates along a space- and time-varying refractive index distribution. As a result, part of the energy launched into a single OAM state will be redistributed into other OAM states after turbulent propagation. Consequently, atmospheric turbulence induces a time-varying crosstalk among OAM channels.

There have been some successful laboratory experiments to generate beams with superimposed OAM states [84,85,93]. Our interest is to study the feasibility of a multi-channel OAM terrestrial FSO link and quantify the channel crosstalk as a function of turbulence strength, number of simultaneous channels, and signal-to-noise ratio (SNR). Through numerical methods we simulate the coaxial propagation of Laguerre-Gauss beams each with a distinct OAM state in the range $[-s_{max}, +s_{max}]$ over a 1-km turbulent path. Because we seek to determine the effects of atmospheric turbulence alone, we assume perfect generation and detection of the OAM channels.

As expected, these simulations verify that optical turbulence induces OAM crosstalk and that the average crosstalk between channels grows with turbulence strength. For each transmitted OAM state we (i) quantify the efficiency (% of power remaining in transmitted channel) of each channel in terms of the turbulence strength

and (ii) quantify the average crosstalk observed on all channels in the studied range, in terms of turbulence strength. The efficiency in (i) accounts for channel losses due to beam spreading, beam wander, and crosstalk.

The averages found above can be understood as the channel matrix of the OAM-multiplexed communication system. Knowledge of this matrix (at each turbulence strength level) is essential to designing and predicting the performance of such a system.

With the assumption that crosstalk and detector noise are mutually independent Gaussian noise sources we model each OAM mode as a binary symmetric channel whose probability of flip error is a function of the channel efficiency, the crosstalk induced by the other constituent channels, and by detector noise. Using this model we find for a prescribed number of channels the optimal set of OAM mode numbers, in the sense of maximizing the aggregate capacity. Because of the Gaussian assumption, this approach renders a lower bound on system capacity. The optimal sets of OAM state numbers are determined at each value of SNR and turbulence strength considered. Aggregate capacity curves and bit-error rate curves are presented as functions of transmit power to quantify the turbulence-induced channel losses and the service quality of constituent channels.

The Chapter is structured as follows. In section 5.2 we briefly describe the Laguerre-Gauss beams and note several methods for generating them. Section 5.3 describes the transmitter and receiver models and our numerical method for simulating the turbulent propagation. In section 5.4 the crosstalk among OAM channels is presented as a function of turbulence strength. The results on aggregate capacity and bit-error rate are given in section 5.5, and conclusions are given in section 5.6.

5.2. Orbital angular momentum in Laguerre-Gauss beams

5.2.1. Laguerre-Gauss modal distribution

Among the optical beams that can carry OAM, Laguerre-Gauss (LG) beams are of special interest because they are easily realizable. Because of its symmetry around the optical axis, the field distribution of a LG beam is best described in cylindrical coordinates. For a radial distance r from the propagation axis, azimuthal angle ϕ , and propagation distance z , the field distribution can be expressed as

$$\begin{aligned}
 u(r, \phi, z) = & \sqrt{\frac{2p!}{\pi(p+|m|)!}} \frac{1}{w(z)} \left[\frac{r\sqrt{2}}{w(z)} \right]^{|m|} L_p^m \left[\frac{2r^2}{w^2(z)} \right] \\
 & \times \exp \left[\frac{-r^2}{w^2(z)} \right] \exp \left[\frac{-ikr^2z}{2(z^2 + z_R^2)} \right] \\
 & \times \exp \left[i(2p + m + 1) \tan^{-1} \frac{z}{z_R} \right] \exp(-im\phi), \quad (5.1)
 \end{aligned}$$

where $w(z) = w_0\sqrt{1 + (z/z_R)^2}$ is the beam radius at distance z , w_0 is the radius of the zero-order Gaussian beam at the waist, $z_R = \pi w_0^2/\lambda$ is the Rayleigh range, λ is the optical wavelength, and $k = 2\pi/\lambda$ is the propagation constant. Note that in (5.1) the beam waist is at $z = 0$. The term $L_p^m(\cdot)$ represents the generalized Laguerre polynomial, and p and m are the radial and angular mode numbers, respectively.

There are several things to note in (5.1). The radial mode number p is such that $p+1$ represents the number of maxima in the radial intensity distribution. The angular mode number m corresponds to the OAM state number. For $p = 0$, $L_p^m = 1 \forall m$. By setting $m = 0$, $u(r, \phi, z)$ reduces to a zero-order Gaussian beam (TEM₀₀ mode). For $p = 0$ and $m \neq 0$, the intensity of a LG mode is a ring whose radius is proportional to \sqrt{m} . As an example, the intensity and phase profiles of a LG beam with $p = 0$ and

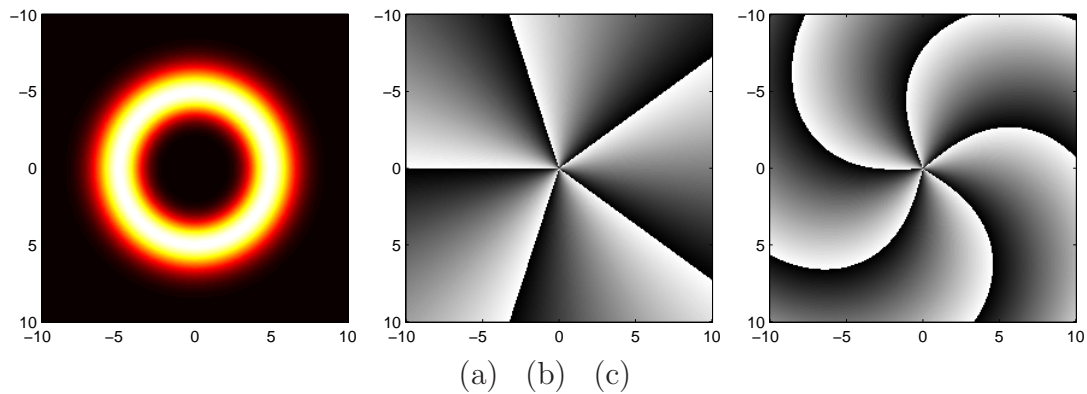


FIGURE 5.1. (a) Intensity distribution of a LG beam with OAM state $m = 5$ and radius $w_0 = 3$ cm. The frame is 20 cm on a side. (b) Phase distribution of the beam at $z = 0$. (c) Phase distribution of the beam at $z = 1$ km.

OAM state $m = 5$ and radius $w_0 = 3$ cm are shown in Fig. 5.1. The characteristic ring-shaped intensity distribution is depicted in (a). The phase distribution of the LG beam at $z = 0$ is shown in (b). The phase is represented by levels of gray, such that black corresponds to $-\pi$ and white to π . As explained in Section 1, a vector normal to the OAM wavefront rotates around the propagation axis m times as the beam propagates for one wavelength. Thus, at any given propagation distance, the beam is characterized by a helicoidal waveform whose phase linearly increases in the azimuth direction such that the total phase difference is $2\pi m$ radians. This explains the 5 line discontinuities in Fig. 5.1(b). Because diffraction induces a radially-dependent phase change with propagation, at $z = 1$ km the phase distribution looks like that of Fig. 5.1(c).

5.2.2. Generation methods

There are numerous methods for generating LG beams. Three methods that have received recent attention are (i) *mode conversion* from high-order Hermite-Gauss beams (generated by a laser) to LG beams by means of a pair of cylindrical lenses [94, 95]; (ii) a *spiral phase plate*, consisting of a transparent optical element whose thickness varies linearly with the azimuthal angle, such that a zero-order Gaussian beam propagating through it acquires a prescribed OAM state [96–101]; and (iii) *computer-generated holograms* created by recording a digitally-generated interference pattern between a reference beam and a LG beam onto a film or by controlling a SLM [85, 93, 102, 103]. Method (i) is theoretically the most efficient, but it is cumbersome as it requires starting with Hermite-Gaussian beams with high modal purity. Method (ii) may also have high efficiency (i.e., above 90%) depending on the number of (discrete) steps used to define the plate thickness. It is, however, not very flexible, as the plate is designed for one wavelength and one OAM state. Method (iii) allows great flexibility. Efficiencies vary according to the type of hologram used. Multi-channel FSO communication systems demand high efficiencies for all OAM states and volume holograms can fulfill such a requirement.

5.3. OAM-multiplexed system and propagation in turbulence

5.3.1. Transmitter and receiver models

The transmitter for the OAM-multiplexed communication system considered here comprises the following. As shown in the diagram of Fig. 2, a number of data-carrying TEM_{00} modes –each independently modulated by a data stream– are shone

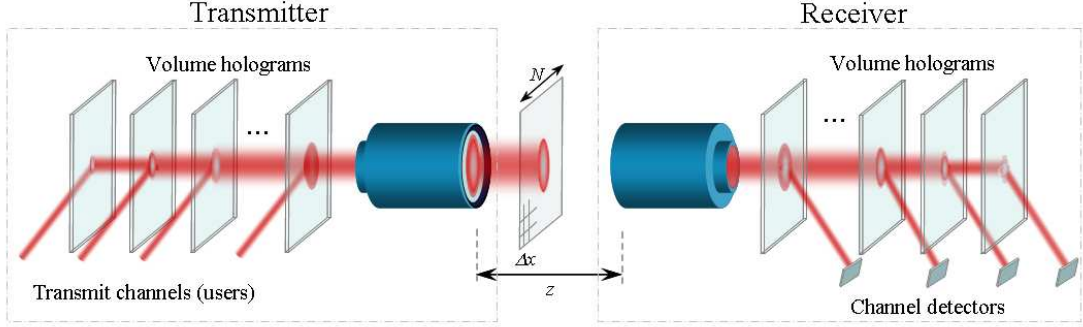


FIGURE 5.2. Diagram of a free-space optical communication link using multiplexed OAM channels.

onto a series of volume holograms, each programmed with a different OAM state, whose diffraction angles are designed to produce coaxial propagation of the outgoing OAM-carrying beams. After the set of independently modulated OAM beams have been made collinear (i.e., optically multiplexed), the resulting superposition field is expanded by a telescope, as shown in Fig. 2. For the work reported here we collimate and expand the outgoing multi-mode beam so as to minimize the receive aperture size for a given link length [27]. The receive aperture in turn, is matched to the size of the largest constituent OAM field so that 99.9% of the transmitted power will be collected in the absence of turbulence. This is accomplished by using a receive aperture diameter $D_{Rx} = 2 w_z \sqrt{|m_0|}$, where m_0 is the largest OAM state number in the system and w_z is the zero-order beam radius at propagation distance z . Even though a beam suffers further spreading in turbulent propagation, larger receiver apertures will not yield higher efficiencies (except for TEM_{00} modes) because the actual per-channel received power depends on the de-multiplexing holographic filter, whose programmed field is fixed.

The design of the receiver end of the link is based on the principle of the or-

thogonality among LG beams with different azimuthal mode numbers. Although the superposition and simultaneous propagation of a set of LG beams with different vorticity may produce an unrecognizable intensity pattern, the scalar product of any two of the constituent fields (after propagating through vacuum) is zero. This is related to the modal radiance theorem, which states that co-propagating modes can be perfectly split and recombined [104]. The receiver is, thus, based on a set of volume holograms programmed with the fields of each of the constituent received OAM channels. These holograms can be arranged in parallel and perform as filters that diffract the powers of the matching channels but otherwise allow transmission of non-matching channels. Given the received field $u_m(r, \phi, z)$ with OAM state m and the analyzing field $u_n^*(r, \phi, z)$ (where $*$ indicates complex conjugate) with OAM state n , the n th channel output signal (observed at the detector of channel n) is

$$\begin{aligned}
 u_m(r, \phi, z) \cdot u_n^*(r, \phi, z) &\triangleq \int r dr d\phi u_m(r, \phi, z) u_n^*(r, \phi, z) \\
 &= \begin{cases} 0 & \forall n \neq m \\ \int r dr d\phi |u_m(r, \phi, z)|^2 & n = m . \end{cases} \quad (5.2)
 \end{aligned}$$

The output signal in (5.2) can be recovered with a conventional PIN or APD detector. It is clear that for the case $n = m$ the outcome is equal to the total power of the observed field. With this approach one can use on-off keying (OOK), pulse-position modulation (PPM), or any other modulation scheme appropriate for direct-detection FSO [105].

We note that given the phase evolution induced by diffraction, the channel filters are designed using the diffracted versions of the LG modes. That is, each detecting hologram must be recorded with the field $u(r, \phi, z = z_L)$, where z_L is the link distance;

otherwise, the power is not maximized. The receiver comprises a collecting lens whose diameter is as large as the largest LG beam considered. In our study, the optical detector is assumed to be large enough to neglect power losses at the focal plane so that only the effects of turbulence on OAM channels are analyzed. Because the FSO channel is not frequency-selective within the range of current bit-rates, the results obtained here will be valid for any data rate. This principle, however, does not hold at very high bit rates for which optical detectors must be small, and therefore, focal plane loss must be included.

We consider a link distance $z = 1$ km. The optical beams have a zero-order radius $w_0 = 1.6$ cm at the transmitter. This radius minimizes the spot size at the receiver end for the link distance considered. All OAM channels use a wavelength $\lambda = 850$ nm. Note that LG beams with larger m are characterized by wider intensity distributions, resulting in a larger optical aperture requirement. This scaling will set a practical limit on the number of OAM channels a system (with a single optical receiver aperture) can have. The diameter of the receiver optics will depend on the turbulence level. For instance, a 15-centimeter collecting aperture is enough to accommodate 21 OAM modes (i.e., from -10 to +10) for the given beam parameters and propagation distance. This diameter is large enough to collect 99.99% of the largest mode's power in the absence of turbulence.

5.3.2. Propagation in turbulence

We simulate the propagation of LG beams with states $m \in \mathcal{S} = \{-s_{max}, -s_{max} + 1, \dots, -1, 0, +1, \dots, +s_{max} - 1, +s_{max}\}$ in atmospheric turbulence (where s_{max} is chosen depending on the strength of the turbulence) by means of the split-step Fourier method [27,50,106]. Turbulence is induced by means of random phase screens inserted

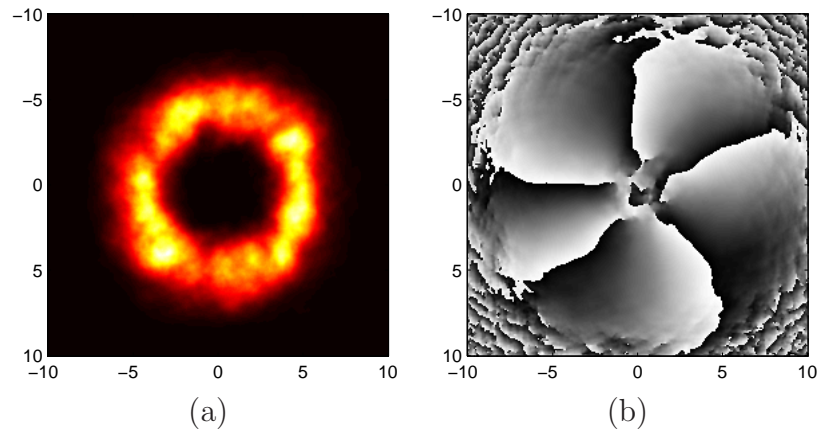


FIGURE 5.3. (a) Intensity distribution of a distorted LG beam with initial OAM state $m = 5$ and radius $w_0 = 3$ cm. The frame is 20 cm on a side. (b) The distorted phase distribution after $z = 1$ km still preserves some of its helical structure. In this example $C_n^2 = 10^{-15} \text{ m}^{-2/3}$.

every 50 m along the propagation path. Each screen is generated by shaping (in the Fourier domain) a set of complex Gaussian deviates according to a two-dimensional power spectrum of refractive-index fluctuations. Again we consider the power spectrum proposed by Andrews [47] given earlier in (2.3) and later repeated in Section 4.2. The outer and inner scales are set to $L_0 = 20$ m and $l_0 = 5$ mm, respectively. The numerical grid comprises 512×512 elements and covers an area of $70 \times 70 \text{ cm}^2$ transverse to the propagation axis. Turbulence strength is controlled by varying C_n^2 from $10^{-16} \text{ m}^{-2/3}$ to $10^{-13} \text{ m}^{-2/3}$. Figure 5.3 shows the intensity and phase distributions of an LG beam whose characteristics are the same as those from Fig. 5.1, after propagation for 1 km in turbulence with $C_n^2 = 10^{-15} \text{ m}^{-2/3}$.

The outer and inner scales are set to $L_0 = 20$ m and $l_0 = 5$ mm, respectively. The numerical grid comprises 512×512 elements and covers an area of $70 \times 70 \text{ cm}^2$ transverse to the propagation axis. Turbulence strength is controlled by varying C_n^2 from $10^{-16} \text{ m}^{-2/3}$ to $10^{-13} \text{ m}^{-2/3}$. Figure 5.3 shows the intensity and phase distribu-

tions of an LG beam whose characteristics are the same as those from Fig. 5.1, after propagation for 1 km in turbulence with $C_n^2 = 10^{-15} \text{ m}^{-2/3}$.

5.4. OAM crosstalk induced by turbulence

5.4.1. The channel matrix

To determine the channel crosstalk we undertake the following procedure. For a given value of C_n^2 , a LG beam with OAM state m is propagated in turbulence as described above. The received, distorted OAM-carrying field is filtered according to the scalar product operation defined in (5.2) for every $m, n \in \mathcal{S}$ and the resulting projections are recorded. This corresponds to one instance of the channel. We repeat this operation on 20,000 different channel instances. Projections are averaged for each (m, n) , yielding a $(2 s_{max} + 1) \times (2 s_{max} + 1)$ matrix whose elements are normalized by the transmitted energy. We denote this matrix by \mathbf{H} . In the absence of turbulence \mathbf{H} is an identity matrix. It is worth noting that the elements of \mathbf{H} relate to optical power, not electrical power. Energy loss induced by fast beam spreading and beam wander are accounted for in \mathbf{H} . Because we consider a transparent medium, this lost energy is in fact spread to outer OAM states.

We perform the numerical propagation described above for several values of C_n^2 , namely, 10^{-16} , 10^{-15} , 10^{-14} , 3×10^{-14} , and $10^{-13} \text{ m}^{-2/3}$. We have determined \mathbf{H} for each of these C_n^2 values. As we have done in previous chapters, we can also express the propagation conditions in terms of the *Rytov variance*, defined as $\sigma_R^2 = 1.23 C_n^2 k^{7/6} z_L^{11/6}$. For a path length $z_L = 1 \text{ km}$ and wavelength $\lambda = 850 \text{ nm}$, the range of σ_R^2 that we study spans from 0.004 to 4.0.

Let us label the elements of the crosstalk matrix \mathbf{H} by η_{mn} , where m is the

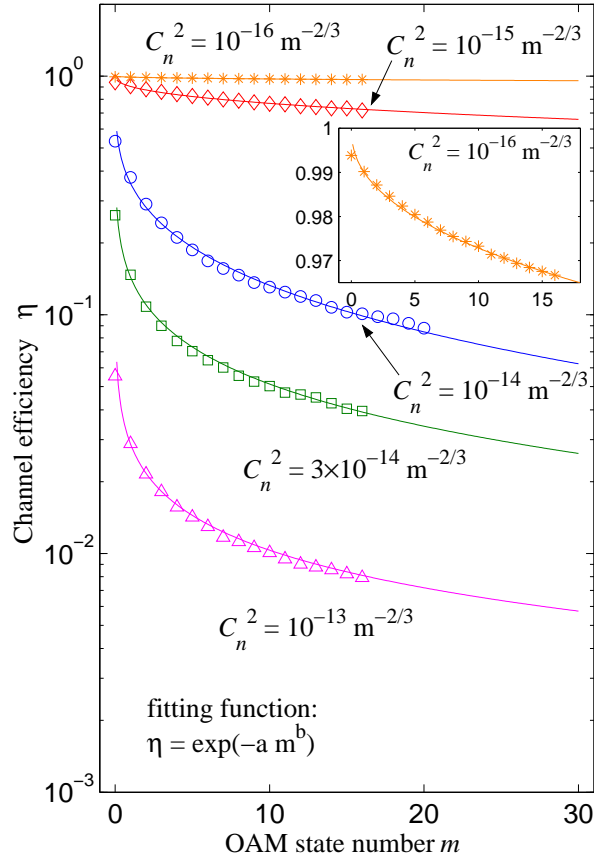


FIGURE 5.4. Transmission efficiency η_{mm} as a function of OAM state, for several values of turbulence strength C_n^2 .

transmitted OAM channel and n is the observed OAM channel at the receiver. The elements on the diagonal of \mathbf{H} , η_{mm} , represent the efficiency of channel m , that is, the fraction of power that remains in the transmitted channel after propagation. Fig. 5.4 shows the channel efficiency η_{mm} of OAM channels +1 to +20 for the 5 values of C_n^2 under consideration. These averages are the same for OAM channels with negative state number, i.e., $\eta_{(-m)(-n)} = \eta_{mn}$. Note that η_{mm} is close to 1 for every m when $C_n^2 = 10^{-16} \text{ m}^{-2/3}$ (a weak dependence on m is, however, apparent in the zoomed-in inset of Fig. 5.4). As turbulence increases, η_{mm} decreases with increasing $|m|$. For

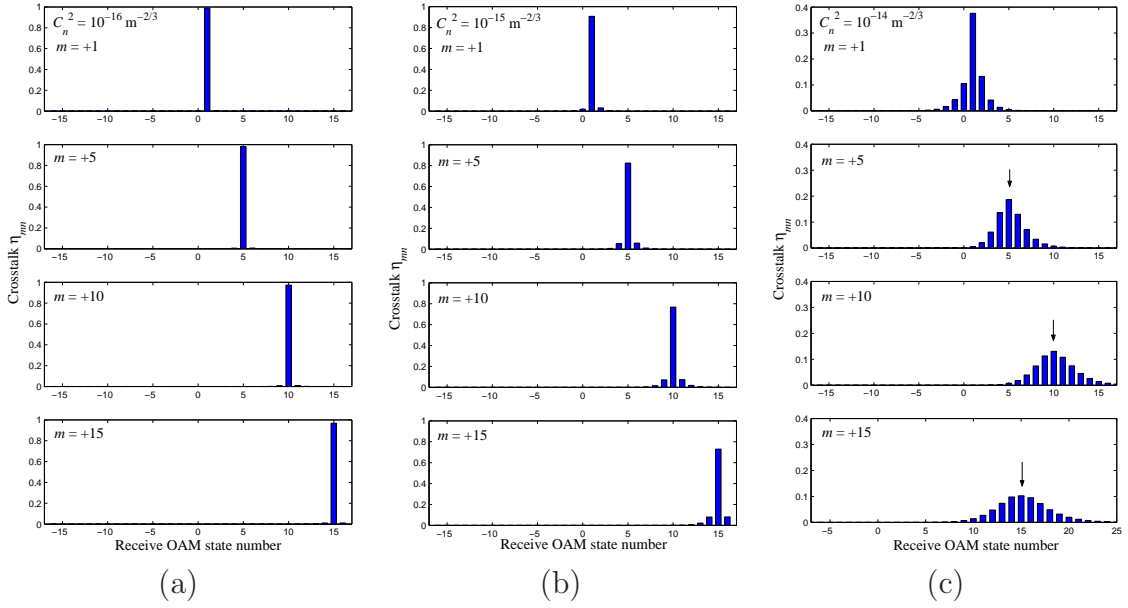


FIGURE 5.5. Average crosstalk η_{mn} observed on OAM channels $n \in \mathcal{S}$ induced by transmit channel $m \in \{+1, +5, +10, +15\}$. In (a), $C_n^2 = 10^{-16} \text{ m}^{-2/3}$; in (b), $C_n^2 = 10^{-15} \text{ m}^{-2/3}$; and in (c), $C_n^2 = 10^{-14} \text{ m}^{-2/3}$.

$C_n^2 = 10^{-13} \text{ m}^{-2/3}$ this decay is severe, ranging from roughly $\eta_{00} = 0.055$ down to $\eta_{1616} = 0.0079$. This is caused by the large spread of energy to adjacent states and/or energy loss from beam spreading. As a consequence, channels with larger OAM state will experience lower SNR. Also, it is clear from Fig. 5.4 that for any given OAM state, η_{mm} decreases with increasing C_n^2 .

5.4.2. OAM crosstalk comparison

The previous discussion refers to the efficiency of each channel alone, which relates to the effective signal power an OAM channel will detect. Crosstalk is the power detected by a receive channel for which the transmitted signal is not intended. This crosstalk is represented by the elements of \mathbf{H} , η_{mn} , for which $m \neq n$. Fig. 5.5 shows histograms of the OAM crosstalk found for (a) $C_n^2 = 10^{-16} \text{ m}^{-2/3}$, (b) $C_n^2 = 10^{-15}$

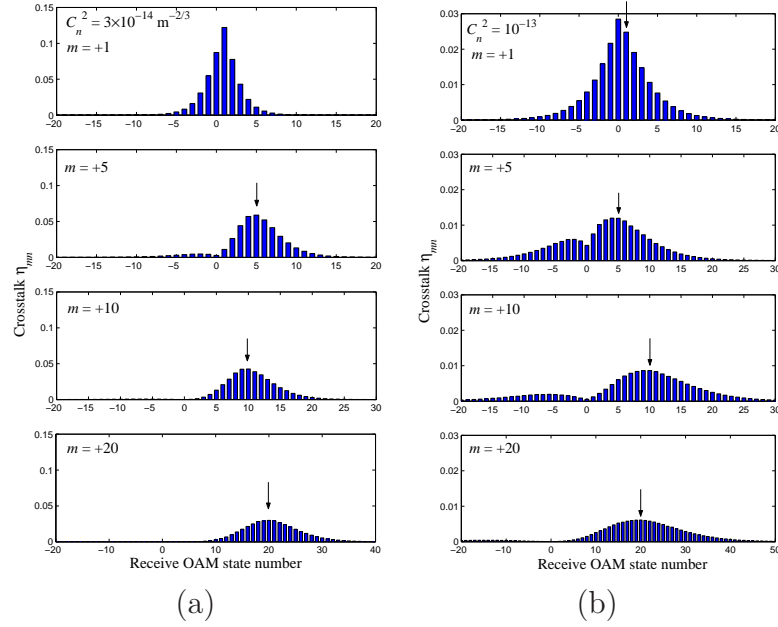


FIGURE 5.6. Average crosstalk η_{mn} observed on OAM channels $n \in \mathcal{S}$ induced by transmit channel $m \in \{+1, +5, +10, +20\}$. In (a), $C_n^2 = 3 \times 10^{-14} \text{ m}^{-2/3}$ and in (b), $C_n^2 = 10^{-13} \text{ m}^{-2/3}$.

$m^{-2/3}$, and (c) $C_n^2 = 10^{-14} \text{ m}^{-2/3}$. In each of the three cases, we present four examples corresponding to the crosstalk generated by transmitting on an isolated channel with $m = 1, 5, 10$, or 15 . Each of these subplots corresponds to a row in \mathbf{H} and, as such, includes the channel efficiency η_{mm} . In case (a) crosstalk among channels is negligible. This manifests in both a large value of η_{mm} and small values of η_{mn} with $m \neq n$. For instance, in the uppermost box of 5.5(a) for which the transmitted OAM state is $m = +1$, $\eta_{11} = 0.99$, $\eta_{12} = 0.0034$, and $\eta_{13} = 0.0004$. The latter two correspond to -24.6 dB and -34 dB of attenuation with respect to η_{11} (decibels in the optical domain). For a transmit channel $m = +10$, $\eta_{1010} = 0.97$, $\eta_{1011} = 0.0092$, and $\eta_{1012} = 0.0019$, corresponding to -20.2 dB and -27 dB, respectively. It can be noted that, as expected from the trends seen in Fig. 5.4, crosstalk to adjacent channels increases with increasing OAM transmit state $|m|$.

In Fig. 5.5(b), $C_n^2 = 10^{-15} \text{ m}^{-2/3}$ and up to four bars of crosstalk are now apparent. For transmit channel $m = +1$, $\eta_{11} = 0.90$, $\eta_{12} = 0.037$, and $\eta_{13} = 0.0043$. Expressed in decibels, the crosstalk is -13.9 dB between channels 1 and 2, and -23.2 dB between channels 1 and 3, indicating a significantly larger interference, compared to that found in case (a). Despite this level of crosstalk, we will show in the next section that multichannel communications can be reliable at this turbulence condition. One can observe the conspicuous increase of crosstalk for higher OAM states. By making another 10-fold increase in C_n^2 , we find that crosstalk in adjacent channels reaches the same order of magnitude as the power remaining in the transmit signal channel. This is shown in Fig. 5.5(c), with $C_n^2 = 10^{-14} \text{ m}^{-2/3}$ (equivalent to $\sigma_R = 0.63$), close to the upper limit of the weak turbulence regime. In this figure we have marked the bar of the transmitted channel with an arrow on top. Note that the distributions of η_{mn} are not symmetric around the transmitted channel. We observe in all cases of Fig. 5.5 that average received energy remains peaked at the transmitted state. Some sample values of crosstalk for $C_n^2 = 10^{-14} \text{ m}^{-2/3}$ and $m = +1$ are $\eta_{11} = 0.38$, $\eta_{13} = 0.041$ (-9.6 dB), and $\eta_{15} = 0.0047$ (-19 dB). For $m = +5$, $\eta_{55} = 0.19$, $\eta_{53} = 0.062$ (-4.8 dB), and $\eta_{51} = 0.0046$ (-16.1 dB). The reader may find the full matrix \mathbf{H} for $C_n^2 = 10^{-14} \text{ m}^{-2/3}$ in the Appendix.

Fig. 5.6 shows the OAM crosstalk for (a) $C_n^2 = 3 \times 10^{-14} \text{ m}^{-2/3}$ and (b) $C_n^2 = 10^{-13} \text{ m}^{-2/3}$. These conditions correspond to $\sigma_R = 1.1$ and $\sigma_R = 2.0$, respectively, in the strong turbulence regime. Again, we have included four examples for each turbulence strength, corresponding to transmit channels $m = 1, 5, 10$, or 20 . In (a) the energy still remains peaked at the transmitted channel but the crosstalk induced on the immediately adjacent channels is nearly as strong as the energy remaining in the signal channel. Energy is in fact spread over all observed channels (and clearly beyond). For

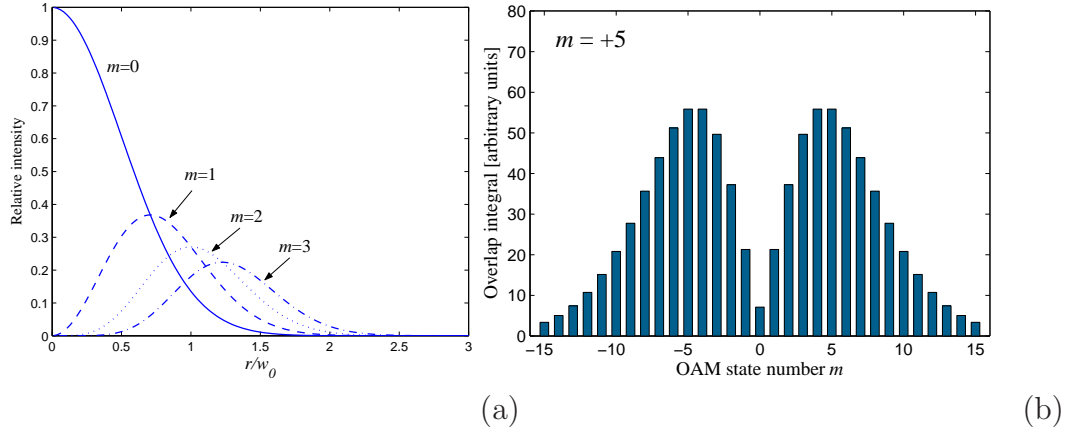


FIGURE 5.7. (a) One-dimensional intensity profile ($\phi = 0$) of some LG modes. (b) Overlap integral of *intensity* distribution of OAM state +5 and those of other OAM states. Note the similarity with the crosstalk for $m = +5$ in 5.6(b).

$C_n^2 = 10^{-13} \text{ m}^{-2/3}$ [shown in Fig. 5.6(b)] the crosstalk is conspicuous in all observed channels. For small values of $|m|$ the energy is not peaked at the transmitted state, but at the state $|m - 1|$. Note also the higher crosstalk observed on channels with negative index. A plausible cause is that for these turbulence levels, OAM fields have lost much of their phase structure and the superposition integral inherent to the channel de-multiplexing operation results in relatively large power for those cases in which the two fields (the distorted received field and the undistorted decoding field) have a geometrically similar intensity distribution. More notable is the null seen at receive channel 0 which, in light of the aforementioned cause, results from a non-overlapping superposition of the intensity maxima between the $m = 0$ mode and the $m \neq 0$ modes. Figure 5.7(a) shows the overlap of the one-dimensional intensity profiles (i.e., $\phi = 0$) for a few values of m . In (b) we have plotted the overlap integral of the unperturbed two-dimensional intensity distribution of OAM state +5 and those of other states. The similarity with the crosstalk bar plot in 5.6(b) for $m = +5$ is striking.

5.5. Aggregate capacity of the OAM-multiplexed system

The channel coefficients determined in the previous section serve the important purpose of characterizing the OAM-multiplexed optical channel. Each channel matrix \mathbf{H} fully determines the communication limits for a fixed receiver noise power. Determining the maximum information rate (i.e., the channel capacity) for such a multiple-input multiple-output channel is a complicated mathematical task (e.g., see [107]). We instead take a simpler approach assuming that the system comprises a set of non-collaborative channels (for instance, the channels are used by independent users without knowledge of other channel's statistics) for which we maximize the information rate, considering a uniform distribution of input symbols in each constituent channel and a uniform power policy among them. Furthermore, it is assumed that crosstalk from each channel is an independent Gaussian noise source that adds to the receiver noise. This intuitive approach gives a lower bound on channel capacity, and is explained in detail below.

5.5.1. Optimal OAM sets

Let us denote a set of M OAM channels by the calligraphic letter \mathcal{O} , where $\mathcal{O} \subset \mathcal{S}$. Each constituent channel $m \in \mathcal{O}$ is modeled as a binary-symmetric channel (BSC). To determine the flip probabilities for each BSC we want to define a SNR per bit that accounts for channel losses and crosstalk. We denote this SNR by γ , defined in the electrical domain as the ratio between the transmit power P_{Tx} times the squared channel efficiency η_{mm} , and the total noise power. Because each contributing crosstalk signal is modeled as an independent Gaussian source, the total noise power on a given channel is determined by the sum of all contributing crosstalk terms and the receiver

noise power N_0 , also modeled as additive white Gaussian. Thus, γ may be written as

$$\gamma \triangleq \frac{\eta_{mm}^2}{\sum_{n \in \mathcal{O}}^{n \neq m} \eta_{nm}^2 + N_0/P_{Tx}}. \quad (5.3)$$

Note that (5.3) has been conveniently arranged to form the term P_{Tx}/N_0 . The term P_{Tx}/N_0 can be varied to control the transmit power. For instance, if P_{Tx}/N_0 is very small in relation to η_{nm} (i.e., the transmit power is low), the system will be limited by detector noise and γ will be small. As the transmit power is increased, the term N_0/P_{Tx} in γ 's denominator becomes smaller. For sufficiently large transmit power, the term N_0/P_{Tx} is negligible and the system becomes crosstalk-limited. This condition is intuitively evident if one considers that large transmit powers induce large crosstalk noise (as the latter grows proportionally), such that for a sufficiently small (fixed) detector noise power, the system's performance will depend on the crosstalk matrix alone.

For a given matrix \mathbf{H} , we seek to find an optimum set of OAM channels in the sense of maximizing the system's aggregated information rate. The optimum set, which we denote by $\hat{\mathcal{O}}$, will depend on the number of channels M , and is found by performing the maximization over all possible subsets of \mathcal{S}

$$\hat{\mathcal{O}} = \arg \max_{\mathcal{O} \subset \mathcal{S}} \sum_{m \in \mathcal{O}} C(p_m), \quad (5.4)$$

with

$$C(p_m) = 1 + p_m \log_2 p_m + (1 - p_m) \log_2(1 - p_m) \quad (5.5)$$

$$p_m = \frac{1}{2} \operatorname{erfc}(\sqrt{\gamma/2}), \quad (5.6)$$

where $C(p_m)$ is the capacity of a BSC with flip probability p_m and $\text{erfc}(\cdot)$ is the complementary error function. The expression in (5.6) assumes orthogonal signal modulation, such as OOK or binary PPM.

For a given \mathbf{H} , there are two design variables that must be specified, namely, the number of OAM channels and the power ratio P_{Tx}/N_0 . Using (5.4)-(5.6) we find the optimum channel sets for every $M \in \{2, 3, \dots, 10\}$ over a large power range. For the weakest turbulence strength considered, $C_n^2 = 10^{-16} \text{ m}^{-2/3}$, the crosstalk is small enough to allow a maximum rate equal to 1 bit per channel, equal to M bits per M parallel channels simultaneously (*bits/M-channels*) for any OAM state number combination, provided the power ratio P_{Tx}/N_0 is large enough. In this case the optimal channel set, at any power level, is simply $\hat{\mathcal{O}} = \{-M/2, \dots, -1, 0, +1, \dots, +M/2 - 1\}$ for even M and $\hat{\mathcal{O}} = \{-\lceil M/2 \rceil, \dots, -1, 0, +1, \dots, +\lfloor M/2 \rfloor\}$ for odd M .

As turbulence strength grows however, the aggregated rate becomes increasingly sensitive to the choice of channels. Optimal OAM state numbers balance the channel efficiency (which decays as $|m|$ increases) with crosstalk (whose effect increases for small channel separation) and detector noise. To show the dependence on transmit power, we plot the optimal state numbers at each power level for a few cases of M and C_n^2 . In Fig. 5.8(a) the optimal OAM state numbers for a 7-channel system in a turbulent atmosphere with $C_n^2 = 10^{-14} \text{ m}^{-2/3}$ are plotted. Note that at very low transmit power the optimal sets are simply $\hat{\mathcal{O}} = \{-3, -2, -1, 0, +1, +2, +3\}$. Crosstalk among these states is clearly significant; however, for small values of P_{Tx} the dominant noise is that of the detector. At $P_{Tx}/N_0 = 20 \text{ dB}$ the optimal set is $\hat{\mathcal{O}} = \{-6, -3, -1, 0, +1, +3, +6\}$. As transmit power is increased greater loss can be tolerated and, therefore, we can afford to use channels with larger m resulting in optima with larger channel separations. For instance, at $P_{Tx}/N_0 = 32 \text{ dB}$ the optimal

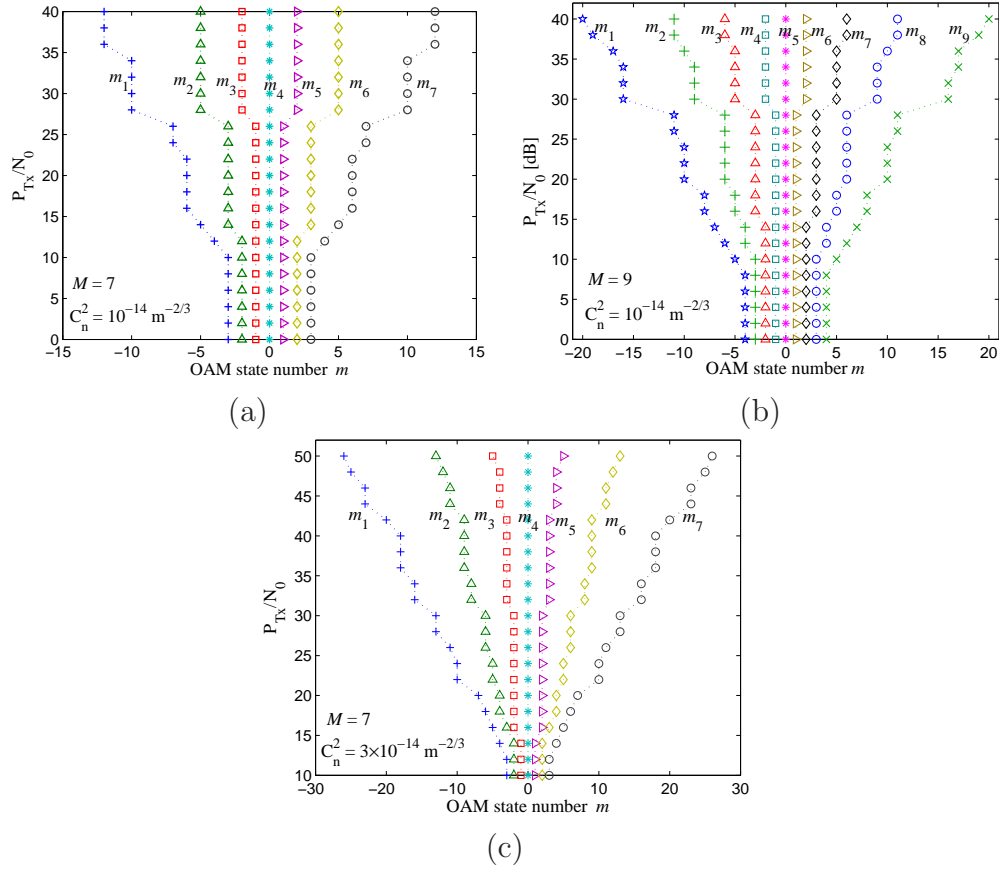


FIGURE 5.8. Optimal OAM channel sets versus P_{Tx}/N_0 , for (a) $M = 7$ and $C_n^2 = 10^{-14} \text{ m}^{-2/3}$, for (b) $M = 9$ and $C_n^2 = 10^{-14} \text{ m}^{-2/3}$, and for (c) $M = 7$ and $C_n^2 = 3 \times 10^{-14} \text{ m}^{-2/3}$.

set is $\hat{\mathcal{O}} = \{-10, -5, -2, 0, +2, +5, +10\}$. Also, note that increasing the transmit power beyond $P_{Tx}/N_0 = 36$ dB will not yield larger optimal channel separation for this turbulence condition, as aggregate capacity is near saturation (i.e., $C \rightarrow 7$). It is promising to see that at this turbulence strength the largest optimal OAM mode needed is $|m| = 10$, corresponding to a receiver aperture of about 15 cm if the design parameters given in section 3.A are employed.

Figure 5.8(b) shows a plot of the optimal OAM state numbers for a system with $M = 9$ channels. The turbulence conditions are the same as those of Fig. 5.8(a).

Table 5.1. Optimal channel sets for $M = 9$ and $P_{Tx}/N_0 = 20$ dB.

C_n^2 [m ^{-2/3}]	Optimal OAM state numbers									
10^{-15}	-6	-4	-2	-1	0	+1	+2	+4	+6	
10^{-14}	-10	-6	-3	-1	0	+1	+3	+6	+10	
3×10^{-14}	-10	-6	-4	-2	0	+2	+4	+6	+10	
10^{-13}	-4	-3	-2	-1	0	+1	+2	+3	+4	

Table 5.2. Optimal channel sets for $M = 9$ and $P_{Tx}/N_0 = 30$ dB.

C_n^2 [m ^{-2/3}]	Optimal OAM state numbers									
10^{-15}	-6	-4	-2	-1	0	+1	+2	+4	+6	
10^{-14}	-16	-9	-5	-2	0	+2	+5	+9	+16	
3×10^{-14}	-22	-13	-6	-2	0	+2	+6	+13	+22	
10^{-13}	-10	-7	-5	-4	0	+4	+5	+7	+10	

At $P_{Tx}/N_0 = 32$ dB the optimal set is $\hat{\mathcal{O}} = \{-16, -9, -5, -2, 0, +2, +5, +9, +16\}$. We repeat the exercise with 7 channels for $C_n^2 = 3 \times 10^{-14}$ m^{-2/3} and find that at $P_{Tx}/N_0 = 32$ dB the optimal set is $\hat{\mathcal{O}} = \{-16, -8, -3, 0, +3, +8, +16\}$. Note that a larger range of OAM state numbers is required (-16 to +16) in comparison to the case of Fig. 5.8(a) with $P_{Tx}/N_0 = 32$ dB (-10 to +10). Moreover, for $C_n^2 = 3 \times 10^{-14}$ m^{-2/3}, $P_{Tx}/N_0 = 32$ dB is no longer near the saturation point of capacity. Therefore, optimal sets require a larger range of state numbers as the transmit power is further increased. For instance, with $M = 7$ and $C_n^2 = 3 \times 10^{-14}$ m^{-2/3}, the optimal set at $P_{Tx}/N_0 = 44$ dB is $\hat{\mathcal{O}} = \{-23, -11, -4, 0, +4, +11, +23\}$, which would require a receive aperture with $D_{Rx} = 23$ cm, approximately.

We summarize our optimization results in tables organized by P_{Tx}/N_0 . Table 5.1 contains the optimal OAM channel sets with $M = 9$ at $P_{Tx}/N_0 = 20$ dB for the considered values of C_n^2 . Table 5.2 presents the optimal sets at $P_{Tx}/N_0 = 30$ dB. In Table 5.3, the power level is $P_{Tx}/N_0 = 40$ dB. All these sets are symmetric around

Table 5.3. Optimal channel sets for $M = 9$ and $P_{Tx}/N_0 = 40$ dB.

C_n^2 [$\text{m}^{-2/3}$]	Optimal OAM state numbers								
10^{-15}	-6	-4	-2	-1	0	+1	+2	+4	+6
10^{-14}	-20	-11	-6	-2	0	+2	+6	+11	+20
3×10^{-14}	-33	-18	-9	-3	0	+3	+9	+18	+33
10^{-13}	-31	-18	-10	-4	0	+4	+10	+18	+31

$m = 0$. In a few cases we obtained slightly non-symmetric optimal sets that we replaced by the closest symmetric set, with a difference in capacity $\Delta C < 0.02$ (with much smaller ΔC at large P_{Tx}/N_0). These differences are within the error of our crosstalk estimation procedure. It is worth noting that at $C_n^2 = 10^{-13} \text{ m}^{-2/3}$, optimal channel separation grows very fast with increasing transmit power. for sufficiently large P_{Tx}/N_0 (relative to channel loss), OAM mode numbers may span to $|m| = 50$ or more. Because our largest OAM mode simulated at this turbulence level is $|m| = 52$, optimal sets were found for only a limited range of transmit power.

The optimal sets in Table 5.4 are organized differently. We have chosen $M = 8$ to illustrate that optimal sets with even numbers of channels are generally not symmetric around OAM state $m = 0$. This is because the efficiency of mode $m = 0$ is superior to that of any other mode, and as such it is part of the optimal set, thus breaking the symmetry of the even-numbered sets. However, we have found a small range of operating conditions for which the optimal sets with even channel count become symmetric (i.e., they exclude state $m = 0$). These cases are observed for $C_n^2 = 10^{-14} \text{ m}^{-2/3}$ and $C_n^2 = 3 \times 10^{-14} \text{ m}^{-2/3}$, and only for values of P_{Tx}/N_0 at which the aggregate capacity is very near saturation. We show a few examples in Table 5.4. This can be explained by observing the following. In turbulence conditions at which crosstalk is significant and when transmit power is such that the system operates in a crosstalk-limited regime (i.e., noise power is negligible), the relatively higher efficiency of state

Table 5.4. Optimum channel sets for $M = 8$ at various power levels.

C_n^2 [m ^{-2/3}]	P_{Tx}/N_0	Optimal OAM state numbers							
10^{-15}	12 dB	-5	-3	-2	-1	0	+1	+2	+4
10^{-15}	18 dB	-6	-4	-2	-1	0	+1	+2	+4
10^{-14}	20 dB	-10	-6	-3	-1	0	+1	+3	+6
10^{-14}	30 dB	-11	-6	-3	-1	+1	+3	+6	+11
3×10^{-14}	40 dB	-33	-18	-9	-3	0	+3	+9	+18
3×10^{-14}	46 dB	-33	-18	-9	-3	+3	+9	+18	+33
10^{-13}	44 dB	-43	-26	-13	-4	0	+7	+18	+35
10^{-13}	48 dB	-49	-31	-15	-5	0	+7	+18	+35

$m = 0$ has lower impact. In such conditions the optimal sets are pushed into a symmetric condition because the channel matrix is symmetric around η_{00} . However, at $C_n^2 = 10^{-13} \text{ m}^{-2/3}$ this phenomenon does not happen because the crosstalk induced by a channel on its counterpart with opposite sign is significant [e.g. see Fig. 5.6 (b)], particularly for small OAM state numbers.

It is important to note that the power ratios P_{Tx}/N_0 given above are per-channel. That is, the total transmit power grows with each additional channel in a set. In the following subsection we present the aggregate capacity of the OAM multi-channel system using this per-channel incremental power scheme. Later we will re-analyze the aggregate capacity under the assumption that total transmit power is fixed and evenly split among the constituent channels.

5.5.2. Aggregate capacity

The optimal sets presented in the previous section were determined by maximizing the aggregate capacity of the collection of independent binary-symmetric channels. Recall that capacity has been determined using γ defined in (5.3), which is the SNR at the receiver. By plotting capacity as a function of P_{Tx}/N_0 all power penalties

caused by turbulence, including channel losses (consequence of beam wander and spreading) and crosstalk have been included. In Figure 5.9 we plot the aggregate capacity in bits/M-channels for (a) $C_n^2 = 10^{-15} \text{ m}^{-2/3}$ with $M = \{1, 2, \dots, 10\}$, for (b) $C_n^2 = 10^{-14} \text{ m}^{-2/3}$ with $M = \{1, 2, \dots, 10\}$, for (c) $C_n^2 = 3 \times 10^{-14} \text{ m}^{-2/3}$ with $M = \{1, 2, \dots, 9\}$, and for (d) $C_n^2 = 10^{-13} \text{ m}^{-2/3}$ with $M = \{1, 2, \dots, 8\}$. Each curve is computed using the optimal channel set at every value of (per-channel) P_{Tx}/N_0 . Therefore, the constituent channels in the optimal channel sets will change along each curve.

On each curve we have marked the P_{Tx}/N_0 point at which the channel with *the worst performance* within the set has a BER= 10^{-5} . This serves as a reference for quality comparisons among systems with different M and different C_n^2 . Because the case with $C_n^2 = 10^{-16} \text{ m}^{-2/3}$ is very similar to that in Fig. 5.9(a) (except for an approximately uniform 3-dB improvement), we refrain from plotting it. We see from Fig. 5.9(a), for which the crosstalk is weak, aggregate capacities show a steady growth with P_{Tx}/N_0 and M . From Fig. 5.9(b), we note that it takes an additional 9 dB of P_{Tx}/N_0 (for $M = 2$) to 19 dB (for $M = 10$) to reach the rates shown in (a), due to the lower efficiency η_{mm} of each constituent channel. At $C_n^2 = 3 \times 10^{-14} \text{ m}^{-2/3}$ [Fig. 5.9(c)], an additional 14.5 dB (for $M = 2$) over the P_{Tx}/N_0 in (b) is required to achieve the same rate, and 11.5 dB if $M = 9$ (a curve with $M = 10$ cannot be completed for this turbulence level given the range of OAM states considered). The power levels required to achieve a large capacity at $C_n^2 = 10^{-13} \text{ m}^{-2/3}$ [Fig. 5.9(d)] are very large. In this case, only systems with optical amplification at the receiver may be feasible, given this system design. However, by using more complex receiver models, capacity is likely to grow faster with transmit power than in the non-collaborative BSC model studied here. As a last note about Fig. 5.9, we observe that in all cases

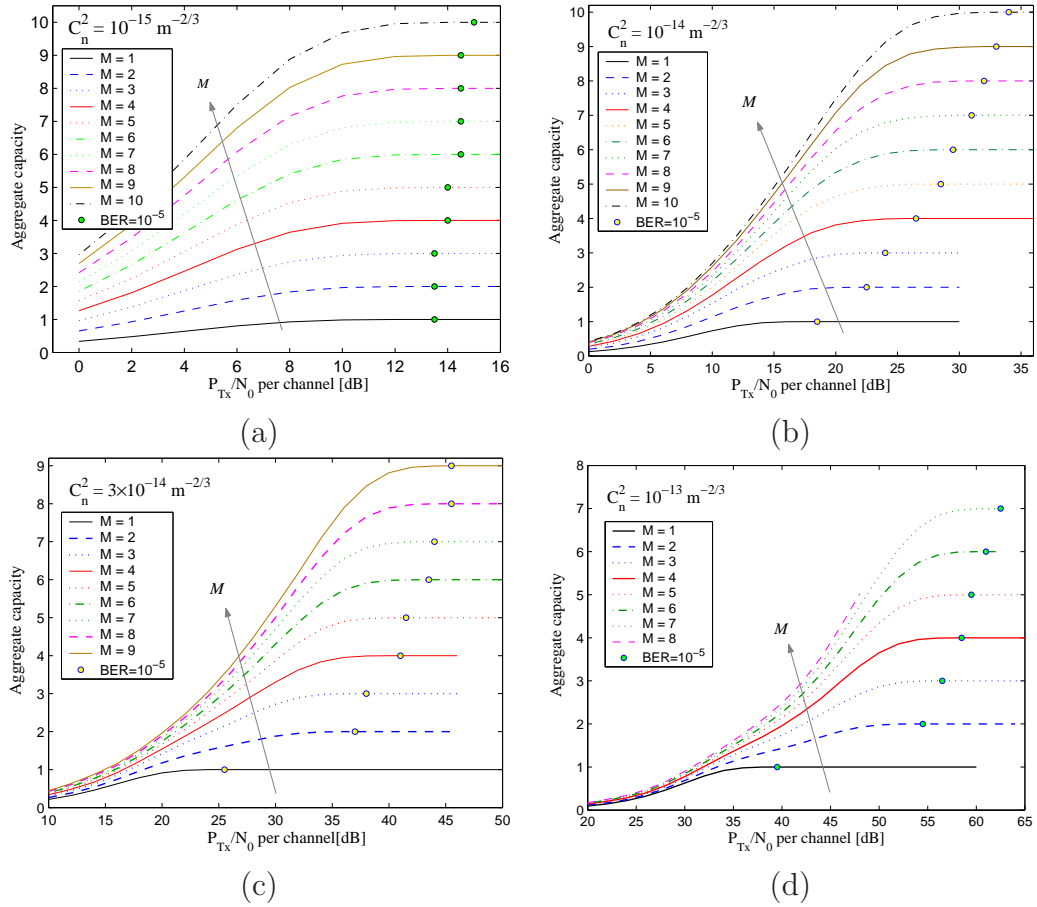


FIGURE 5.9. Aggregate capacity (in bits/M-channels) versus P_{Tx}/N_0 for (a) $C_n^2 = 10^{-15} \text{ m}^{-2/3}$, for (b) $C_n^2 = 10^{-14} \text{ m}^{-2/3}$, for (c) $C_n^2 = 3 \times 10^{-14} \text{ m}^{-2/3}$, and for (d) $C_n^2 = 10^{-13} \text{ m}^{-2/3}$.

capacity has a monotonic growth with M .

5.5.3. Bit-error rate

Knowledge of the optimum number of OAM channels and the aggregate rate at each turbulence condition provides a good measure of the system performance. However, it does not describe the quality of each constituent channel. In Figs. 5.5 and 5.6 we showed that neither efficiency nor crosstalk are symmetric across the OAM channels.

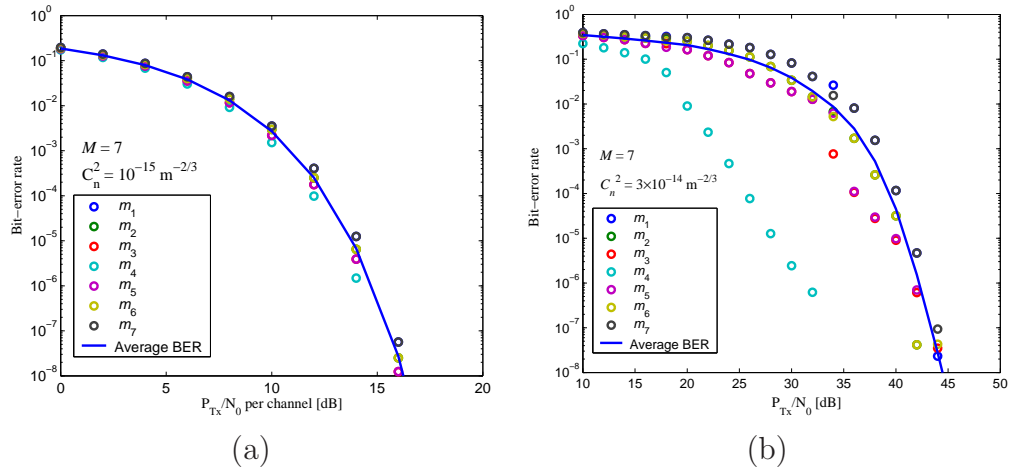


FIGURE 5.10. Bit-error rate versus P_{Tx}/N_0 in dB, with $M = 7$ at (a) $C_n^2 = 10^{-15} \text{ m}^{-2/3}$ and (b) $C_n^2 = 3 \times 10^{-14} \text{ m}^{-2/3}$.

Therefore, we expect to observe nonuniform channel performance within such an OAM multiplexed system. We plot the BER curves for two cases to illustrate this. As seen in the previous graphs, systems operating at $C_n^2 \leq 10^{-15} \text{ m}^{-2/3}$ will have very good performance with low P_{Tx} requirements. We compare a system with $C_n^2 = 10^{-15} \text{ m}^{-2/3}$ [Fig. 5.10(a)] against another with $C_n^2 = 3 \times 10^{-14} \text{ m}^{-2/3}$ [Fig. 5.10(b)]. In each plot, every circle corresponds to the BER of a different constituent channel. At each P_{Tx}/N_0 there are 7 circles (as before, BER is determined using the optimal channel sets). The continuous curves indicate the average BER of these systems. It is evident that BER is not constant within a set (or equivalently, at a given value of P_{Tx}/N_0); however, differences are not significant in (a). In (b), the uneven performance is more apparent, featuring one channel with significantly better BER ($m_4 = 0$) and larger BER differences among the constituent channels in comparison with the BER differences observed in 5.10(a).

5.5.4. Aggregate capacity - fixed system power

We have previously presented the aggregate capacity in systems for which total power grows with the number of channels. This is a reasonable approach for an existent system whose optics may allow additional co-propagating channels without reducing the quality of those already in operation. We now consider the case in which the total power is fixed and any additional channels share the available transmit power uniformly. Figure 5.11 shows the aggregate capacity versus P_{Tx}/N_0 . Because the transmit power is being uniformly distributed, the optimal sets found earlier remain valid. In this case, for a given P_{Tx}/N_0 in Fig. 5.11 the optimal channel set is found using a value $P_{Tx}/N_0 - 10 \log_{10} M$ in Tables 1-4 or in Fig. 5.8. As M grows the capacity curves shift to higher values of P_{Tx}/N_0 as expected. As a consequence, capacity no longer grows monotonically with M . It is apparent in Figs. 5.11(b), (c), and (d) that capacity curves with different M intersect for low values of P_{Tx}/N_0 . It is, therefore, convenient to plot capacity as a function of M to investigate these trends.

In Fig. 5.12 we show the same data that is plotted in Fig. 5.11 with the horizontal axis now corresponding to the number of channels M . Within each plot, a curve shows the aggregate capacity for a given value of total P_{Tx}/N_0 . In (a), for which $C_n^2 = 10^{-15} \text{ m}^{-2/3}$, the curves show a monotonic growth (at least for $M \leq 10$) at all values of P_{Tx}/N_0 . Under these turbulence conditions, ten or more OAM channels can be allocated while keeping the transmit power fixed, provided the optical aperture is large enough. Because the capacity provides diminishing returns as the number of channels grows (i.e., the curves have decreasing slope), the practical number of OAM channels may be chosen to balance the costs of increasing the optical aperture with the marginal increment in aggregate capacity. In Fig. 5.12(b), maxima are

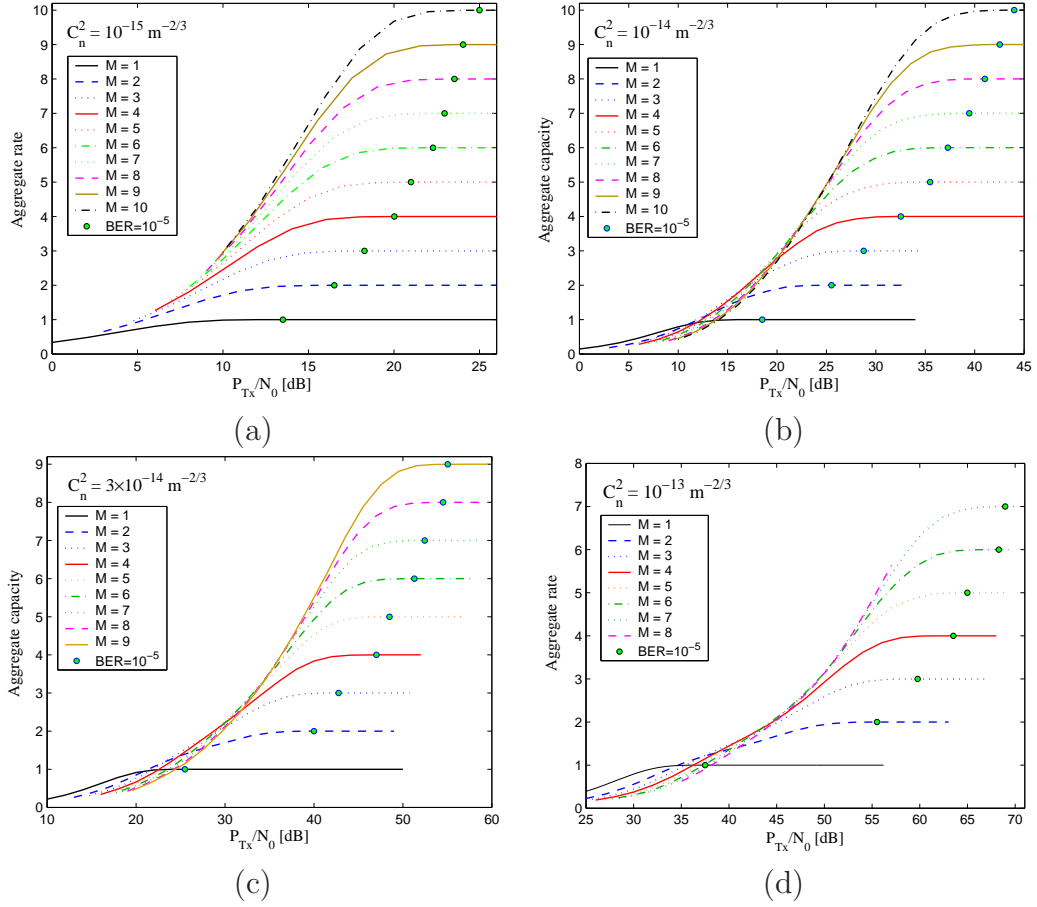


FIGURE 5.11. Aggregate capacity (in bits/M-channels) versus P_{Tx}/N_0 (transmit power fixed) for (a) $C_n^2 = 10^{-15} \text{ m}^{-2/3}$, (b) $C_n^2 = 10^{-14} \text{ m}^{-2/3}$, (c) $C_n^2 = 3 \times 10^{-14} \text{ m}^{-2/3}$, and (d) $C_n^2 = 10^{-13} \text{ m}^{-2/3}$.

observed for curves with $P_{Tx}/N_0 = 12$ dB (at $M = 3$), $P_{Tx}/N_0 = 16$ dB (at $M = 3$), $P_{Tx}/N_0 = 20$ dB (at $M = 5$), and $P_{Tx}/N_0 = 25$ dB (at $M = 9$). At larger P_{Tx}/N_0 , however, no maximum is observed for $M \leq 10$. The existence of maxima in stronger turbulence conditions is explained by the slow growth in aggregate capacity at low P_{Tx}/N_0 for large M [e.g., see Figs. 5.11(c) and (d)], as the available power shared by these channels is not enough to overcome the crosstalk among them. In Fig. 5.12(c), for which $C_n^2 = 3 \times 10^{-14} \text{ m}^{-2/3}$, maxima are observed at curves with $P_{Tx}/N_0 = 20$

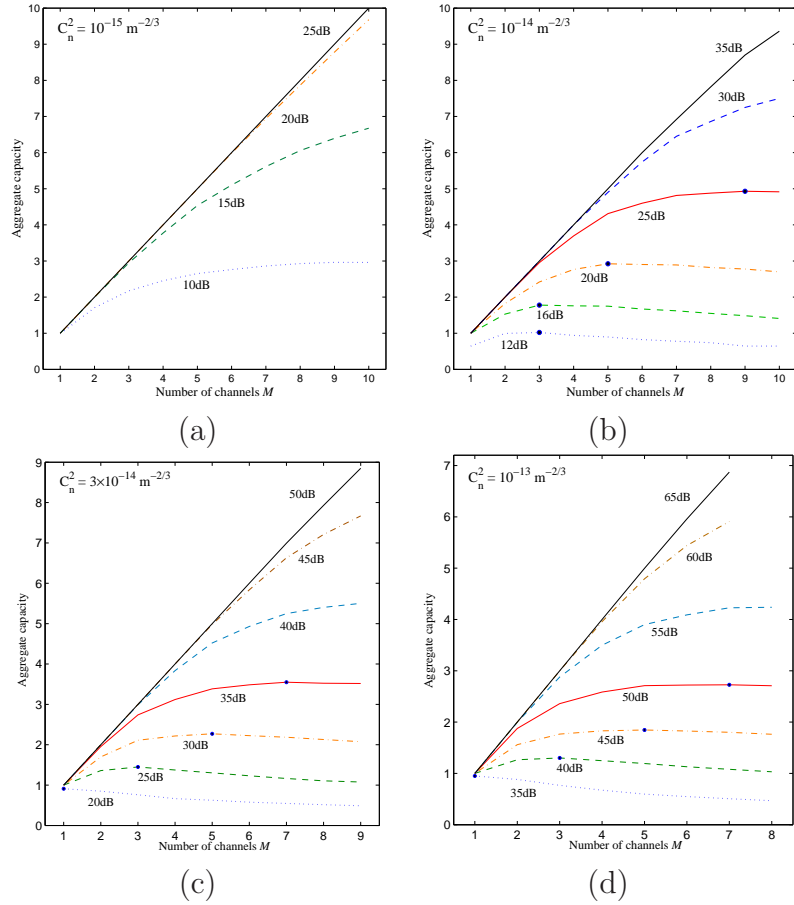


FIGURE 5.12. Aggregate capacity (in bits/M-channels use) versus number of OAM channels M for (a) $C_n^2 = 10^{-15} \text{ m}^{-2/3}$, (b) $C_n^2 = 10^{-14} \text{ m}^{-2/3}$, (c) $C_n^2 = 3 \times 10^{-14} \text{ m}^{-2/3}$, and for (d) $C_n^2 = 10^{-13} \text{ m}^{-2/3}$.

dB (at $M = 1$), with $P_{Tx}/N_0 = 25$ dB (at $M = 3$), with $P_{Tx}/N_0 = 30$ dB (at $M = 5$), and with $P_{Tx}/N_0 = 35$ dB (at $M = 7$). In the case for which $C_n^2 = 10^{-13} \text{ m}^{-2/3}$ [Fig. 5.12(d)], we find maxima up to $P_{Tx}/N_0 = 50$ dB, in which case it occurs at $M = 7$. As mentioned previously in this section, in situations for which the combination of C_n^2 and P_{Tx}/N_0 support the existence of maxima, the design of an OAM-multiplexed system will require the consideration the additional cost incurred in increasing the transmit and receive optics (as well as the additional electronics and holograms) for

the marginal aggregate capacity gained. This will likely result in a channel count smaller than that of the theoretical optimum.

As a final note on the plausibility of further increasing the aggregate capacity of an OAM-multiplexed system, one can think of using additional sets of coaxial OAM modes on parallel optical paths through the existent transmit and receive optical apertures. This approach may benefit from the increased efficiency of OAM modes of small state number, with the additional constraint of fewer total modes in order to avoid overlap.

5.6. Conclusions

Laguerre-Gauss beams can be employed in a multi-channel FSO communication system by exploiting the orthogonality of their OAM states. These beams can be generated and detected with high photon efficiency using volume holograms.

We evaluate the feasibility of an OAM-multiplexed FSO link in atmospheric turbulence by simulating the propagation of LG beams with OAM states $m \in \{-s_{max}, -s_{max}+1, \dots, -1, 0, +1, \dots, +s_{max}-1, +s_{max}\}$ over 1 km in atmospheric turbulence (with s_{max} up to 50+ in the strongest turbulence case considered) and estimating the average attenuation and channel crosstalk. The turbulence strength considered in this study ranges from $C_n^2 = 10^{-16} \text{ m}^{-2/3}$ to $C_n^2 = 10^{-13} \text{ m}^{-2/3}$ corresponding to Rytov variances from $\sigma_R^2 = 0.004$ to $\sigma_R^2 = 4.0$. We find that OAM channels are subjected to increasing attenuation with increasing turbulence strength and observe that channels with larger OAM state number are more strongly affected. We demonstrate that crosstalk among OAM states increases with increasing turbulence strength and find that the power remains peaked at the transmitted OAM state except at the largest

turbulence level evaluated.

We model a set of M co-propagating OAM states as a set of binary symmetric channels and treat the crosstalk induced by the constituent channels as Gaussian noise. Using this model we find optimum sets of OAM states in the sense that the aggregate rate of the system is maximized at each turbulence level considered. Curves of aggregated capacity as a function of P_{Tx}/N_0 (transmit power over detector noise power) are determined using the optimal OAM channel sets for multiplexed systems using up to 10 OAM channels. These rates provide lower bounds to the capacities of OAM-based multichannel FSO systems and demonstrate that good performance can be expected in weak turbulence conditions. Capacity is also determined for systems in which the total transmit power is shared by the constituent OAM channels, yielding optimal points of operation.

6. BETHE FREE ENERGY APPROACH TO LDPC DECODING IN MEMORY CHANNELS

6.1. Introduction

Most transmission media used in current digital communication systems exhibit a non-uniform frequency response. This non-uniform response, which may manifest in amplitude and/or in phase, introduces distortion to the transmitted signal. This distortion induces a spreading of a symbol waveform beyond its allocated time slot. As a result, a sequence of consecutive symbols transmitted through the channel experiences overlaps of their waveforms, such that the individual symbols are no longer identifiable at the receiver. This symbol overlap is commonly referred to as intersymbol interference (ISI). Channel ISI is an undesirable feature as it usually increases the complexity of the receiver and may increase the probability of symbol error in the detection process. ISI is observed, for instance, in fiber-optic channels, in the read-back process of magnetic and optical recording channels, and in radio-frequency wireless channels [108–110].

In many cases, channel ISI can be represented by a linear filter. In a discrete-time system, this filter gives rise to a state-dependent response, where a channel output is a linear combination of the past transmitted symbols. The number of past symbols affecting the output symbol is denoted as *ISI length* or *memory length*. The memory length is one of the dominant factors determining the ability of a receiver to correctly and efficiently detect symbols in the presence of ISI and receiver noise, and a common way to reduce it is equalizing the channel to a target *partial-response*

(PR) channel [111–113]. PR channels are designed with short ISI length, to simplify symbol decoding. A discrete-time PR-equalized channel is usually characterized by its PR *polynomial* or *target* $h(D)$, where D denotes the symbol delay. A PR target must be chosen carefully in order not to boost noise to intolerable levels at frequencies for which the channel response is weak. Symbols transmitted over a PR channel are typically decoded using a maximum likelihood (ML) sequence detector [114], like the Viterbi algorithm, or using a maximum a posteriori (MAP) symbol detector [115], like the Bahl, Cocke, Jelinek, and Raviv (BCJR) algorithm. Errors made in the detector may be controlled by an *error correction code*, typically a linear block code.

A class of linear block codes that has received much recognition in the last decade is that of *low-density parity-check* (LDPC) codes. LDPC codes have been shown to give outstanding bit-error rate (BER) performance while featuring a simple encoding and decoding algorithm based on belief propagation [116–120]. The belief-propagation algorithm, which operates on a graphical representation of the parity-check matrix of a code, involves passing messages (received bit probabilities or likelihoods) from variable nodes to checks nodes, and vice-versa. This message-passing scheme operates locally on bits and checks and can, consequently, lend itself to low-complexity hardware implementations [117].

Even though knowledge of the channel PR polynomial could be exploited by the error correction decoder, in the state-of-the-art receivers symbol detection and error correction are performed separately due to speed and complexity constraints. Roughly, the idea of such sub-optimal algorithms is to provide ISI-free channel symbols as well as their likelihoods to an error-correction decoder. The independence among input symbol likelihoods –assuming that no other a-priori information is available to the decoder– is a necessary condition for successful decoding of LDPC codes

by means of the message passing algorithms mentioned above, an example of which is the sum-product algorithm. For a detailed discussion on the sum-product algorithm (or its variants) the reader is referred to [121]. Most of the proposed alternatives for decoding LDPC codes over ISI channels involve the use of the BCJR algorithm (or its variants) followed by the sum-product algorithm. A significantly more efficient approach is to use the output symbol likelihoods of the sum-product algorithm as extrinsic information to improve the performance of the sequence detector in an iterative feedback scheme. This is known as *turbo equalization*, and is currently the most effective known algorithm to decode LDPC codes on PR channels [122–125]. Turbo equalization entails, however, high complexity and, because of the sequential nature of the BCJR algorithm, may lead to a significant delay.

Simultaneous channel ISI removal and error-correction decoding is preferred if high bit rates and/or short decoding delays are sought. In this direction, noteworthy contributions have been made by Kurkoski, Siegel, and Wolf [109], and by Pakzad and Anantharam [126]. In the former, a PR channel detector performs parallel symbol message-passing between the PR channel state nodes and the variable nodes for a prescribed number of iterations (graphical models for LDPC codes and ISI channels will be introduced in Section 6.2). The resulting symbol likelihoods are later passed to the LDPC decoder. After a number of iterations of the sum-product algorithm, the LDPC decoder feeds its output likelihoods back to the channel detector, thus completing a turbo iteration. The approach in [109] is, therefore, very similar to turbo equalization, but with the advantage of a significantly shorter delay thanks to the parallel channel detector. Nevertheless, the method can only attain the performance of the BCJR-based turbo equalization algorithm if the number of iterations in the PR channel detector is equal to the LDPC codeword length.

It is well known that the inference of marginal probabilities in a graph can only be uniquely accomplished if the graph is a tree. Since the decoding of LDPC codes corresponds to an inference problem for which the graph has loops, the convergence of the message-passing algorithm is not guaranteed. In this regard, the decoding strategy proposed in [126] seeks to redefine the underlying graphical model –comprised by LDPC nodes/checks and PR nodes– in terms of a set of super-nodes or regions. The belief propagation algorithm is applied to the new, region-based graphical model, thus implementing the Generalized Belief Propagation (GBP) strategy introduced in [127, 128]. It was shown in [126], that the GBP-based approach can outperform the decoding approach of [109]. However, one should also be aware of two important caveats of the GBP-based algorithm. First, the selection of regions is not an unambiguous process, but rather a heuristic strategy, lacking a rigorous justification. Therefore, the quality of the algorithm is not universal, but case- (e.g. code-) specific, and it can only be judged upon simulations. Second, increasing the size of the regions improves GBP but it is also computationally expensive, as the overhead grows exponentially with the region size.

This chapter addresses the problem of joint detection and error correction in PR channels. We present, for the first time, a derivation of the belief propagation (BP) equations in a LDPC-coded PR channel. These are obtained by minimizing the Bethe free energy, which is equivalent to performing the exact inference [128] if the graph is loop-free. The derived equations give an explicit solution to the decoding of LDPC codes on general PR channels with pair-wise ISI (i.e., those in which each observed symbol depends on two transmitted symbols), that are corrupted by additive white Gaussian noise. This solution is exact if the LDPC part of the graph does not contain loops and allows a fully parallel implementation on the symbols. The equations reduce

to the well-known BP equation for the memoryless channel [121] in the absence of ISI. We also present a simple yet powerful algorithmic solution to the PR-BP equations. The algorithm features a fully parallel implementation, in the sense that channel detection and LDPC decoding are simultaneously performed on each symbol (after a complete codeword has been received). We evaluate the performance of this algorithm on some LDPC codes over the Dicode channel, for which $h(D) = 1 - D$, and find that it outperforms the turbo equalization algorithm. We illustrate the smooth convergence of PR-BP algorithm towards the ISI-free channel case by evaluating its performance over a channel with $h(D) = 1 + 0.5D$.

The remainder of the Chapter is organized as follows. In Section 6.2 we briefly introduce LDPC codes and their graphical representation. We also introduce a graphical model for LDPC codes on a linear ISI channel. In Section 6.3 the derivation of the BP equations from the Bethe free energy is given, and an iterative decoding algorithm to solve the equations is proposed. In Section 6.4 we present a numerical evaluation of the bit-error rate (BER) versus signal-to-noise ratio (SNR) of several LDPC codes over the Dicode channel. A comparison against the BER performance of a turbo equalizer is also offered to display the excellent convergence of the PR-BP algorithm, particularly with medium- to low-rate codes. A brief comparison of complexity between our approach and that of turbo equalization is offered at the end of Section 6.4. Finally, Section 6.5 summarizes our results.

6.2. Preliminaries on graphical models

6.2.1. Graphical representation of a LDPC code

Let $\mathbf{x} = \{x_1, x_2, \dots, x_N\}$ denote an ordered set of variables each of which can take values from a finite alphabet \mathcal{B} . Let g indicate a function of these variables. A *configuration* of \mathbf{x} denotes a particular realization of \mathbf{x} from the domain $\mathcal{S} = \mathcal{B}^N$, referred to as the *configuration space*. A *marginal* function $g_i(x_i)$ is a function such that for each $\gamma \in \mathcal{B}$, $g_i(\gamma)$ is found by summing $g(\mathbf{x})$ over all those configurations for which $x_i = \gamma$. Namely, the marginal function $g_i(x_i)$ is expressed by [14]

$$g_i(x_i) = \sum_{\mathbf{x} \setminus x_i} g(x_1, x_2, \dots, x_n)$$

where $\mathbf{x} \setminus x_i$ denotes that the summation is over all variables in \mathbf{x} except x_i . Let us assume that $g(\mathbf{x})$ can be expressed as a product of functions f_α whose arguments \mathbf{x}_α are subsets of \mathbf{x} , and α is an element of the index set A . We write $g(\mathbf{x})$ as

$$g(x_1, x_2, \dots, x_n) = \prod_{\alpha \in A} f_\alpha(\mathbf{x}_\alpha), \quad (6.1)$$

and the marginal $g_i(x_i)$ can be written as

$$g_i(x_i) = \sum_{\mathbf{x} \setminus x_i} \prod_{\alpha \in A} f_\alpha(\mathbf{x}_\alpha). \quad (6.2)$$

A factor graph is a bipartite graph whose configuration is determined via (6.1) [129, 130]. In a factor graph, variables x_i are symbolized by variable nodes; factor functions f_α are symbolized by factor nodes; and the dependence of a function on a variable is symbolized by an edge joining the two. It is not difficult to see that

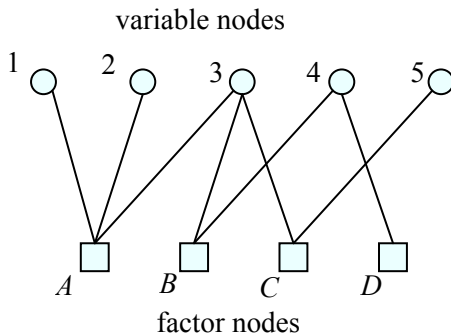


FIGURE 6.1. Factor graph or bipartite graph. Circles correspond to the variable (bit) nodes and the squares correspond to the factor (check) nodes.

every factor graph is a tree. Figure 6.1 depicts an example of a factor graph, in which the variable nodes are represented by circles and the factor nodes are represented by squares. This graph has five variable nodes and four factor nodes. Its structure corresponds to the functional expression

$$g(x_1, x_2, x_3, x_4, x_5) = f_A(x_1, x_2, x_3) f_B(x_3, x_4) f_C(x_3, x_5) f_D(x_4). \quad (6.3)$$

A LDPC code is a linear block code specified by its parity-check matrix \mathbf{H} . This matrix has elements from the set $\{0, 1\}$ and is sparse, i.e., the number of elements 1 is much smaller than the number of elements 0. \mathbf{H} is said to be regular if it features uniform column and row weight; otherwise, it is called irregular. A parity-check matrix \mathbf{H} of M rows and N columns and rank $\text{rank}(H)$ defines a code C with block length N and rate $(N - \text{rank}(H))/N$. Each row of \mathbf{H} defines a parity check equation. A 1 in row j and column i indicates that variable x_i is an argument of the j th parity check equation. A codeword of the code C is a configuration of the ordered set of variables \mathbf{x} for which all the parity check equations are satisfied. If the alphabet \mathcal{B}

is binary with elements from $\text{GF}(2)$, then a codeword of C (in vector representation) satisfies $\mathbf{H} \mathbf{x}^T = \mathbf{0}$ over $\text{GF}(2)$, where $\mathbf{0}$ is an all-zero vector. A bipartite graph in which the parity check equations are represented by factor nodes and the variables x_i by variable nodes is referred to as a *Tanner graph*. A value 1 at row j and column i of \mathbf{H} is represented by an edge between variable node i and factor node j . We define q_i as the node degree (i.e., the number of connected edges) of variable node i and p_j as the node degree of factor node j [117]. A regular LDPC codes has $q_i = q$, $p_j = p$, $\forall i, j$.

6.2.2. The discrete ISI channel

Consider the transmission of a sequence of symbols x_i in discrete time intervals indexed by i . A linear discrete ISI channel relates the output signal y_i with the transmitted signal x_i as

$$y_i = \sum_{j=0}^L h_j x_{i-j} + \xi_i \quad (6.4)$$

where L is the ISI length, h_0, h_1, \dots, h_r are real-valued channel coefficients, and ξ_i is an additive discrete noise process, which we assume to be white and Gaussian with zero mean and variance σ^2 . The relation in (6.4) is commonly referred to as the PR channel. The PR channel is usually represented by the polynomial expression

$$h(D) = \sum_{j=0}^L h_j D^j \quad (6.5)$$

where D is the delay operator, such that $D^j x_i = x_{i-j}$. We assume that the polynomial $h(D)$ is normalized so that $h_0 = 1$. Figure 6.2 shows a graphical representation of (6.5). Each variable x_i is represented by a *hidden* variable node, that is, a variable node that cannot be observed. An output variable y_i is designated by a triangle in

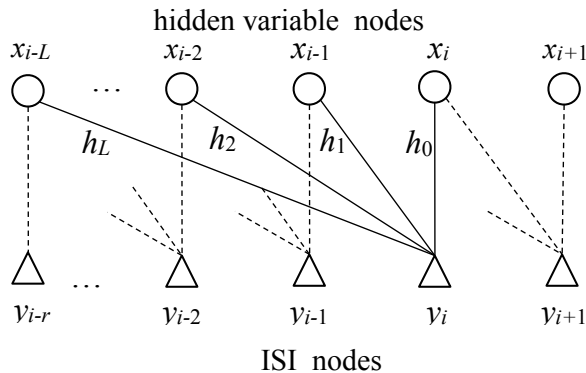


FIGURE 6.2. Graphical representation of a linear ISI channel. The output nodes y_i are a linear combination of the uncorrelated nodes x_i plus additive receiver noise.

the graph, which we denote as an ISI node. ISI nodes include the contribution of additive noise, but to simplify the graph we choose to leave this contribution implicit. We denote the SNR by s^2 and, following [131], is defined as

$$s^2 = \frac{\sum_{j=0}^L h_j^2}{\sigma^2}. \quad (6.6)$$

This definition of SNR accounts for the energy contribution induced by the ISI, so that the energy per symbol is maintained, regardless of the channel coefficients and the memory length L .

6.2.3. Graphical representation of a LDPC code on a discrete ISI channel

An LDPC code operating on an ISI channel can have a graphical representation that combines the graphs in Figs. 6.1 and 6.2. An example of this is the tripartite graph

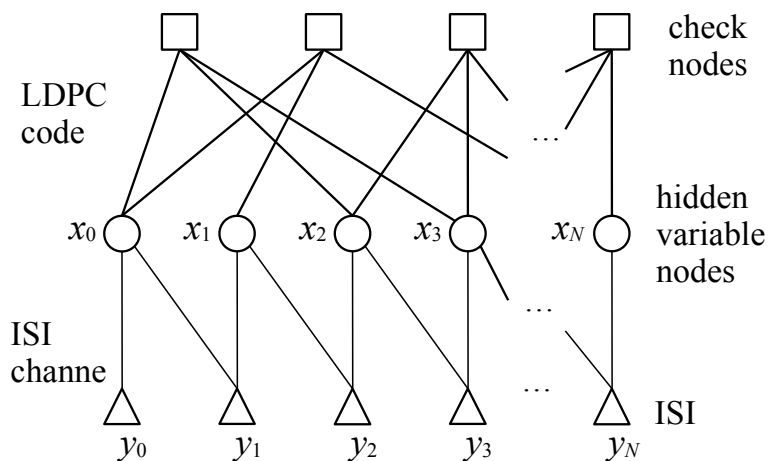


FIGURE 6.3. Factor graph of a LDPC code on a ISI channel with length $L = 1$. Squares, circles, and triangles represent factor nodes, variable nodes, and ISI nodes, respectively.

in Fig. 6.3, which correspond to a linear code on a discrete ISI channel of length L . Provided that the factor nodes in Fig. 6.3 correspond to the parity check equations of the LDPC code, we may interchangeably refer to them as *check nodes*. We have previously denoted the parity check equations by f_α . In addition, we denote the functional representation of the ISI node by f_{\aleph} (\aleph is the first letter of the hebrew alphabet). The tripartite graph in Fig. 6.3 serves as the basis for the derivation of the BP equations over a discrete ISI channel. Note that the left-most ISI node in the graph is assumed to be the first output signal observed. The next section presents the derivation of the belief propagation equations.

6.3. Bethe free energy and belief propagation equations

We begin this Section by briefly introducing the concept of beliefs and the Bethe free energy. The reader may find a thorough description of the BP algorithm and its relation to the Bethe free energy in [128]. A belief $b_i(x_i)$ at the variable node i is an approximation to the exact marginal function $g_i(x_i)$ [128]. We can extend this definition to the other types of nodes in the graph shown in Fig. 6.3. The joint belief $b_\alpha(\mathbf{x}_\alpha)$ at the set of variables \mathbf{x}_α (which in turn corresponds to the belief of the factor node f_α) is an approximation to the exact marginal function $g_\alpha(\mathbf{x}_\alpha)$. Similarly, the joint belief $b_{\aleph}(\mathbf{x}_{\aleph})$ of the set of variables \mathbf{x}_{\aleph} , corresponding to the variable nodes connected to the ISI node \aleph , is an approximation to the exact marginal function $g_{\aleph}(\mathbf{x}_{\aleph})$.

It is of interest to compute the marginal function mentioned above, because they represent the probabilities of the transmitted symbols. However, even with the knowledge of the global function $g(\mathbf{x})$, this may be a very difficult computational task. We may use the BP equations to approximate the marginal functions by means of the beliefs.

6.3.1. Bethe free energy approach to the decoding of LDPC codes in a PR channel

The BP equations correspond to the stationary points of a function of the beliefs called the Bethe free energy [128]. The Bethe free energy, expressed as a function of the beliefs $b_\alpha(\mathbf{x}_\alpha)$ and $b_{\aleph}(\mathbf{x}_{\aleph})$ on the check, and the ISI nodes, respectively, is

$$F[b_\alpha(\mathbf{x}_\alpha), b_{\aleph}(\mathbf{x}_{\aleph})] = U[b_\alpha(\mathbf{x}_\alpha), b_{\aleph}(\mathbf{x}_{\aleph})] - H[b_\alpha(\mathbf{x}_\alpha), b_{\aleph}(\mathbf{x}_{\aleph})], \quad (6.7)$$

where the Bethe self energy U is

$$U [b_\alpha(\mathbf{x}_\alpha), b_\aleph(\mathbf{x}_\aleph)] = - \sum_\alpha \sum_{\mathbf{x}_\alpha} b_\alpha(\mathbf{x}_\alpha) \ln f_\alpha(\mathbf{x}_\alpha) - \sum_\aleph \sum_{\mathbf{x}_\aleph} b_\aleph(\mathbf{x}_\aleph) \ln f_\aleph(\mathbf{x}_\aleph) \quad (6.8)$$

and the Bethe entropy H is

$$\begin{aligned} H [b_i(x_i), b_\alpha(\mathbf{x}_\alpha), b_\aleph(\mathbf{x}_\aleph)] &= \sum_\alpha \sum_{\mathbf{x}_\alpha} b_\alpha(\mathbf{x}_\alpha) \ln b_\alpha(\mathbf{x}_\alpha) - \sum_\aleph \sum_{\mathbf{x}_\aleph} b_\aleph(\mathbf{x}_\aleph) \ln b_\aleph(\mathbf{x}_\aleph) \\ &\quad + \sum_i (q_i - 1) \sum_{x_i} b_i(x_i) \ln b_i(x_i). \end{aligned} \quad (6.9)$$

In a tree-like graph, the Bethe free energy is a concave function on the beliefs such that at its minimum points, $b_\alpha(\mathbf{x}_\alpha) = g_\alpha(\mathbf{x}_\alpha)$ and $b_\aleph(\mathbf{x}_\aleph) = g_\aleph(\mathbf{x}_\aleph)$, the desired marginal functions, and $F = F_{\text{free}}$, the free energy. Since it is of interest to interpret the beliefs as probability mass functions, the normalization constraints

$$\sum_{x_i} b_i(x_i) = \sum_{\mathbf{x}_\alpha} b_\alpha(\mathbf{x}_\alpha) = \sum_{\mathbf{x}_\aleph} b_\aleph(\mathbf{x}_\aleph) = 1, \quad (6.10)$$

and the consistency constraints

$$b_i(x_i) = \sum_{\mathbf{x}_\alpha \setminus x_i} b_\alpha(\mathbf{x}_\alpha) = \sum_{\mathbf{x}_\aleph \setminus x_i} b_\aleph(\mathbf{x}_\aleph), \quad (6.11)$$

must be satisfied.

The probability of observing the channel output vector \mathbf{y} , given the binary input vector $\mathbf{x} \in \{-1, 1\}^N$ and the SNR s^2 , is

$$P(\mathbf{y}|\mathbf{x}) \propto \exp \left[-\frac{s^2}{2} \sum_{i=1}^N \left(y_i - \sum_{j=0}^L h_j x_j \right)^2 \right] \quad (6.12)$$

provided that the discrete additive noise process is white and Gaussian. After expanding (6.12) and discarding the constant terms, we obtain

$$P(\mathbf{y}|\mathbf{x}) \propto \exp\left(\sum_{i=1}^N u_i x_i\right) \exp\left(-\sum_{(i,j), 1 \leq |i-j| \leq L} Q_{j-i} x_j x_i\right), \quad (6.13)$$

where the summation on the right-most exponent is over all pairs (i, j) of distinct bits separated by a distance $(i, j), 1 \leq |i - j| \leq L$, and we have defined

$$u_i = s^2 \sum_{j=0}^L h_j y_j, \quad Q_p = s^2 \sum_{k=0}^{|p-L|} h_k h_{k+p}. \quad (6.14)$$

With u_i we symbolize the likelihood of the variable node i . For $L = 0$, u_i takes the form of the likelihood of a Gaussian memoryless channel. Q_p accounts for the pair-wise memory.

Following the approach in [128, 132], we would like to write the joint probability distribution function of the random vector \mathbf{X} representing the binary symbols of a codeword with a product of functions such that the probability of the configuration $\mathbf{x} = \{x_1, x_2, \dots, x_N\}$, $p(\mathbf{x})$, is given by

$$p(\mathbf{x}) = \frac{1}{Z} \prod_{\alpha \in A} f_{\alpha}(\mathbf{x}_{\alpha}) \prod_{\aleph \in \beth} f_{\aleph}(\mathbf{x}_{\aleph}) \quad (6.15)$$

where $\{f_{\alpha}(\mathbf{x}_{\alpha})\}$ is a set of M non-negative functions as defined in Section 6.2. Similarly, $\{f_{\aleph}(\mathbf{x}_{\aleph})\}$ is a set \beth of N non-negative functions indexed by \aleph whose arguments \mathbf{x}_{\aleph} are subsets of \mathbf{x} . In (6.15), Z is a normalization constant given by

$$Z = \sum_{\mathbf{x}} \prod_{\alpha \in A} f_{\alpha}(\mathbf{x}_{\alpha}) \prod_{\aleph \in \beth} f_{\aleph}(\mathbf{x}_{\aleph}) \quad (6.16)$$

such that $\sum_{\mathbf{x}} p(\mathbf{x}) = 1$, i.e., $p(\mathbf{x})$ is a probability mass function. The purpose of expressing the joint probability distribution in this fashion is to conveniently represent the factor graph in Fig. 6.3, in which $\{f_\alpha(\mathbf{x}_\alpha)\}$ describes the check nodes of the LDPC parity-check matrix, and $\{f_{\aleph}(\mathbf{x}_{\aleph})\}$ describes the observed ISI nodes. By writing

$$f_\alpha(\mathbf{x}_\alpha) \equiv \delta \left(\prod_{x_j \in \mathbf{x}_\alpha} x_j, 1 \right) \exp \left(q_i^{-1} \sum_{x_i \in \mathbf{x}_\alpha} x_i u_i \right) \quad (6.17)$$

$$f_{\aleph}(\mathbf{x}_{\aleph}) \equiv \exp \left(-Q_{|j-i|} x_i x_j \right), \quad (6.18)$$

where $\delta(v, 1) = 1$ for $v = 1$ (the parity-check equation is satisfied) and 0 otherwise, we obtain

$$p(\mathbf{x}) = \frac{1}{Z} \prod_{\alpha=1}^M \delta \left(\prod_{x_j \in \mathbf{x}_\alpha} x_j, 1 \right) \prod_{i=1}^N \exp(u_i x_i) \prod_{(i,j), 1 \leq |i-j| \leq L} \exp(-Q_{j-i} x_j x_i). \quad (6.19)$$

The Bethe free energy is then minimized with respect to the beliefs b_i , b_α , and b_{\aleph} subject to the normalization and consistency constraints in (6.10) and (6.11). Namely, we minimize the Lagrangian function

$$\begin{aligned} \mathcal{L} = & U - H + \sum_{\alpha} \gamma_{\alpha} \left(\sum_{\mathbf{x}_\alpha} b_{\alpha}(\mathbf{x}_\alpha) - 1 \right) + \sum_{\aleph} \gamma_{\aleph} \left(\sum_{\mathbf{x}_{\aleph}} b_{\aleph}(\mathbf{x}_{\aleph}) - 1 \right) \\ & + \sum_i \gamma_i \left(\sum_{x_i} b_i(x_i) - 1 \right) + \sum_i \sum_{\alpha \ni i} \sum_{x_i} \lambda_{i\alpha}(x_i) \left[b_i(x_i) - \sum_{\mathbf{x}_\alpha \setminus x_i} b_{\alpha}(\mathbf{x}_\alpha) \right] \\ & + \sum_i \sum_{\aleph \ni i} \sum_{x_i} \lambda_{i\aleph}(x_i) \left[b_i(x_i) - \sum_{\mathbf{x}_{\aleph} \setminus x_i} b_{\aleph}(\mathbf{x}_{\aleph}) \right], \end{aligned} \quad (6.20)$$

where $\alpha \ni i$ and $\aleph \ni i$ indicate all indices of the checks and of the ISI nodes connected to bit i , respectively, and $\gamma_i, \gamma_\alpha, \gamma_{\aleph}, \lambda_{i\alpha}(x_i), \lambda_{i\aleph}(x_i)$ are Lagrange coefficients that mul-

tiply the normalization constraints (6.10) and the consistency constraints (6.11). The minimization of (6.20) with respect to the beliefs leads to

$$b_\alpha(\mathbf{x}_\alpha) = f_\alpha(\mathbf{x}_\alpha) \exp \left[-\gamma_\alpha - 1 + \sum_{i \in \alpha} \lambda_{i\alpha}(\sigma_i) \right], \quad (6.21)$$

$$b_\aleph(\mathbf{x}_\aleph) = f_\aleph(\mathbf{x}_\aleph) \exp \left[-\gamma_\aleph - 1 + \sum_{i \in \aleph} \lambda_{i\aleph}(x_i) \right], \quad (6.22)$$

$$b_i(x_i) = \exp \left[\frac{1}{q_i + L - 1} \left(\gamma_i + \sum_{\alpha \ni i} \lambda_{i\alpha}(x_i) + \sum_{\aleph \ni i} \lambda_{i\aleph}(x_i) \right) - 1 \right]. \quad (6.23)$$

Equations (6.21)-(6.23) complemented by the normalization and the consistency constraints form a close system of BP equations for the $\lambda_{i\alpha}(x_i)$ and $\lambda_{i\aleph}(x_i)$ coefficients. Following the traditional notation of BP equations in terms of the fields η defined on the edges of the factor graph, we have the relations

$$\eta_{i\alpha} \equiv \frac{\lambda_{i\alpha}(+1) - \lambda_{i\alpha}(-1)}{2} + \frac{h_i}{q_i}, \quad \eta_{i\aleph} \equiv \frac{\lambda_{i\aleph}(+1) - \lambda_{i\aleph}(-1)}{2}, \quad (6.24)$$

where $\eta_{i\alpha}$ indicates the field going from variable node i to factor node α , and $\eta_{i\aleph}$ indicates the field going from variable node i to ISI node \aleph . Substituting (6.24) in (6.21)-(6.23) yields the expressions

$$\sum_{\mathbf{x}_\alpha} x_i b_\alpha(\mathbf{x}_\alpha) = \tanh \left[\eta_{i\alpha} + \tanh^{-1} \left(\prod_{\substack{j \neq i \\ j \in \alpha}} \tanh \eta_{j\alpha} \right) \right], \quad (6.25)$$

$$\sum_{\mathbf{x}_\aleph} x_i b_\aleph(\mathbf{x}_\aleph) = \tanh \left(\eta_{i\aleph} - \tanh^{-1} (\tanh \eta_{i\aleph} \tanh Q_\aleph) \right), \text{ s.t. } (i, j) \in \aleph, \quad (6.26)$$

$$\sum_{x_i} x_i b_i(x_i) = \tanh \left(\frac{\sum_{\alpha \ni i} [\lambda_{i\alpha}(+1) - \lambda_{i\alpha}(-1)] + \sum_{\aleph \ni i} [\lambda_{i\aleph}(+1) - \lambda_{i\aleph}(-1)]}{2(q_i + L - 1)} \right). \quad (6.27)$$

By equating the right-hand sides of (6.25), (6.26), and (6.27), and using (6.24),

after some algebraic manipulations we find the BP equations for the ISI channel:

$$\eta_{i\alpha} = u_i + \sum_{\substack{\beta \neq \alpha \\ \beta \ni i}} \tanh^{-1} \left(\prod_{\substack{j \neq i \\ j \in \beta}} \tanh \eta_{j\beta} \right) - \sum_{\aleph \ni i} \tanh^{-1} (\tanh \eta_{i\aleph} \tanh Q_{\aleph}), \quad (6.28)$$

$$\eta_{i\aleph} = u_i - \sum_{\substack{\beth \neq \aleph \\ \beth \ni i}} \tanh^{-1} (\tanh \eta_{i\beth} \tanh Q_{\beth}) + \sum_{\alpha \ni i} \tanh^{-1} \left(\prod_{\substack{j \neq i \\ j \in \alpha}} \tanh \eta_{j\alpha} \right). \quad (6.29)$$

where the hebrew letter \beth is used to indicate those ISI nodes that are connected to the variable node i but are not \aleph .

It can be observed in (6.28)-(6.29) that in the absence of ISI, $Q_{\aleph} = 0$ and the equations reduce to the well known BP equations for memoryless channels.

Equations (6.28)-(6.29) form the exact BP solution to the PR channel with pairwise ISI, regardless of the distance between the two variable nodes joint by an ISI node. In a factor graph whose PR nodes do not form loops (in the absence of the check nodes), the solution is exact in the sense that the fields determined correspond to the stationary points of the Bethe free energy. Of course, the check nodes of the LDPC code add loops to the graph, and therefore, the convergence of the fields is not guaranteed. The BP equations above can be used to decode the message symbols of a LDPC code over a discrete PR channel with polynomial

$$h(D) = 1 - \alpha D^n, \quad (6.30)$$

where $-1 \leq \alpha \leq 1$ and n is a non-negative integer. For ISI involving more than two variable nodes, the solution is suboptimal even in the absence of the check nodes because the ISI nodes and the variable nodes will form loops.

The BP equations are nonlinear and the roots can be evaluated with the method of preference. In the next subsection we describe a simple iterative procedure to solve

the BP equations, analogous to the message-passing algorithm applied to memoryless channels.

6.3.2. Algorithmic solution to the BP equations

The nonlinear PR-BP equations described above can be solved using any nonlinear minimization algorithm. However, in the interest of finding a simple and fully-parallel decoding algorithm, we follow an iterative approach similar to that of message-passing for LDPC codes on memoryless channels. Equations (6.28)-(6.29) can be iteratively decoded using the following algorithm:

$$\eta_{i\alpha}^{(n+1)} = u_i + \sum_{\beta \ni i}^{\beta \neq \alpha} \mu_{i\beta} - \sum_{\aleph \ni i} \zeta_{i\aleph} \quad (6.31)$$

$$\eta_{i\aleph}^{(n+1)} = u_i - \sum_{\beth \ni i}^{\beth \neq \aleph} \zeta_{i\beth} + \sum_{\alpha \ni i} \mu_{i\alpha} \quad (6.32)$$

with

$$\mu_{i\beta} = \tanh^{-1} \left(\prod_{\substack{j \neq i \\ j \in \beta}} \tanh \eta_{j\beta}^{(n)} \right) \quad (6.33)$$

$$\zeta_{i\aleph} = \tanh^{-1} \left(\tanh \eta_{i\aleph}^{(n)} \tanh Q_{\aleph} \right) \quad (6.34)$$

The superscript $(n + 1)$ refers to the value of the field η at iteration step $n + 1$. Decoding starts when all ISI symbols associated with a LDPC codeword have been received. The algorithm is initialized by setting all $\mu_{i\beta}, \zeta_{i\aleph}$ to zero. It is assumed that the symbols transmitted prior and posterior to the codeword are on a known state. Using terminating nodes with known states is not strictly necessary when the channel has memory length $L = 1$, as convergence is enforced by the check equations.

However it helps achieving a faster convergence and it is also common practice in the evaluation of decoders on PR channels. The fields in (6.31) and (6.32) are evaluated using the values $\mu_{i\beta}, \zeta_{i\mathbb{N}}$, computed in the previous iteration to replicate a fully-parallel architecture at each iteration. After every iteration, the likelihood Λ_i on each variable node i is computed as

$$\Lambda_i = u_i + \sum_{\alpha \ni i} \mu_{i\alpha} \quad (6.35)$$

and the codeword is checked. Note that the summation is in this case over all the check nodes a connected to variable node i . In the next section we present a BER evaluation of some LDPC codes using this iterative algorithm on a Dicode channel.

6.4. Numerical simulations

As we have already mentioned, the exact solution given above does not guarantee convergence to a valid codeword because linear block codes generate graphs with loops. It is well-known, however, that very good convergence is generally observed using the sum-product algorithm on graphs with loops such as those generated by LDPC codes [119]. We expect this to be also true for the BP equations presented here. To illustrate this, we have numerically performed the transmission and decoding of random LDPC codewords on a Dicode channel, given by the polynomial $h(D) = 1 - D$ by means of Monte Carlo simulations. We have done this for various LDPC codes using the algorithm in (6.31)-(6.34) with the initialization given in (6.14). Clearly, for the Dicode channel $h_0 = 1$, $h_1 = -1$, and $Q_1 = -s^2$. Each channel observation y_i is computed using (6.4), in which x_i is a LDPC-coded binary symbol that takes values from $\{-1, +1\}$, and ξ_i is a AWGN sample from the normal distribution $N(0, \sigma^2)$.

In the following subsections we present the BER vs. SNR curves obtained from

the abovementioned simulations. Because the BER performance of a code on an ISI channel may depend on the transmitted codeword, we determine the generator matrix of the code by means of Gaussian elimination and encode randomly generated sequences of equiprobable bits. For each LDPC code considered, we have included the BER performance obtained from the turbo equalization scheme [122] for comparison purposes. Decoding using turbo equalization was performed in the following way. Each turbo iteration consisted of one pass of the BCJR algorithm followed by S iterations of the sum-product algorithm. If T is the number of turbo iterations, we selected T such that $T(S + 1)$ would equal (or be near) the number of iterations J of the PR-BP algorithm. It is worth mentioning that T and S were chosen to achieve the best performance of the turbo equalization algorithm, and were in fact different for different LDPC codes.

6.4.1. Length-495, rate 0.875 (quasi) regular LDPC code

We first consider the MacKay (495,433) code, with rate 0.875, column weight 3 and row weight 24 [133]. This is a slightly irregular code, as it features three parity-check equations with weight 23. This code has been previously considered in the joint-decoding works published in [109] and [126].

Figure 6.4 depicts the BER versus SNR in decibels. We use the definition of SNR given in (6.6). In this and in the next examples, a power penalty is applied to the SNR to account for the code redundancy, and is given by $10 \log_{10} R$, where R is the code rate. In this example, the penalty equals 0.58 dB. In Fig. 6.4, the curve with black square markers shows the BER performance of the code on a memoryless channel obtained making 20 iterations of the sum-product algorithm. This curve may serve as a lower bound to the code performance in a ISI channel. The curve with open

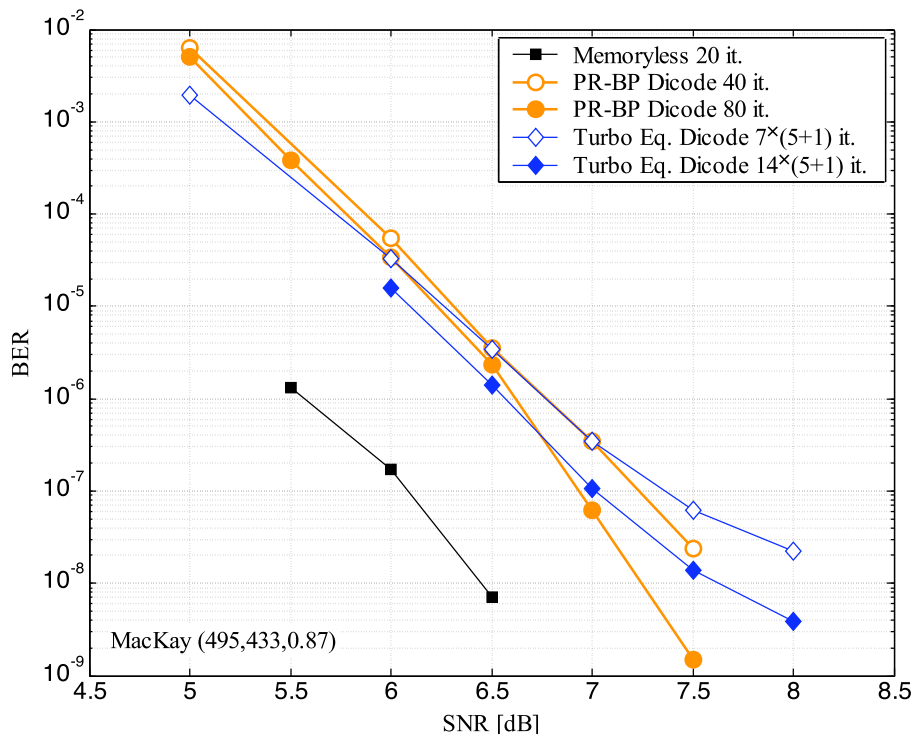


FIGURE 6.4. BER versus SNR in dB of the MacKay(495,433) rate 0.875 (quasi) regular code performing on both a memoryless and a Dicode channel.

circle markers was obtained with the PR-BP algorithm using 40 iterations, while the curve with filled circle markers corresponds to 80 iterations of the same algorithm.

The curves with open and filled diamond markers were obtained using turbo equalization with $8 \times (5+1)$ iterations and $16 \times (5+1)$ iterations, respectively. Note that at high SNR these curves show an error floor, whereas those from the PR-BP algorithm do not. We observe a decoding gain of about 0.5 dB at $\text{BER} = 10^{-8}$.

6.4.2. Length-4095, rate 0.82, (quasi) regular LDPC code

Our second example considers a code with block length 4095 and rate 0.82 [133]. This code features column weight of 4 and row weights 22 and 23. We simulate this code on both a memoryless channel and a Dicode channel using randomly-generated

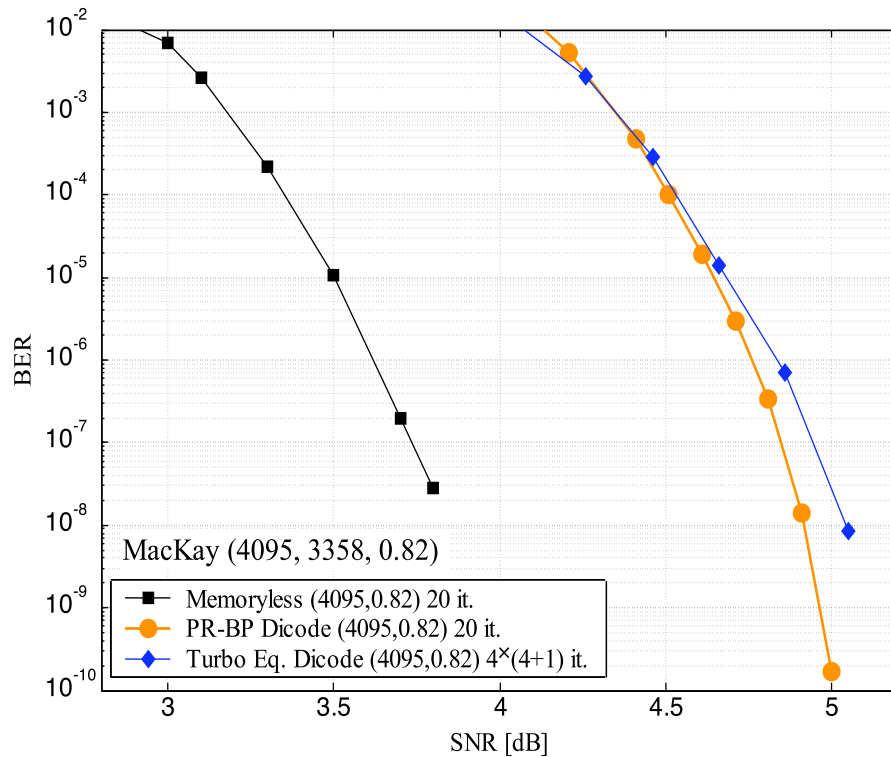


FIGURE 6.5. BER versus SNR in dB of the MacKay (4095,3358) rate 0.82 (quasi) regular code performing on both a memoryless and a Dicode channel.

codewords. Figure 6.5 shows the BER curves of this code. The memoryless channel is decoded using 20 iterations of the sum-product algorithm, and its BER curve is shown with square markers. The results using the PR-BP algorithm with 20 iterations is depicted by the curve with circle markers. The curve with diamond markers represent the performance of the turbo equalization algorithm using $4 \times (4 + 1)$ iterations. Note the low BER values achieved with the PR-BP algorithm (2×10^{-10}) at SNR = 5 dB. As with the code in the previous subsection, the BER curves on the Dicode channel exhibit a cross-over, with a steeper slope in the case of the PR-BP algorithm. We observe again that with high-rate codes the improvement over turbo equalization can only be seen at low BER. At BER = 10^{-8} , the decoding gain is 0.15 dB. This gain, however, increases for lower rate codes, as we show next.

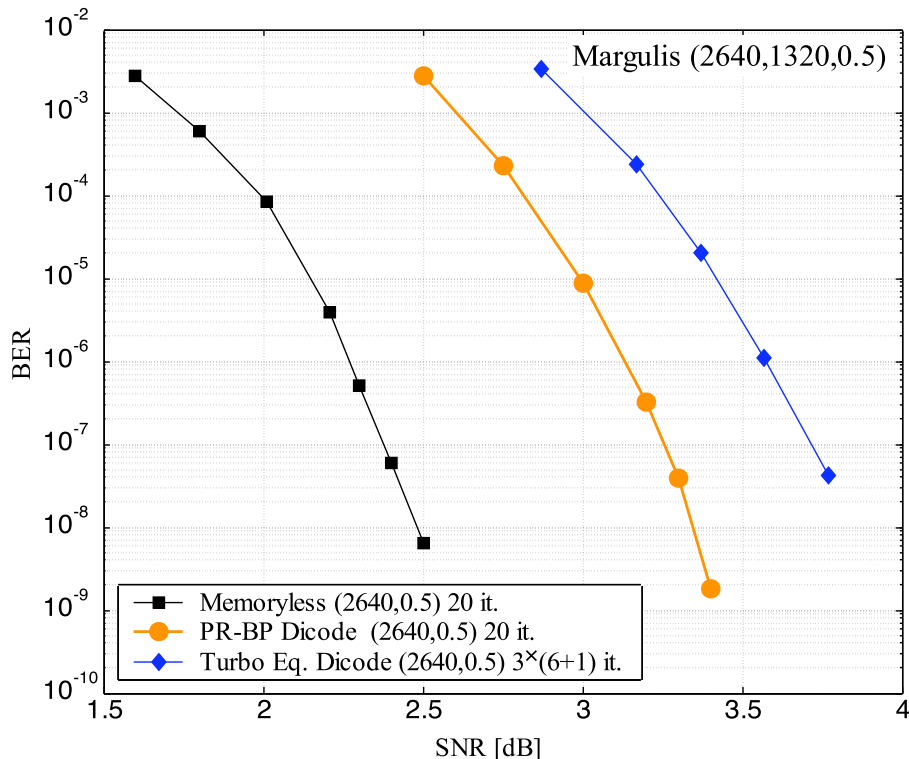


FIGURE 6.6. BER versus SNR in dB of the Margulis (2640,1320) rate 0.50 regular code over both a memoryless and a Dicode channel.

6.4.3. Length-2640, rate 0.50, regular LDPC code

The next LDPC code we evaluate is a regular Margulis (2640,1320) code with rate 0.5, column weight 3 and row weight 6 [133]. As with the previous codes we have determined the BER performance on the memoryless and Dicode channels. We use 20 iterations for PR-BP. The best decoding performance using turbo equalization is attained using $3 \times (6 + 1)$ iterations, different from the optimal combination found for the previous code. We observe that the performance of turbo equalization can be seriously degraded with a careless selection of the iteration parameters T and S , as described at the beginning of this Section, at least when the target number of iterations is small.

In the evaluation of this code there is a substantial decoding improvement with

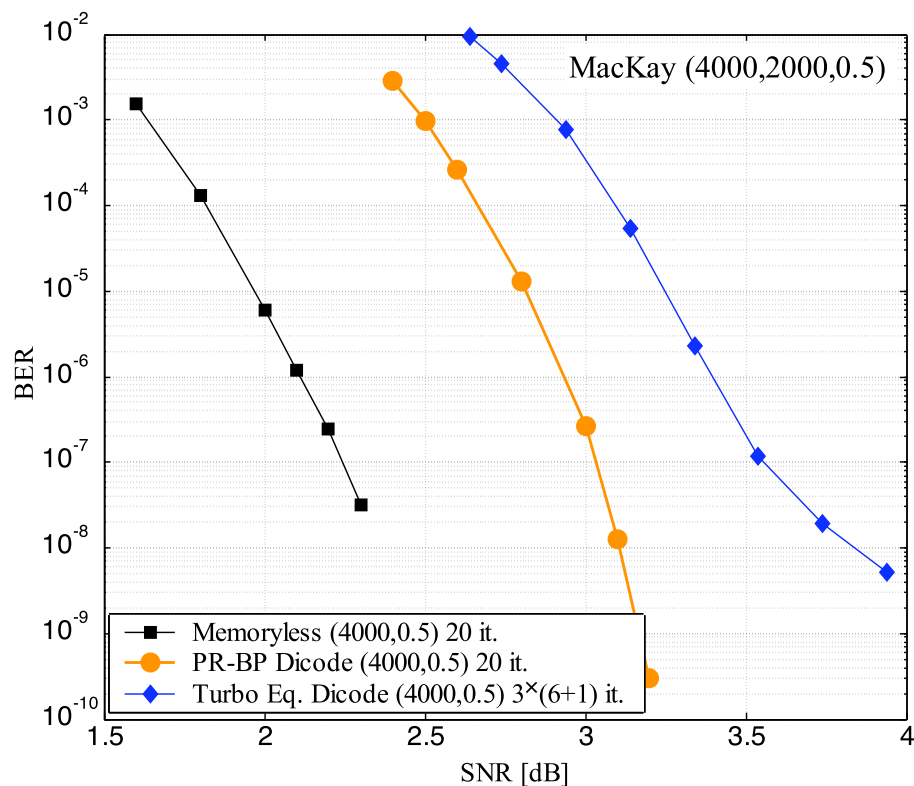


FIGURE 6.7. BER versus SNR in dB of the MacKay (4000,2000) rate 0.50 regular code over both a memoryless and a Dicode channel.

the PR-BP algorithm over turbo equalization, as observed in the BER plot of Fig. 6.6. The BER curves are marked as in the last example. The decoding gain reaches approximately 0.5 dB at $\text{BER} = 10^{-7}$ and appears to increase at higher SNR. At BER as low as 10^{-9} the PR-BP algorithm shows a steadily increasing slope, with no sign of an error floor. We observe a difference of only about 0.8 dB with the memoryless case.

6.4.4. Length-4000, rate 0.50 regular LDPC code

The last code considered is a MacKay code of block length 4000 and rate 0.5 [133]. This code is regular with column and row weights 3 and 6, respectively. Of the codes considered in this numerical BER evaluation, this is the strongest, as it can be seen in

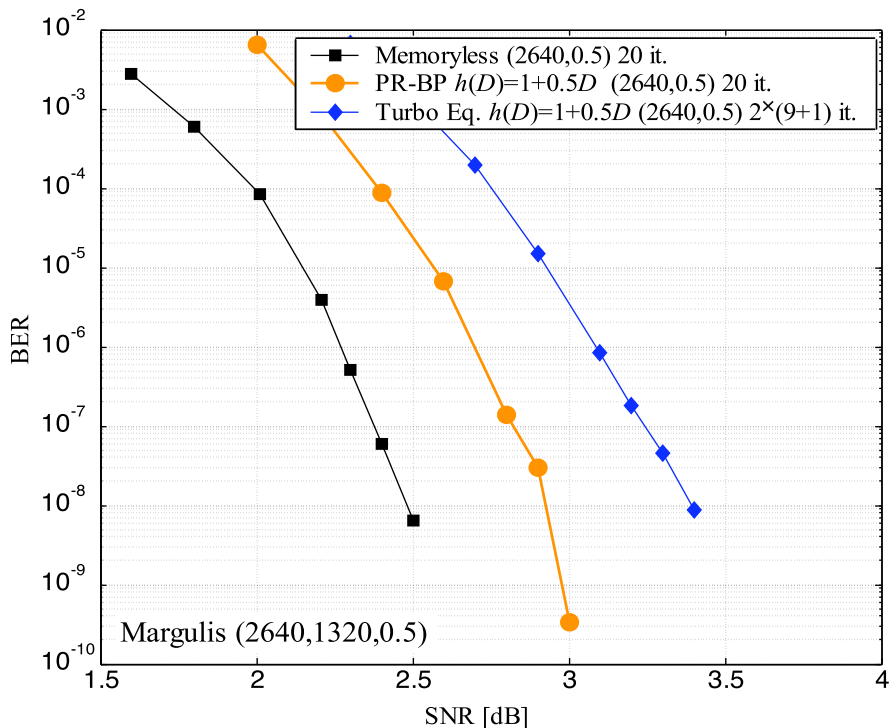


FIGURE 6.8. BER versus SNR in dB of the Margulis (2640,1320) rate 0.50 regular code over both a memoryless and a channel with $h(D) = 1 + 0.5D$.

Fig. 6.7, by the curve with square markers. We have used 20 iterations on the PR-BP algorithm and $3 \times (6+1)$ iterations on the turbo equalization algorithm. The decoding gain achieved by the PR-BP algorithm is about 0.5 dB at $\text{BER} = 10^{-7}$. It is interesting to see that the turbo equalization algorithm shows an error floor below $\text{BER} = 10^{-7}$. However, no indication of this is seen with PR-BP, even at $\text{BER} = 3 \times 10^{-10}$. Because of the error floor, the decoding gain increases to approximately 0.75 dB at $\text{BER} = 10^{-8}$.

6.4.5. Length-2640, rate 0.5 LDPC code on PR channel $h(D) = 1 + 0.5D$

As mentioned at the end of Section 6.3, the PR-BP equations are optimal on PR channels with pair-wise ISI. Although not shown here, we have evaluated the Margulis code on a PR2 channel, with $h(D) = 1 - D^2$, and as expected, the BER performance coin-

cides with that of the Dicode channel. It is worthwhile to assess the PR-BP algorithm on a channel with smaller ISI to observe how it approaches to the performance of the sum-product algorithm on a memoryless channel. We have chosen a channel with an arbitrary impulse response $h(D) = 1 + 0.5D$. Figure 6.8 shows the BER versus SNR of the Margulis code. As one would expect, the BER curve corresponding to PR-BP approaches nicely the curve of the memoryless channel, with a distance of only 0.4 dB. Again, the turbo equalization algorithm required a change of iteration parameters ($T = 2$ and $S = 9$) and its BER performance did not approach that of the memoryless case as fast as the PR-BP scheme.

6.4.6. Complexity and delay

To finish our analysis we briefly present an account of the operations required to complete one iteration of the PR-BP algorithm on a pair-wise ISI channel, of which the Dicode channel is an example. Let q and p be the (constant) outdegrees of the variable nodes and the check nodes of the LDPC code, respectively. In order to simplify the analysis, we do not consider the complexity of the \tanh and \tanh^{-1} functions (as if they were look-up-table operations) and only account for multiplications and additions. We also disregard the computation of the initial likelihoods u_i .

To compute $\mu_{i\beta}$ in (6.33), $(p-2)$ multiplications are required, and only 1 multiplication is needed for $\zeta_{i\aleph}$ in (6.34). The field $\eta_{i\alpha}$ in (6.31) requires $(q-2)$ additions of $\mu_{i\beta}$ and 1 addition of $\zeta_{i\aleph}$, besides the 2 explicit additions of the equation. Since there are $(q-1)$ different $\mu_{i\beta}$ and two different $\zeta_{i\aleph}$, the total number of multiplications for $\eta_{i\alpha}$ is $(q-1)(p-2) + 2$. For a pair-wise ISI channel there are only two edges on each ISI node. A careful look at (6.32) reveals that all the terms in $\eta_{i\aleph}$ have been computed for the field $\eta_{i\alpha}$, or for another field on an edge connected to check node

α . Only $(q - 1)$ additions have to be counted. We also count the 2 additions of the terms in (6.32). In summary, considering all edges incident on each variable node i (both from the LDPC checks and from ISI nodes), the number of multiplications N_m and additions N_a per symbol per iteration for the PR-BP algorithm on a pair-wise ISI channel are

$$N_m = q(q - 1)(p - 2) + 2, \quad N_a = q(q + 1) + 6. \quad (6.36)$$

The number of operations per symbol in the BCJR algorithm for a two-state trellis is 18 multiplications and 9 additions. We add to this the cost of the sum-product algorithm, which consists of $q(q - 1)(p - 2)$ multiplications and $q(q - 1)$ additions per symbol. Because the number of sum-product and BCJR iterations within a turbo iteration differs from case to case, the overall complexity varies. Using one of the simulations reported above we compare the complexity and the latency of PR-BP and turbo equalization.

Example: In subsection 6.4.4 we simulate the performance of a (4000,2000) LDPC code with weights $q = 3$ and $p = 6$. The total number of operations per symbol performed by the PR-BP algorithm on 20 iterations is 520 multiplications and 360 additions. In the turbo equalization algorithm we have used 3 turbo iterations, each with 7 sum-product iterations and 1 BCJR iteration. This corresponds to 486 multiplications 135 additions per symbol. With respect to delay, the PR-BP algorithm exceeds the performance of the turbo equalization algorithm. To decode a codeword it takes 20 time steps of the PR-BP algorithm, assuming that a parallel architecture is used. In contrast, the same decoding operation takes approximately $3 \times N = 12,000$ time steps of the turbo equalization algorithm. Note that the complexity within each

time step in the BCJR algorithm is smaller than (18 multiplications and 9 additions) but comparable to that of each symbol in the PR-BP algorithm (26 multiplications and 18 additions).

6.5. Conclusions

We have considered the problem of joint channel detection and error correction of LDPC codes over PR channels. We treat the joint PR-LDPC system as an inference problem defined on a graph on which we attempt to determine the marginal probabilities. Finding the marginal probabilities on the combined factor graph is equivalent to decoding a codeword on a PR channel. We have presented a derivation of the belief propagation equations for such a combined system [equations (6.28),(6.29)]. The equations originate from the minimization of the Bethe free energy –a well-known technique in statistical mechanics– and provide an optimal solution (limited by the effect of loops in the LDPC part of the graph) for PR channels with polynomial $h(D) = 1 - \alpha D^n$ (where $-1 \leq \alpha \leq 1$) and n is a non-negative integer.

The BP equations for PR channels are explicit and can be solved by any algorithm capable of solving nonlinear equations. We propose a simple iterative algorithm that permits fully parallel implementation on the symbols. Numerical simulations show that the algorithm delivers excellent BER performance on all of the LDPC codes evaluated, surpassing the performance of turbo equalization and showing no error floor above BER= 10^{-9} . The complexity of the PR-BP scheme in terms of number of operations is comparable to that of turbo equalization. Particularly good characteristics of the PR-BP scheme are its simplicity –as it requires no customization for different LDPC codes– and very low latency. In fact the algorithm exhibits a delay

that only depends on the number of iterations, and not on the codeword length. This feature makes it an excellent choice for sequence detection and decoding at high bit rates. Further work is being pursued (a) to determine the optimal BP equations for PR channels with longer memory length, and (b) to analyze, in the spirit of [132,134], the effects of LDPC-related loops on performance of the PR-BP scheme in the error-floor domain.

REFERENCES

- [1] K. Allen, E. Violette, R. Espeland, “Observed Wide-Band Digital Performance at 30.3 GHz,” *IEEE Trans. Commun.*, **34**, 733–736 (1986).
- [2] N. S. Bergano and C. R. Davidson, “Wavelength division multiplexing in long-haul transmission systems,” *J. Lightw. Technol.* **14**, 1299 (1996).
- [3] G. J. Foschini and M. J. Gans, “On limits of wireless communications in a fading environment when using multiple antennas,” *Wireless Personal Commun.* **6**, 311–335 (1998).
- [4] E. Telatar, “Capacity of multi-antenna Gaussian channels,” *European Trans. Telecomm.* **10**, 585–596 (1999).
- [5] I. Pastirk, X. Zhu, R. M. Martin, and M. Dantus, “Remote characterization and dispersion compensation of amplified shaped femtosecond pulses using MIIPS,” *Opt. Express* **14**, 8885–8889 (2006).
- [6] A. Akbulut, H. Gokhan Ilk, F. Ari, “Design, availability and reliability analysis on an experimental outdoor FSO/RF communication system,” *Transparent Optical Networks, 2005, Proc. of 7th International Conference, IEEE*, **1**, 403–406 (2005).
- [7] K. Kiasaleh, “Performance of APD-based PPM free-space optical communication system in atmospheric turbulence,” *IEEE Trans. Commun.* **53**, 1455–1461 (2005).

- [8] N. Cvijetic, S. G. Wilson and M. Brandt-Pearce, "Receiver optimization in turbulent free-space optical MIMO channels with APDs and Q-ary PPM," *IEEE Photon. Techn. Lett.* **10**, 103–105 (2007).
- [9] S. G. Wilson, M. Brandt-Pearce, Q. Cao and J. Leveque, "Free-Space optical MIMO transmission with Q-ary PPM," *IEEE Trans. Commun.* **53**, 1402–1412 (2005).
- [10] P. M. Pierce, J. Ramaprasad, and E. Eisenberg, "Optical attenuation in fog and clouds," *Proc. SPIE* **4530**, 58–71 (2001).
- [11] S. S. Muhammad, B. Flecker, E. Leitgeb, and M. Gebhart, "Characterization of fog attenuation in terrestrial free space optical links," *Optical Eng.* **46**, (2007).
- [12] M. Gebhart, E. Leitgeb, S. Sheikh Muhammad, B. Flecker, C. Chlestil, M. Al Naboulsi, F. de Fornel, and H. Sizun, "Measurement of light attenuation in dense fog conditions for FSO applications," *Proc. SPIE* **5891**, 58910K (2005).
- [13] A. L. Buck, "Effects of the atmosphere on laser beam propagation," *Appl. Opt.* **6**, 703–708 (1967).
- [14] J.-P. Laussade, A. Yariv, and J. Comly, "Optical communication through random atmospheric turbulence," *Appl. Opt.* **8**, 1607-1611 (1969).
- [15] J. H. Churnside and S. F. Clifford, "Log-normal Rician probability-density function of optical scintillations in the turbulent atmosphere," *J. Opt. Soc. Am. A* **4**, 1923–1930 (1987).
- [16] X. Zhu and J. M. Kahn, "Free-space optical communication through atmospheric turbulence channels," *IEEE Trans. Commun.*, **50**, 1293–1300 (2002).

- [17] J. C. Ricklin and F. M. Davidson, "Atmospheric turbulence effects on a partially coherent Gaussian beam: implications for free-space laser communication," *J. Opt. Soc. Am. A* **19**, 1794–1802 (2002).
- [18] A. C. Boucouvalas, "Guest editorial -Optical wireless communications," *IEEE Wireless Commun.*, **10**, 6–7 (2003).
- [19] S. M. Flatté, C. Bracher, and G.-Y. Wang, "Probability-density functions of irradiance for waves in atmospheric turbulence calculated by numerical simulation," *J. Opt. Soc. Am. A* **11**, 2080–2092 (1994).
- [20] L. C. Andrews and R. L. Phillips, "I-K distribution as a universal propagation model of laser beams in atmospheric turbulence," *J. Opt. Soc. Am. A* **2**, 160–163 (1985).
- [21] R. J. Hill and R. G. Frehlich, "Probability distribution of irradiance for the onset of strong scintillation," *J. Opt. Soc. Am. A* **14**, 1530–1540 (1997).
- [22] L. C. Andrews, R. L. Phillips, C. Y. Hopen, M. A. Al-Habash, "Theory of optical scintillation," *J. Opt. Soc. Am. A*, **16**, 1417–1429 (1999).
- [23] A. Belmonte, A. Comerón, J. A. Rubio, J. Bará, and E. Fernández, "Atmospheric-turbulence-induced power-fade statistics for a multiaperture optical receiver," *Appl. Opt.* **36**, 8632–8638 (1997).
- [24] J. C. Ricklin and F. M. Davidson, "Atmospheric optical communication with a Gaussian Schell beam," *J. Opt. Soc. Am. A* **20**, 856–866 (2003).

- [25] O. Korotkova, L. C. Andrews, R. L. Phillips, “Model for a partially coherent Gaussian beam in atmospheric turbulence with application in Lasercom,” *SPIE Opt. Eng.* **43**, 330–341 (2004).
- [26] H. Yuksel, S. Milner, C. Davis, “Aperture averaging for optimizing receiver design and system performance on free-space optical communication links,” *J. Opt. Netw.*, **4**, 462–475 (2005).
- [27] J. A. Anguita, M. A. Neifeld, and B. V. Vasic, “Spatial correlation and irradiance statistics in a multiple-beam terrestrial free-space optical communication link,” *Appl. Opt.* **46**, (2007).
- [28] Jing Li, M. Uysal, “Achievable information rate for outdoor free space optical communication with intensity modulation and direct detection,” in *Global Telecommunications Conference 2003. GLOBECOM 03 (IEEE, 2003)*, **5**, 2654–2658.
- [29] M. Uysal and J. Li, “Error rate performance of coded free-space optical links over gamma-gamma turbulence channels,” in *Proceedings of IEEE International Conference on Communication ICC’04 (IEEE, 2004)*, **6**, 3331–3335.
- [30] J. A. Anguita, I. B. Djordjevic, M. A. Neifeld, and B.V. Vasic, “Shannon capacities and error-correction codes for the optical atmospheric turbulent channels”, *J. Opt. Netw.*, **4**, 586–601 (2005).
- [31] C. Higgs, H. Barclay, S. Cusumano, K. Biliman, “Active tracking using multi-beam illumination,” *Proc. SPIE*, **3381**, 160 (1998).

- [32] V. Vilnrotter, C.-W. Lau, M. Srinivasan, K. Andrews, R. Mukai, "Optical array receiver for communication through atmospheric turbulence," *J. Light. Tech.* **23**, 1664–1675 (2005).
- [33] M. Razavi, J. H. Shapiro, "Wireless optical communications via diversity reception and optical amplification," *IEEE Trans. Wireless Commun.*, **4**, 975–983 (2005).
- [34] J. A. Anguita, M. A. Neifeld, and B. Vasic, "Multi-beam space-time coded systems for optical atmospheric channels," *Proc. SPIE* **6304**, 63041B (2006).
- [35] A. Harris, J. J. Sluss, H. H. Refai, P. G. LoPresti, "Comparison of active beam steering elements and analysis of platform vibrations for various long-range FSO links," *Proc. SPIE*, **5819**, 474–484 (2005).
- [36] K. Kiasaleh "Beam-tracking in FSO links impaired by correlated fading," *Proc. SPIE*, **6304**, 63041I (2006).
- [37] K. Kazaura, K. Omae, T. Suzuki, M. Matsumoto, E. Mutafungwa, T. O. Korhonen, T. Murakami, K. Takahashi, H. Matsumoto, K. Wakamori, and Y. Arimoto, "Enhancing performance of next generation FSO communication systems using soft computing-based predictions," *Opt. Express* **14**, 4958-4968 (2006).
- [38] P. G. Goetz *et al.*, "Modulating retroreflector implementation of mil-std 1553 protocol with free-space optics," *Aerospace Conference, 2003. Proc. of the IEEE* **4**, 1799–1808 (2003).
- [39] K. Sayyah, A. Narayanan, D. Persechini, P. Brewer, "Conformal pixellated MQW modulator structure for modulating retroreflector applications," *IEEE Photon. Techn. Lett.* **17**, 1854–1856 (2005).

- [40] S. Karp, R. Gagliardi, S. E. Moran, and L. B. Stotts, *Optical channels* (Plenum, NY, 1988).
- [41] V. I. Tatarskii, *Wave propagation in a turbulent medium* (McGraw-Hill, 1961), trans. by R. A. Silverman.
- [42] A. Ishimaru, *Wave propagation and scattering in random media*, Academic, NY, 1978.
- [43] L.C. Andrews, R.L. Phillips, C.Y. Hopen, *Laser beam scintillation with applications* (SPIE Press, 2001).
- [44] L.C. Andrews and R.L. Phillips, *Laser beam propagation through random media*, 2nd ed. (SPIE Press, 2005).
- [45] R. J. Hill and G. R. Ochs, “Inner-scale dependence of scintillation variances measured in weak scintillation,” *J. Opt. Soc. Am. A* **9**, 1406–1411 (1992).
- [46] R. J. Hill and S. F. Clifford, “Modified spectrum of atmospheric temperature fluctuations and its application to optical propagation,” *J. Opt. Soc. Am.* **68**, 892–899 (1978).
- [47] L. C. Andrews, “An analytical model for the refractive index power spectrum and its application to optical scintillations in the atmosphere,” *J. Mod. Opt.*, **39**, 1849–1853 (1992).
- [48] J. W. Goodman, *Introduction to Fourier optics*, 2nd ed. (McGraw-Hill, 1996).
- [49] J. A. Anguita, “A Study of codes and capacities for nonlinear dispersive fibers,” MS Thesis, University of Arizona (2004).

- [50] A. Belmonte, “Feasibility study for the simulation of beam propagation: consideration of coherent lidar performance,” *Appl. Opt.*, **39**, 5426–5445, (2000).
- [51] M.A. Al-Habash, L.C. Andrews, and R. L. Phillips, “Mathematical model for the irradiance probability density function of a laser beam propagating through turbulent media,” *Opt. Eng.*, **40**, 1554–1562 (2001).
- [52] I. B. Djordjevic and B. Vasic, “MacNeish-Mann theorem based iteratively decodable codes for optical communication systems,” *IEEE Commun. Lett.* **8**, 538–540 (2004).
- [53] O. Milenkovic, I. B. Djordjevic, and B. Vasic, “Block-circulant low-density parity-check codes for optical communication systems,” *J. Sel. Top. Quant. Electron.* **10**, 294–299 (2004).
- [54] B. Vasic, O. Milenkovic “Combinatorial construction of low-density parity check codes,” *IEEE Trans. Inf. Theory* **50**, 1156–1176 (2004).
- [55] Y. Kou, S. Lin, M. P. C. Fossorier, “Low-density parity-check codes based on finite geometries: a rediscovery and new results,” *IEEE Trans. Inf. Theory* **47**, 2711–2736 (2001).
- [56] L. C. Andrews and R. L. Phillips, “Mathematical genesis of the I-K distribution for random optical fields,” *J. Opt. Soc. Am. A* **3**, 1912–1919 (1986).
- [57] J. H. Churnside and R. J. Hill, “Probability density of irradiance scintillations for strong path integrated refractive turbulence,” *J. Opt. Soc. Am. A* **4**, 727–733 (1987).

- [58] J. H. Churnside and R. G. Frehlich, “Experimental evaluation of log-normally modulated Rician and IK models of optical scintillation in the atmosphere,” *J. Opt. Soc. Am. A* **6**, 1760–1766 (1989).
- [59] T. M. Cover and J. A. Thomas, *Elements of Information Theory* (Wiley-Interscience, 1991).
- [60] D. P. Palomar, J. R. Fonollosa, and M. A. Lagunas, “Capacity results of spatially correlated frequency-selective MIMO channels in UMTS,” in 54th IEEE Vehicular Technology Conference, 2001. VTC 2001 (IEEE, 2001), **2**, 553–557.
- [61] M. Fozunbal, S. W. McLauhlin, R. W. Schafer, “On performance limits of MIMO-OFDM systems over block-fading channels,” in Wireless Communications and Networking Conference, 2004. WCNC (IEEE, 2004), **2**, 976–980.
- [62] A. Papoulis, *Probability, Random Variables, and Stochastic Processes* (WCB/McGraw Hill, 1991).
- [63] C. P. Robert, G. Casella, *Monte Carlo Statistical Methods* (Springer-Verlag, 2004).
- [64] M. Uysal, S. Mohammad Navidpour, and J. Li, “Error rate performance of coded free-space optical links over strong turbulence channels,” *IEEE Commun. Lett.*, **8**, 635–637 (2004).
- [65] S. Lin, D. J. Costello, *Error Control Coding* (Prentice Hall, 2004).
- [66] W. E. Ryan, “Concatenated convolutional codes and iterative decoding,” in *Wiley Encyclopedia in Telecommunications*, J. G. Proakis, ed. (Wiley, 2003).

- [67] M. Mansour, "Implementation of LDPC Decoders," presented at the IEEE Comm. Theory Workshop, Park City, Utah, 13–15 June 2005.
- [68] J. H. Churnside, "Aperture averaging of optical scintillations in the turbulent atmosphere," *Appl. Opt.*, **30**, 1982–1994 (1991).
- [69] L. C. Andrews, R. L. Phillips, C. Y. Hopen, "Aperture averaging of optical scintillations: power fluctuations and the temporal spectrum," *Waves in Random Media*, **10**, 53–70 (2000).
- [70] S. G. Wilson, M. Brandt-Pearce, Q. Cao, M. Baedke, "Optical repetition MIMO transmission with multipulse PPM," *IEEE J. Sel. A. Commun.*, **23**, 1901–1910 (2005).
- [71] S. M. Navidpour, M. Uysal, and J. Li, "BER performance of MIMO free-space optical links," in *Proceedings of IEEE Conference on Vehicular Technology (IEEE 2004)*, p. 3378.
- [72] M. K. Simon, V. A. Vilnrotter, "Alamouti-type space-time coding for free-space optical communication with direct detection," *IEEE Trans. Wireless Comm.*, **4**, 35–39, (2005).
- [73] A. Biswas and M. W. Wright, "Mountain-top-to-mountain-top optical link demonstration: part I," *IPN Progress Report 42–149*, JPL (2002).
- [74] P. T. Ryan, W. H. Lowrey, I.A. De La Rue, R.Q. Fugatea, "Scintillation characterization for multiple beams," *Proc. SPIE*, **3763**, 210 (1999).
- [75] I. Kim, P. Adhikari, E. Korevaar, A. Majumdar, "Scintillation reduction using multiple transmitters," *Proc. SPIE*, **2990**, 102 (1997).

- [76] H. Willebrand, “Multibeam-multipath terrestrial lasercom terminal,” Proc. SPIE, **3532**, 16 (1999).
- [77] A. Tiker, N. Yarkoni, N. Blaunstein, A. Zilberman, and N. Kopeika, “Prediction of data stream parameters in atmospheric turbulent wireless communication links” Appl. Opt. **46**, 190–199 (2007).
- [78] N. Perlot, “Evaluation of the scintillation loss for optical communications systems with direct detection,” SPIE Opt. Eng. **46(2)**, 025003 (2007).
- [79] J.C . Dainty, M.J. Northcott, D.-N. Qu, “Measurements of the temporal correlation of images at La Palma,” J. of Modern Optics, **37**, 1247–1254 (1990).
- [80] R. J. McEliece and W. E. Stark, “Channels with Block Interference,” IEEE Trans. Inf. Theory, **30**, 44–53 (1984).
- [81] J. W. Goodman, *Statistical optics* (Wiley, 1985), Chapter 5.
- [82] V. Tarokh, H. Jafarkhani, A.R. Calderbank, “Space-time block codes from orthogonal designs,” IEEE Trans. Inf. Theory **45**, 1456–1467 (1999).
- [83] L. Allen, M. W. Beijersbergen, R. J. C. Spreeuw, and J. P. Woerdman, “Orbital angular momentum of light and the transformation of Laguerre Gaussian laser modes,” Physical Review A, **45**, 8185–8189 (1992).
- [84] A. Vaziri, G. Weihs and A. Zeilinger “Superpositions of the orbital angular momentum for applications in quantum experiments,” J. Opt. B Quantum Semi-class. Opt. **4**, S47–S51 (2002).

- [85] G. Gibson, J. Courtial, M. J. Padgett, “Free-space information transfer using light beams carrying orbital angular momentum,” *Opt. Express*, **12**, 5448–5456 (2004).
- [86] Z. Bouchal and R. Celechovsky, “Mixed vortex states of light as information carriers,” *New J. of Physics* **6**, 131 (2004).
- [87] Jingzhi Wu, Hui Li, Yangjun Li, “Encoding information as orbital angular momentum states of light for wireless optical communications,” *Opt. Eng.*, **46**, (2007).
- [88] Z. Bouchal, J. Wagner, M. Chlup, “Self-reconstruction of a distorted nondiffracting beam,” *Optics Commun.*, **151**, 207–211 (1998).
- [89] W. C. Soares, D. P. Caetano, and J. M. Hickmann, “Hermite-Bessel beams and the geometrical representation of nondiffracting beams with orbital angular momentum,” *Opt. Express*, **14**, (2006).
- [90] Carlos López-Mariscal, Julio C. Gutiérrez-Vega, “Orbital angular momentum transfer in helical Mathieu beams,” *Opt. Express*, **14** (2006).
- [91] D. Rozas, C. T. Law, G. A. Swartzlander, Jr., “Propagation dynamics of optical vortices,” *J. Opt. Soc. Am. B*, **14**, 3054–3065 (1997).
- [92] V. Aksenov, “Fluctuations of orbital angular momentum of vortex laser-beam in turbulent atmosphere,” *Proc. SPIE*, **5892**, 58921Y-1 (2005).
- [93] J. Lin, X.-C. Yuan, S. H. Tao, R. E. Burge, “Synthesis of multiple collinear helical modes generated by a phase-only element,” *J. Opt. Soc. Am. A*, **23**, 1214–1218 (2006).

- [94] D. V. Petrov, F. Canal, and L. Torner, “A simple method to generate optical beams with a screw phase dislocation,” *Opt. Commun.*, **143**, 265–267 (1997).
- [95] M. J. Padgett and L. Allen, “Orbital angular momentum exchange in cylindrical-lens mode converters,” *J. Opt. B Quantum Semiclass. Opt.*, **4**, S17–S19 (2002).
- [96] M. W. Beijersbergen, R. P. C. Coerwinkel, M. Kristensen, and J. P. Woerdman, “Helical-wavefront laser beams produced with a spiral phaseplate,” *Opt. Commun.*, **112**, 321–327 (1994).
- [97] K. Sueda, G. Miyaji, N. Miyanaga and M. Nakatsuka, “Laguerre-Gaussian beam generated with a multilevel spiral phase plate for high intensity laser pulses,” *Opt. Express*, **12**, 3548–3553 (2004).
- [98] S. S. R. Oemrawsingh, J. A. W. van Houwelingen, E. R. Eliel, J. P. Woerdman, E. J. K. Verstegen, J. G. Kloosterboer, and G. W. t Hooft “Production and Characterization of Spiral Phase Plates for Optical Wavelengths,” *Appl. Opt.*, **43**, 688–694 (2004).
- [99] V. V. Kotlyar, S. N. Khonina, A. A. Kovalev, and V. A. Soifer, “Diffraction of a plane, finite-radius wave by a spiral phase plate,” *Opt. Lett.*, **31**, 1597–1599 (2006).
- [100] C.-S. Guo, D.-M. Xuea, Y.-J. Hana, and J. Ding, “Optimal phase steps of multi-level spiral phase plates,” *Opt. Commun.*, **268**, 235–239 (2006).
- [101] C. Rotschild, S. Zommer, S. Moed, O. Hershcovitz, and S. G. Lipson, “Adjustable spiral phase plate,” *Appl. Opt.* **43**, 2397–2399 (2004).

- [102] V. Y. Bazhenov, M. S. Soskin, and M. V. Vasnetsov, "Screw dislocations in light wavefronts," *J. of Mod. Opt.*, **39**, 985–990 (1992).
- [103] N. R. Heckenberg, R. McDuff, C. P. Smith, and A. G. White, "Generation of optical phase singularities by computer-generated holograms," *Opt. Lett.*, **17**, 221–223 (1992).
- [104] D. J. Brady, "Multiplex sensors and the constant radiance theorem," *Opt. Lett.* **27**, 16–18 (2002).
- [105] S. S. Muhammad, E. Leitgeb, O. Koudelkat, "Multilevel Modulation and Channel Codes for Terrestrial FSO links," 2nd International Symposium on Wireless Commun. Systems, 2005, pp. 795-799, 5-7 Sept. 2005.
- [106] S. M. Flatté and J. S. Gerber, "Irradiance-variance behavior by numerical simulation for plane-wave and spherical-wave optical propagation through strong turbulence," *J. Opt. Soc. Am. A*, **17**, 1092–1097 (2000).
- [107] S. Jafar and A. Goldsmith, "Multiple-antenna capacity in correlated Rayleigh fading with channel covariance information," *IEEE Trans. Wireless Commun.*, **4**, 990–998 (2005).
- [108] O. E. Agazzi, M. R. Hueda, H. S. Carrer, and D. E. Crivelli, "Maximum-likelihood sequence estimation in dispersive optical channels," *J. Lightw. Technol.* **23**, 749–763 (2005).
- [109] B. Kurkoski, P. Siegel, J. Wolf, "Joint message-passing decoding of LDPC codes and partial-response channels," *IEEE Trans. Inf. Theory* **48**, 1410–1422 (2002).

- [110] S. L. Ariyavisitakul and Ye Li, "Joint coding and decision feedback equalization for broadband wireless channels," *IEEE J. Sel. Areas Commun.* **16**, 1670–1678 (1998).
- [111] H. Kobayashi, "Correlative level coding and maximum-likelihood decoding," *IEEE Trans. Inf. Theory* **IT-17**, 586–594 (1971).
- [112] P. Kabal and S. Pasupathy, "Partial-response signaling," *IEEE Trans. Commun.* **COM-23**, 921–934 (1975).
- [113] H. Thapar and A. Patel, "A class of partial-response systems for increasing storage density in magnetic recording," *IEEE Trans. Magn.* **MAG-23**, 3666–3668 (1987).
- [114] A. Acampora, "Maximum-likelihood decoding of binary convolutional codes on band-limited satellite channels," *IEEE Trans. Commun.* **26**, 766–776 (1978).
- [115] L. R. Bahl, J. Cocke, F. Jelinek, and J. Raviv, "Optimal decoding of linear codes for minimizing symbol error rate," *IEEE Trans. Inf. Theory* **20**, 284–287 (1974).
- [116] R. G. Gallager, *Low-Density Parity-Check Codes*. (Cambridge, MA, MIT Press, 1963).
- [117] R. M. Tanner, "A recursive approach to low complexity codes," *IEEE Trans. Inf. Theory* **IT-27**, 533–547 (1981).
- [118] D. J. C. MacKay and R. M. Neal, "Near Shannon limit performance of low density parity check codes," *IEEE Electron. Lett.* **32**, 1645–1646 (1996).

- [119] D. J. C. MacKay, “Good error-correcting codes based on very sparse matrices,” *IEEE Trans. Inf. Theory* **45**, 399–431 (1999).
- [120] T. Mittelholzer, A. Dholakia, and E. Eleftheriou, “Reduced-complexity decoding of low density parity check codes for generalized partial response channels,” *IEEE Trans. Magn.* **37**, 721–728 (2001).
- [121] F. R. Kschischang, B. J. Frey, and H.-A. Loeliger, “Factor graphs and the sum-product algorithm,” *IEEE Trans. Inf. Theory* **47**, 498–519 (2001).
- [122] M. Tuchler, R. Koetter, A. C. Singer, “Turbo equalization: principles and new results,” *IEEE Trans. Commun.* **50**, 754–767 (2002).
- [123] T. Souvignier, M. Oberg, P. H. Siegel, R. E. Swanson, and J. Wolf, “Turbo decoding for partial response channels,” *IEEE Trans. Commun.* **48**, 1297–1308 (2000).
- [124] W. Ryan, “Concatenated codes for class IV partial response channels,” *IEEE Trans. Commun.* **49**, 445–454 (2001).
- [125] C. Douillard, M. Jezequel, C. Berrou, A. Picart, P. Didier, and A. Glavieux, “Iterative correction of intersymbol interference: Turbo equalization,” *Eur. Trans. Telecomm.* **6**, 507–511 (1995).
- [126] P. Pakzad and V. Anantharam, “Kikuchi approximation method for joint decoding of LDPC codes and partial response channels,” *IEEE Trans. Commun.*, **54**, 1149–1153 (2006).

- [127] O. Shental, A. J. Weiss, N. Shental, Y. Weiss, “Generalized belief propagation receiver for near- optimal detection of two-dimensional channels with memory,” Inform. Theory Workshop, 2004. IEEE, **50**, 225–229, Oct. 2004.
- [128] J. S. Yedidia, W. T. Freeman, and Y. Weiss, “Constructing free-energy approximations and generalized belief propagation algorithms,” IEEE T. Inf. Theory **51**, 2282–2312 (2005).
- [129] H.-A. Loeliger, “An Introduction to Factor Graphs,” IEEE Signal Process. Mag., Jan 2001, 28–41.
- [130] G. D. Forney, Codes on graphs: normal realizations, IEEE Trans. Inf. Theory **47**, 520–548 (2001).
- [131] A. Kavcic, X. Ma, and N. Varnica, “Matched information rate codes for partial response channels,” IEEE Trans. Inf. Theory **51**, 973–989 (2005).
- [132] M. Chertkov and V. Chernyak, “Loop series for discrete statistical models on graphs,” J. Stat. Mech. (2006) P06009, cond-mat/0603189.
- [133] D. J.C. MacKay, *Encyclopedia of sparse graph codes*. [Online]. Available: <http://www.inference.phy.cam.ac.uk/mackay/codes/data.html>
- [134] M. Chertkov and V. Chernyak, “Loop calculus helps to improve belief propagation and linear programming decodings of low-density-parity-check codes,” presented at 44th Allerton Conference (Sept. 2006, Allerton, IL), arXiv:cs.IT/0609154.